Graphene-SiC Particle Reinforced Aluminum Alloy Composite Foam: Response to High Strain Rate Deformation

---

A Thesis presented to

The Faculty of the Graduate School

At the University of Missouri-Columbia

In Partial Fulfillment

Of the Requirements for the Degree of

Master of Science

By

SOURAV DAS

Prof. (Dr.) Sanjeev Khanna, Thesis Supervisor

JULY 2016

The undersigned, appointed by the dean of the Graduate School, have examined the

Thesis entitled:

Graphene-SiC Particle Reinforced Aluminum Alloy Composite Foam: Response to High Strain Rate Deformation

Presented by

Sourav Das

A candidate for the degree of Master of Science and hereby certify that, in their opinion, it is worthy of acceptance.

(Prof.) Dr. Sanjeev Khanna, PhD

(Prof.) Dr. Jinn-Kuen Chen, PhD

(Prof.) Dr. Sarah Orton, PhD

Dedication

I would like to dedicate this research to my father Dr. S. Das and my mother Mrs. Keka Das. My dad has been such an amazing role model and has always supported me in every decision I take. He is extremely selfless and has taught me how to be a great yet kind leader. My mom has gone out her way to include me in all of her business ventures so that I can learn how to be successful early in life and every action she makes is always in the best interest to me. I am blessed to have parents like them and always want to make them proud. Thank you for being such a big part of my achievement.

SOURAV DAS

Acknowledgement

First, I take this opportunity to express my sincere gratitude to my advisor Prof. (Dr.) Sanjeev Khanna for the continuous support of my Master study and research, and for his patience, motivation, enthusiasm, and immense knowledge. His guidance helped me in all the time of research and writing of this thesis. Besides my advisor, my sincere thanks go to the rest of my thesis committee: Dr. J.K Chen and Dr. Sarah Orton for their encouragement and insightful comments. I would also like to thank, Ghazan, Rex, who have helped me.

I am grateful to my fellow worker Mr. Abdelhakim Aldoshan who helped me on this thesis from the early stages of experiments.

Finally yet importantly, I owe my deepest gratitude to my beloved parents Dr. S. Das and Mrs. Keka Das, for their unceasing encouragements and supporting me spiritually throughout my life.

Thank you all, I really appreciate everything you have done for me.

SOURAV DAS

Table of Contents

LIST OF FIGURES

List of Tables

Abstract

Aluminum foams are becoming potential material for multifunctional applications because it is lightweight and has excellent combination of physical and mechanical properties and noise and vibration mitigation characteristic. Because of its cellular structure, it exhibits excellent damping capacity, sound and noise absorption, shock and impact energy absorption. Applications of metal foam for energy absorption and crashworthiness require knowledge on their compressive deformation response at various strain rates. The properties of metal foam are dependent on cell wall mechanical properties and their microstructure. Cell wall properties have been improve by adding Graphene Nano platelets as reinforcement to the Al-foam. This investigation is related to the study of quasi-static compressive behavior and the high strain rate response under dynamic compressive loading in Graphene Al foam. The experimental results show that the peak, plateau stress and energy absorption of reinforced foam is much higher than unreinforced foam. The high strain rate compressive behavior of Graphene Al foam been studied using the split Hopkinson pressure bar apparatus. It is found that peak stress, plateau stress and energy absorption of Graphene Al foam increases as the strain rate increases over a range of strain rate from 500 s^{-1} to 2760 s^{-1}. Thus, the Graphene Al foam is strain rate sensitive the plateau stress and energy absorption in the Graphene -Al foam increased by about two times and three times, respectively, compared to unreinforced foam.

CHAPTER: 1

INTRODUCTION

Metal foams are becoming potential material for multifunctional applications because of its lightweight and excellent combination of physical and mechanical properties (1). Because of its cellular structure, it exhibits excellent damping capacity, sound and noise absorption, shock and impact energy absorption (2-6). Attempts have been made to use these foams as the core in sandwich panels, foam filled tubes for structural applications, besides others. The open cell foams are excellent materials for heat exchangers, catalytic converter, filters etc. The Closed-cell aluminum foams retain the fire resistant and recycling capability of other metallic foams but add the ability to float in water. Attentions is being paid to use these materials for flooring of ships, automobiles, trains and defense vehicles. Depending on the applications, the character of foams is important. For shock absorption and impact energy absorption applications, high strain rate deformation behavior of these foams is an important characteristic to examine. Since the last decade, considerable attention has been paid to the development of porous and/or cellular metallic materials for a wide range of applications with special reference to crash energy absorption and thermal management. These metal foams have been found to contain porosity ranging from 50% to 95%. Out of different metallic systems, majority of the work has been carried out on aluminum and its alloys. Worldwide, considerable effort has been made towards the development of processes for making metal foams based on aluminum, Ti, Ni, Steel, copper with an objective to have uniform distribution of pores with controlled size range and porosity level. Metal foam can sustain sudden impact and able to convert much of the impact energy into the plastic energy and absorbs more energy than the bulk material per unit weight. Because of these properties, it is used as a high-energy absorbing material in crash protectors packaging, door panel, front hood, bumpers, roof panels, bonnets and body frame element etc. The range of applications of metallic foam is increasing steadily day by day. While defining, more distinctly the meaning of metal foam, one must distinguish the literal meaning of cellular metal. Cellular material is defined as a metallic body, which has any kind of gaseous voids. The gaseous voids are separated by the metallic body. Cellular material can be divided into three groups namely porous metal, metal foam and metal sponge. Figure 1 shows the schematic diagram of different groups of cellular material. Porous metal is a special kind of cellular material in which pores are round in nature and isolated from each other. Metal foam is a special kind of cellular material that originates from the liquid metal and can have any shape right from spherical to polyhedral and separated from each other by thin metallic film. Metal sponge or open cell foam is also a special kind of cellular material in which the pores are interconnected.

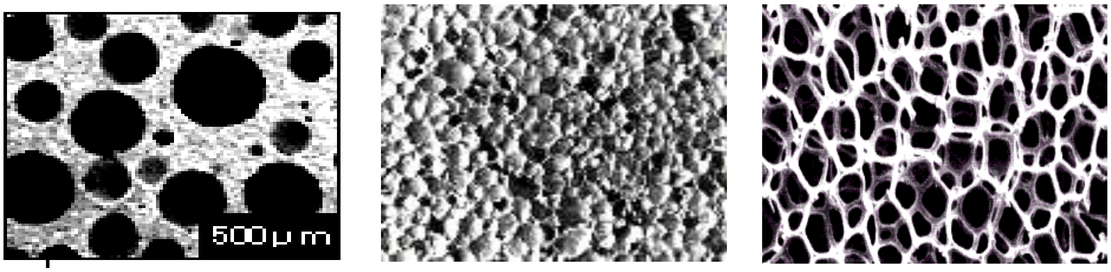

Porous metal Foam Metal Sponge

Fig. 1.1 Classification of cellular material (Reference: http://www.metalfoam.net/)

Applications of metal foam for energy absorption and crashworthiness require knowledge of their compressive response at various strain rates (7-10). Many researchers in this area have carried out several studies in the past but there exist contradictory opinions. This arises mainly because of their different foam structure, density of foam and defects in the cell walls. Among various properties, impact energy absorption appears to be important property imparted by the aluminum foam. The energy absorption capacity of Al foam depends upon the area under the stress-strain curve. One of the major applications of closed pore Al foam is the crash box. Al foam is inserted into a hollow portion of the crash box in order to enhance the energy absorption capability. Presently crash box is a hollow section and it is proposed that by inserting closed pore Al foam in the hollow portion the energy absorption capacity of the crash box could be enhanced considerably (11-15). Crash box which is located at the front side frame of the car, it is one of the most important automotive parts for crash energy absorption. In case of frontal crash accident, for example, crash box is expected to collapse by absorbing crash energy prior to the other body parts so that the damage of the main cabin frame is minimized and passengers are saved. The energy absorption capacity of Al foam is dependent upon the area under the true stress–strain graph; hence to achieve higher energy absorption capacity from Al foam it must have a wide plateau stress region. Applications of metal foam for energy absorption and crashworthiness require knowledge on their compressive deformation response at various strain rates (16-17).

Realizing the above fact, recently preliminary are being made to enhance the strength of cell walls by dispersing carbon Nano tubes (18-19). It has been reported that Graphene foam is used for water oxidation (20) and for sensor application (21). To the best of our knowledge this study is the first attempt to develop and study the mechanical response of Graphene reinforced Al foam under both static and dynamic loading. However, recent literature reported that reinforcement of wt.0.3%Graphene in solid Al alloy enhances the strength of the matrix alloy by 62% (22).

Graphene is pure carbon in the form of sheets one atom thick. Graphene is estimated to be 200 times stronger than steel, is as flexible as rubber, and conducts heat and electricity extremely efficiently. Further, because it is only an atom thick, it is nearly two-dimensional, imbuing it with many interesting light-related and water-related properties. Graphene is not a naturally occurring substance. Even though it had been theorized by physicists since 1960s, it was only produced for the first time in 2004. Back then, production methods made Graphene usage prohibitively expensive; however, over the past decade, academics and corporate researchers have made great strides in reducing production costs. And as those costs drop further with each passing year, Graphene is poised to revolutionize the fields of medicine, electronics, computing, and more. Graphene is a hexagonal lattice of carbon atoms bonded tightly together. Its sp2 hybridization – a double bond between the carbon atoms, coupled with its especially thin atomic thickness, fuel its special properties. Graphene is a monolayer of carbon atoms arranged in honeycomb lattice has a higher electrical and thermal conductivity than copper. Its room temperature electron mobility is up to 200,000 cm^2/(V-s). Its ability to conduct electricity and heat so effectively is believed to be a function of the carbon bonds being very small and strong. Being composed of singular carbon atoms, Graphene is also so thin as to be effectively two-dimensional, in addition to being extremely light weight. Additionally, the material also weighs less than 1 milligram per square meter. Graphene 's benefits are closely tied to its properties, which make it tremendously attractive as a raw material for the production of a wide variety of commercial goods. In short, Graphene 's major benefits are that it is highly conductive – 200 times more conductive than silicon, and conducts heat very efficiently as well; thin – enough to be considered a 2D material; transparent; strong

– approximately 200 times stronger than steel; light-weight; and flexible, while maintaining its strength and conductivity. The Graphene used in this experiment is H - Grade Graphene supplied by World-Leading Graphene Company - XG Sciences World-Leading (www.xgsciences.com). Grade H particles have an average thickness of approximately 15 Nanometers and a typical surface area of 50 to 80 m^2/g, with average particle diameters of 5 microns.

It is expected that incorporating Graphene Nano platelets into metal matrices could lead to ultrahigh performance metal matrix Nanocomposites (MMNCs). However, it is very difficult, to effectively incorporate and disperse Graphene Nano platelets into metals to obtain bulk Graphene Nano platelets reinforced MMNCs this problem is due to Nano platelets large surface areas and high surface energy that easily leads to agglomerations. So far, little work on high performance Graphene Nano platelets reinforced MMNCs have been reported (23-25).

In the present investigation Al alloy–SiC composite and Al Alloy-SiC-Graphene composite foams were studied under compression load. Initially, both the Al-SiC composite foam and Al composite foam with Graphene were studied under quasi-static load using a servo hydraulic machine at strain rates of $0.001s^{-1}$ to $1s^{-1}$. The effect of Graphene in enhancing the compressive strength has been observed and then a detailed study was carried out only on Al alloy composite with Graphene under dynamic loading condition using Split Hopkinson Pressure Bar (SHPB) unit over a strain rates of 500s‑1 to $2760s^{-1}$.

Chapter 2: Literature Review

SPLIT HOPKINSON PRESSURE BAR

2.1 Split Hopkinson Pressure bar (SHPB) theory

2.1.1 Classical SHPB

In 1941, Bancroft [26] reported on the distortion of longitudinal pulses in elastic cylinders resulting from the effect of lateral inertia. They concluded that only the fundamental modes of longitudinal pulse should be considered. In 1982, Gorham [27] investigated a numerical method for correction of dispersion in pressure bar signals. He removed the effects of dispersion by modeling stress wave propagation in pressure bars using theoretical dispersion relations. This method helped correct SHPB problems. Follansbee [28] continued to study the wave-propagation problem in SHPB focusing on the origin and nature of oscillations. He found that Pochhammer-Chree oscillations could be remove from strain gage records for improved stress-strain curves. In 1990, Gong and Malvern [29] turned back to the problem of dispersion, which rides on the top of the main pulses. They used Fast Four Transform (FFT), a Fourier series, to build the numerical schemes, and then applied them to test concrete specimens. Results collected showed few oscillations in the stress-strain curves verifying the advantage of the method. In 1994, Lifshitz and Leber [30] presented basic principles of analyzing data to get accurate stress strain responses, and pointed out the influence of sound velocity on their results.

2.1.2. Fundamental equations

Using SHPB technique to determine stress-strain relations of any material is based on the principle of one-dimensional (1D) elastic wave propagation [31] The subscripts 1 and 2 donate for interfaces between incident bar and specimen, and specimen and transmitted bar, respectively. Subscripts I, T, R present the incident, transmitted and reflected pulses, respectively. 1-D elastic wave propagation is given as:

$$\frac{\partial^2 u}{\partial x^2} = \frac{1}{c_{OB}^2}\frac{\partial^2 u}{\partial t^2} \tag{1}$$

Where C_{OB} is the bar sound velocity.

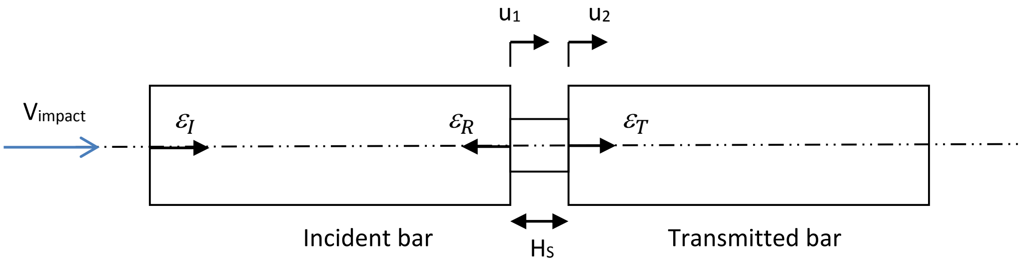

Fig. 2.1: Traditional 1-D SHPB analysis

The incident bar and solution of equation (1) is given by using D'Alembert's method as follows:

$$u_1 = f(x - c_{OB}t) + g(x + c_{OB}t) = u_I + u_R \tag{2}$$

Where, f and g are arbitrary functions.

Strain in incident bar: $$\varepsilon_1 = \frac{\partial u_1}{\partial x} = f' + g' = \varepsilon_I + \varepsilon_R \tag{3}$$

Particle velocity at the incident-specimen interface is:

$$\dot{u}_1 = \frac{\partial u_1}{\partial t} = -f'.c_{OB} + g'.c_{OB} = c_{OB}(g' - f') = c_{OB}(\varepsilon_R - \varepsilon_I) \tag{4}$$

For transmitted bar, solution of equation (1) given by using D'Alembert's method as follows:

$$u_2 = h(x - c_{OB}t), \tag{5}$$

Where h is an arbitrary function.

Strain in transmitted bar: $$\varepsilon_2 = \frac{\partial u_2}{\partial x} = h' = \varepsilon_T \tag{6}$$

Particle velocity at the specimen-transmitted interface is:

$$\dot{u_2} = \frac{\partial u_2}{\partial t} = -c_{OB}.\,\varepsilon_T \tag{7}$$

If the elastic stress wave propagation in the specimen is neglected, [32] give the average strain rate in the specimen:

$$\dot{\varepsilon_s} = \frac{(\dot{u_1} - \dot{u_2})}{H_s} = \frac{c_{OB}}{H_s}(-\varepsilon_I + \varepsilon_R + \varepsilon_T) \tag{8}$$

Where, H_s is the instantaneous length of the specimen.

By definition given in [32], the forces in incident and transmitted bars are:

$$F_1 = A_B E_B(\varepsilon_I + \varepsilon_R) \tag{9}$$

And $$F_2 = A_B E_B \varepsilon_T \tag{10}$$

Where A_B is the cross-sectional area of both incident and transmitted bars, E_B is elastic modulus of the bars.

If forces on front and rear surfaces of specimen are in equilibrium state ($F_1 = F_2$), then:

$$\varepsilon_I + \varepsilon_R = \varepsilon_T \tag{11}$$

Substituting (11) into (8), the average strain rate in specimen is:

$$\dot{\varepsilon}_S = \frac{2c_{OB}\varepsilon_R}{H_s} \tag{12}$$

Average true stress in the specimen is given by:

$$\sigma(t) = \frac{A_B E_B \varepsilon_T}{A_S} \tag{13}$$

Where, A_S is instantaneous cross-sectional area of the specimen.

The expressions for average engineering stress and engineering strain of the specimen:

$$\sigma_s(t) = \left(\frac{A_B E_B}{A_{so}}\right). \varepsilon_t(t) \tag{14}$$

$$\varepsilon_s(t) = \left(\frac{2c_{OB}}{H_{SO}}\right). \int^t \varepsilon_R(t)dt \tag{15}$$

2.1.3. Assumptions for a valid SHPB test

Gama [33] and Gray [34] review assumptions needed for the SHPB test. Basically, solutions [35] and [36] for average engineering stress and strain in the specimen are solved following the principle of 1-D elastic wave propagation, therefore the SHPB bar system (incident and transmitted bars) must have characteristics specific for generating 1-D elastic wave propagation during the test. To satisfy this condition, we require a 1-D stress wave propagation happens in a thin, long rod with the homogeneous, isotropic, linear elastic and uniform characteristics in cross section over the entire length of the incident and transmitted bars. In addition, to ensure 1-D wave propagation in the sample the stress equilibrium condition stated in eq.11 must be achieve. Furthermore, for a valid 1-D dynamic response of a sample we must also obtain a constant strain rate in the specimen.

2.1.4. Manufacturing Methods of Aluminum Foams

There are number of processing methods that are currently used to manufacture foams. These include foaming liquid melts, metallic precursors, foaming of powder compacts and ingots containing blowing agents. Metal foam manufacturing processes can be classified in two groups direct and indirect foaming methods. Direct foaming method are liquid state processing methods. These processes start from a molten metal containing uniformly dispersed ceramic particles to which gas bubbles are injected directly, or generated chemically by the decomposition of a blowing agent (e.g. titanium hydride, calcium), or by precipitation of gas dissolved in the melt by controlling temperature and pressure. However, control of pore size is rather difficult to achieve. In principal air, water vapor or any inert gas can be used for this purpose. Generally, air, oxygen, nitrogen and argon gases are being used for this purpose. For industrial production of metallic foams, all three methods are used. However, decomposition of foaming agent in the liquid melt affords superior structural control compared with the other two. The indirect foaming method or solid-state processing methods are powder metallurgical processes require the preparation of foamable precursors that are subsequently foamed by heating. The foamable precursor consists of a dense compacted of powders, where the blowing agent particles are uniformly distributed into the metallic matrix.

2.1.5. Foaming by Liquid Metals

Metallic foams can be produced by creating gas bubbles in the liquid provided that the melt has been prepared such a manner that the emerging foam is fairly stable during foaming process. This can be done by adding fine ceramic powders or alloying elements to the melt, which form stabilizing melt, or by other means. Currently there are three known ways of foaming metallic melts: (i) gas injecting into the liquid metal, (ii) gas releasing by blowing agent’s addition and dissociation at molten metal temperature and (iii) dissolved gas precipitation

2.1.6. Foaming by Melt Gas Injection Air Bubbling

Varies from 10% to 20%, and the mean size of the particles ranges between 5 µm and 20 µm. This process allows the production of closed-cell foams of 1 m wide to 0.2 m thick slabs (37). The first manufacturing method of foaming aluminum and aluminum alloy melts is based on gas injection into molten metal (Figure 2.3). Alcan N. Hydro Aluminum in Norway and Cymat Corporations in Canada are the manufacturers, which apply this method to produce Al foams. During this process, SiC, aluminum oxide or magnesium oxide particles are used to enhance the viscosity of the liquid metal and adjust its foaming properties because liquid metals cannot easily be foamed by bubbling air through them. Drainage of the liquid down the walls of the bubbles occurs quickly and the bubbles collapse. However, if a small percentage of these particles are added to the melt, the flow of the liquid metal is impeded sufficiently to stabilize the bubbles. In the next stage, the gas (air, argon or nitrogen) is injected into molten aluminum by using special rotating impellers or air injection shaft or vibrating nozzles, which constitute gas bubbles in the melt and distribute them uniformly and easily through the melt (Gibson and Simone 1997). The base metal is usually an aluminum alloy. The volume fraction of particles.

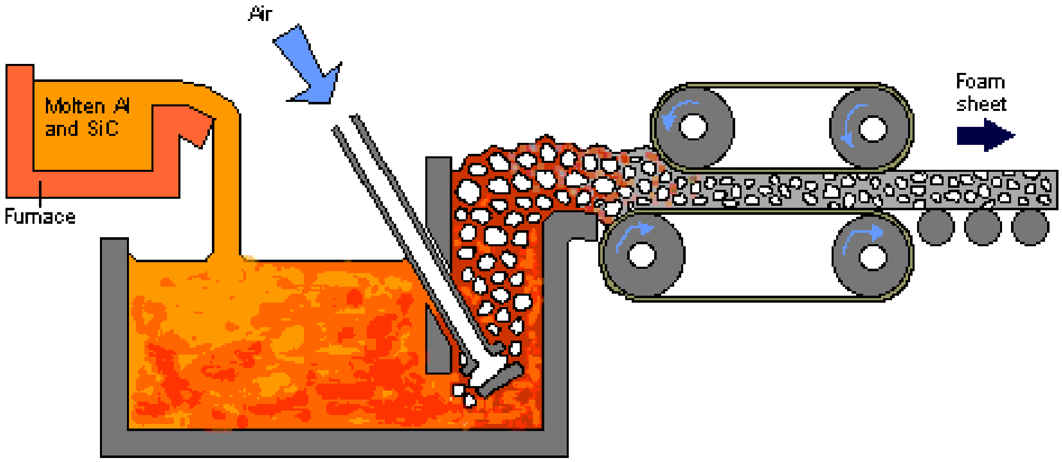

Fig.2.2. schematic diagram of manufacturing of Al foam by melt gas injection method.

The foam is relatively stable owing to the presence of ceramic particles in the melt. The resultant viscous mixture of bubbles and melt floats up to the surface of the liquid where it turns into fairly dry liquid foam as the liquid metal drains out. A conveyor belt is used to pull the foam off the liquid surface, and is then left to cool and solidify. Many non-metallic reinforcements react with molten metal including alumina, boron carbide, silicon carbide, silicon nitride and boron nitride, but silicon carbide is preferred material in practice. Silicon carbide reacts with molten aluminum and forms aluminum carbide and silicon. It has been established that the rate of this reaction can be reduced to an acceptable level by holding the melt at a relatively low temperature during mixing, coating the particles, and inhibiting the reaction by raising the Si content of the aluminum melt. Foaming of melt by gas injection process is the cheapest one among all others, and the only one to have been as a continuous production. Foam panels can be produced at rates of up to 900 kg/hour. Typical density, average cell size and cell wall thickness are 0.069-0.54 g/cm3, 3-25 mm, and 50-85 µm, respectively. Average cell size, average cell wall thickness and density can be adjusted by varying processing parameters including gas injection rate and rotating shaft speed. The main disadvantage of this process is the poor quality of the foams produced. The cell size is large and often irregular, and the foams tend to have a marked density gradient. Although various methods have been developed to improve the drawing of the foam, the size distribution of the pores is still difficult to control. The foamed material either is used directly with a closed outer surface, or is cut into the required shape after foaming. Although having high content of ceramic particles, machining of these foams can be problematic.

2.1.7. Foaming Melts with Blowing Agents

Adding a blowing agent into the melt is the way of foaming melts. The blowing agent decomposes under the influence of heat and releases gas, which then propels the foaming process. Shinko Wire Co., Amagasaki (Japan) has been using this foam production method since 1986 (38, 39). The method is shown schematically in Fig.2.4. In the first stage of the foam production, about 1.5wt.% calcium is added to the aluminum melt at 680 °C. The melt is then stirred for several minutes during which the viscosity of the melt continuously increases by a factor of up to 5 owing to the formation of oxides, e.g. $CaAl_2O_4$, which thicken the liquid metal. Calcium volume fraction and stirring time effects on the viscosity of an Al melt. Upon reaching an optimum viscosity of the melt, titanium hydride is added in an amount typically 1.6 wt.%, which acts as a blowing agent according to the following reaction:

$$\mathbf{TiH_2\ (s) \rightarrow Ti\ (s) + H_2\ (g)}$$

The melt starts to expand slowly and gradually fills the foaming vessel. The whole foaming process can take 15 minutes for a typical batch of about 0.6 m^3. After cooling the vessel below the melting point of the alloy, the liquid foam turns into solid aluminum foam and can be taken out of the mold for further processing.

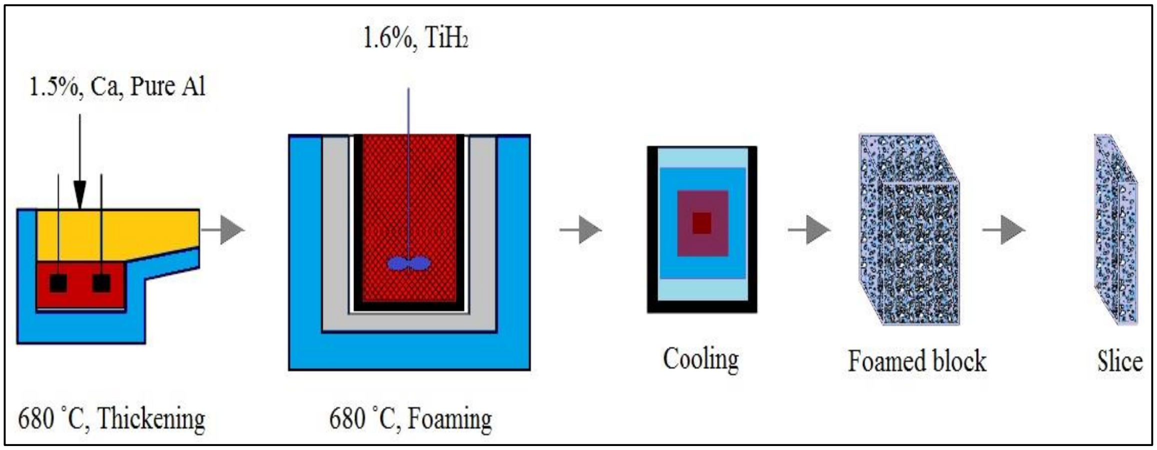

Fig. 2.3. The process steps of aluminum foam forming
by gas releasing agent, Alporas process.

Alporas foam manufactured in this way, has very uniform pore structure and do not require the addition of ceramic particles which makes the foam brittle. However, the method is more expensive than foaming melts by gas injection method owing to more complex processing equipment's are needed.

2.1.8 Gas-releasing particle decomposition in semi-solids (Alulight Process)

The process starts with the mixing of metal powders - elementary metal powders, alloy powders or metal powder blends - with a powdered blowing agent, after which the mix is compacted to peak a dense, semi-finished product (Figure 2.5). Besides metal hydrides (e.g., TiH_2, ZrH_2), carbonates (e.g., calcium carbonate, potassium carbonate, sodium carbonate and sodium bicarbonate), hydrates (e.g., aluminum sulphate hydrate and aluminum hydroxide) or substances that evaporate quickly can also be used as blowing agent. Compaction techniques include uni-axial or isostatic compression, rod extrusion or powder rolling. Extrusion can be used to produce a bar or plate and helps to break the oxide films at the surfaces of the metal powders. Foaming agent decomposes and the material expands by the released gas forces during the heating process (350– 450C) thus a highly porous structure is formed. Several groups, notably IFAM in Bremen, Germany, LKR in Randshofen, Austria, and Neuman-Alu in Marktl, Austria, have developed this approach (40). The manufacturing process of the precursor has to be carried out very carefully because residual porosity or other defects will lead to poor results during further processing. The precursor material could be processed into sheets, rods, profiles, etc. by conventional techniques. The mixture of powders, metal powder and foaming agent, was cold compacted and extruded to give solid metal material containing a dispersion of powdered foaming agent. When this solid was heated to the metal's melting temperature, the foaming agent decomposes to release gas into the molten metal, creating a metal foam. During this process, cooling the foam is a problem since after heating the precursor for foaming; the heat source could be turned off quickly. However, the metal would still be hot, and is prone to collapsing back into molten metal before it solidifies. Water-cooling or heating the foam only locally may avoid this problem; however, the problem may become a significant challenge for the reliable foam production. The foam has a closed-cell structure with pore diameters in the range of 1 mm to 5 mm.

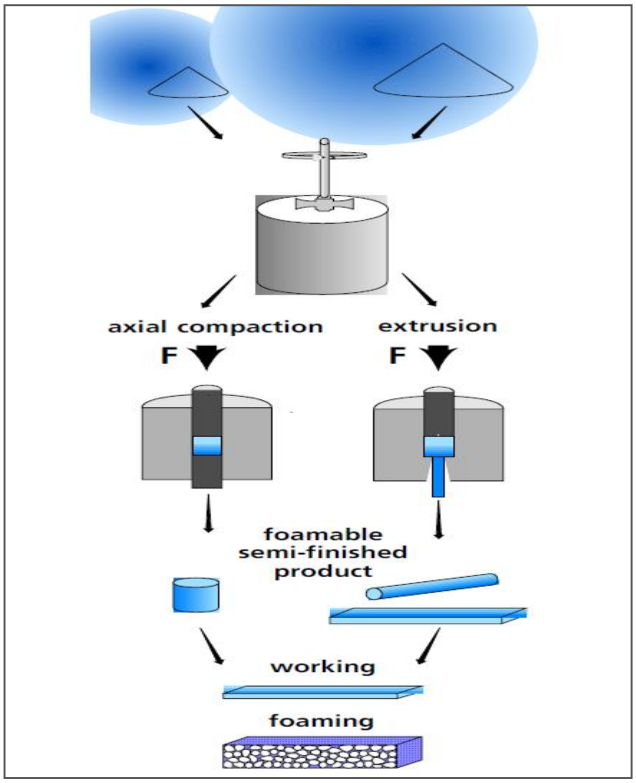

Fig 2.4. Schematic diagram showing the powder compact foaming process (Alulight Process)

2.1.9 Stability of metal foams

Foams are unstable systems because their large surface area causes energy to be far from a minimum value. Foams can therefore be, at the most, metastable, constantly decaying at a certain rate. Aqueous and non-aqueous foams are stabilized by surfactants which form a dense mono layer on a foam film. Such layer reduces surface tension, increase surface viscosity, and create electrostatic forces (the so-called disjoining forces) to prevent a foam film, from collapsing. Metallic foams must be stabilized by different means because there are no surfactants and electrostatic forces are seen in metals. Like water, pure metallic melts cannot be foamed but additives are required to act as stabilizers to create foam. Therefore, foam can be said to be (Kinetically) stable, if it does not change considerably in the time span between completion of the blowing process and solidification. The forces acting on foam are (i) Gravity, (ii) External atmospheric and internal gas pressure, (iii) Mechanical forces, (iv) Forces from within the metallic phase. Any imbalance of these forces will lead to a movement of foam. Changes in foam morphology can be classified according to the terms given in Fig. 2.2. This morphology can be explained in more detail as physics of foams. Physics of foams comprises of many phenomena associated with their birth, life and death in terms that bubble formation is considered as the birth of foams and drainage as their death. Flow may be defined as the movement of bubbles with respect to each other by external forces or changes in the internal gas pressure e.g. during foaming. Drainage is one of the driving forces for the temporal instability of molten metal foams. For usual aqueous foams this phenomenon is well examined and understood on both the experimental and the theoretical side.

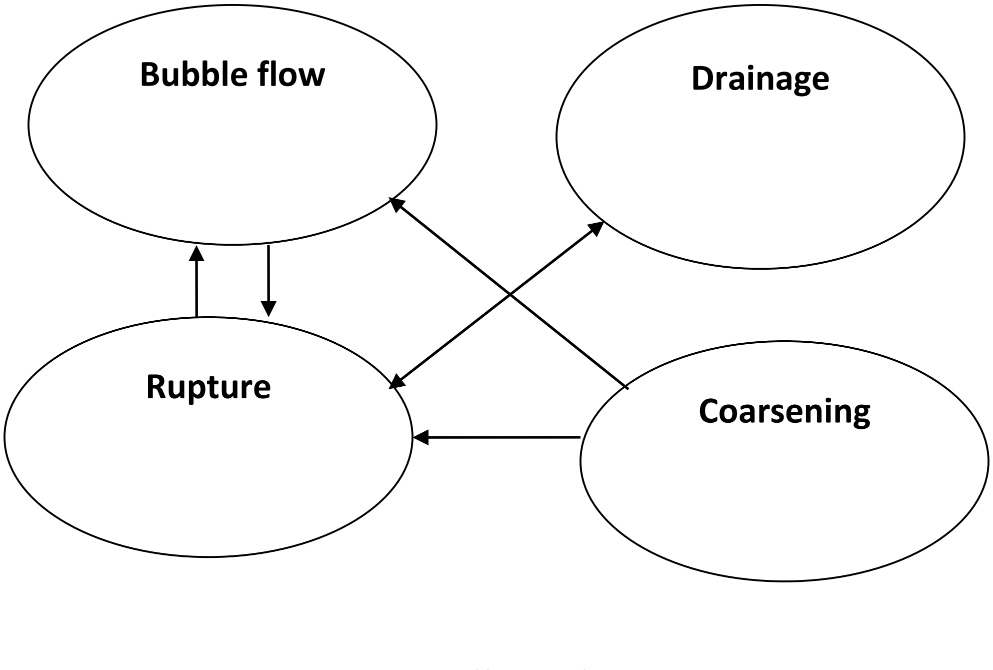

Fig. 2.5 Parameter effecting foam morphology

The situation is different for metallic foams. Due to their opaque nature, the observation of drainage is only possible by either measuring the density distribution of solidified samples *ex situ* or by x-ray or neutron radioscopy. Up to now there exists just one theoretical study describing the drainage behavior of metallic foams incorporating the drainage equation, the temperature dependence of the viscosity and thermal transport. During the formation of closed cell foam, stable liquid foam balances surface tension at the liquid-gas interface and the weight of the liquid cell walls with the air pressure within the cells. A simple force balance indicates that an increase in the air pressure decreases the cell size. At cell edges, where cell walls meet, surface tension forces cause the liquid-gas interface to be curved in an arc called a Plateau border. This causes the fluid pressure at the cell edge to be lower than that in the cell wall, drawing liquid from the cell walls into the cell edges. Gravitational forces then cause drainage of the liquid through the cell edges. During drainage, the Plateau borders decrease in size and the cell walls of the liquid foam become thinner. In a pure liquid with no impurities, the surface tension is generally too strong to be balanced and the cell wall immediately bursts. In order for liquid foam to become stable, the liquid gas interface in each cell must be altered in order to reduce the influence of surface tension. A liquid foam can be stabilized either by introducing a surfactant which lowers the surface energy of the liquid-gas interface or by increasing the viscosity of the surface layer. A cell wall in stabilized liquid foam will drain until it reaches some critical thickness and then stop. Completely drained liquid foam, called dry foam, therefore has cell walls of nearly uniform thickness and small Plateau borders (3)

2.1.10. Compressive Deformation Behavior of Al foam.

In the past few years, there has been a considerable interest in using lightweight metal foams for structural components and energy absorption parts in automobile, railway and aerospace industries (41-43). In these applications, the foam would be subjected to high strain rate deformation. Designing of these components it demands a full characterization of their mechanical properties under a wide range of strain rates. The quasi-static mechanical properties of aluminum alloy foams, such as compressive strength, tensile strength and elastic modulus, have been extensively studied and reviewed (44-47). However, related work under dynamic conditions has been relatively limited due to the difficulty in characterizing the high strain rate behaviour of aluminum alloy foams (48). A servo hydraulic machine is common and convenient, but it is limited to lower strain rates (below 10s-1ec). A drop weight impact test can be used for different specimen geometries and allows easy variation of strain rate. However, the system is very sensitive to the contact conditions between the impactor and specimen (49). The compressive stress-strain curve of Al alloy foams, either quasi-static or dynamic compression, exhibits three distinct deformation regions, an initial linear-elastic region; a flat plateau region with a nearly constant flow stress, sometimes an upper and lower peak point can be observed; and a final densification region representing collapsed of cells in to compacted mass. These deformation characteristics of the Al alloy foams are similar to those of other metal foams (50-51-46).

Metal foams have also showed usefulness in crashworthiness and blast resistance applications (52). Using metal foam in crashworthiness and blast resistance applications one has to study the foam material under dynamic loading condition which required Split

Hopkinson Pressure Bar test unit. In the recent past several researchers have studied Al foam at different strain rate right from quasi –static to high strain rate i.e., in the range 0.0001s-1 to 5000s-1 (53-65). It was observed that their results are conflicting. Some researchers have studied the compressive deformation behavior of Al foam and found that compressive strength is independent of strain rate (53-56). However, some researchers studied the Al foam at different strain rates and reported that plastic strength increases with strain rate (57-62,64). Wang et al [65] developed the elasto-plastic constitutive model of aluminum alloy foam subjected to impact loading. Recently, interest has been shown to study of compressive behavior of syntactic foam (66-69) and foam filled structure (70-78).

2.1.11 Application of Aluminum Foam

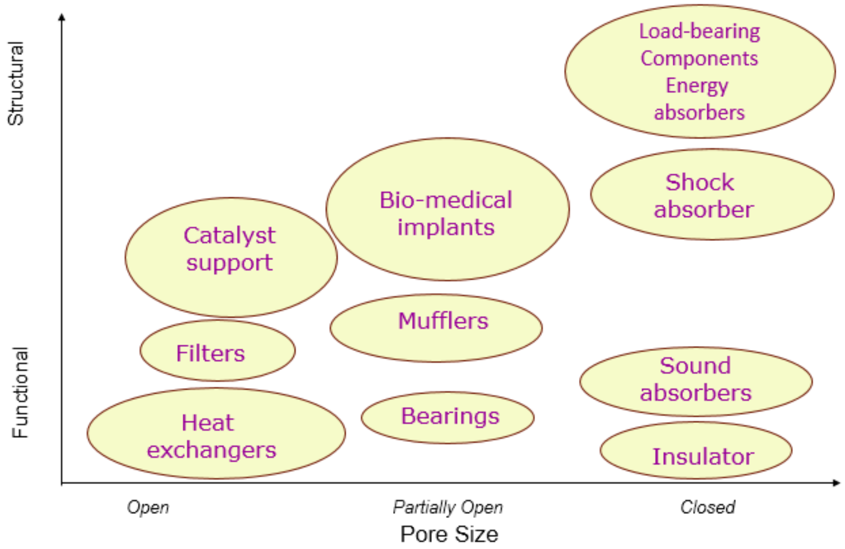

Fig. 2.6. Applications of cellular metals grouped according to the degree of ‘‘openness’’ Needed and whether the application is more functional or structural.

The important nature of these metallic foams is that they possess excellent specific strength. Therefore, aluminum, magnesium or titanium foams or porous metals are preferred for such applications. For medical applications, titanium maybe preferred because of its compatibility with tissue. Stainless steel or titanium is required for applications where aggressive media are involved or high temperatures occur. Fig 2.6 shows the application of Al foam grouped according to the openness.

2.1.12. Structural Applications

Lightweight materials with high stiffness are often desired for various applications. Standard products on the market, like honeycomb panels, use a cellular structure as the core and brazed or glued face sheets to provide the desired properties. They are usually inexpensive, but have some disadvantages, as they cannot be curved, resist high temperatures due to the glue nor be recycled. Aluminum foam sandwiches (AFS) and steel aluminum foam sandwiches (SAS) are promising products for structural applications and are already on the market. AFS panels are used as support frames, e.g., for solar panels, mirrors, etc., and where light and rigid metallic panels are needed. Most of the customers prefer to provide the material as panels and manufacture their own products themselves. Often they even keep their innovative field of application in secret to assure a competitive advantage for their products on the market. A good example is industrial machines, where foam-filled beams and columns are stiff, but light. With reduced inertia, they can be moved quickly and positioned precisely. Examples are drilling, milling, textile, cutting, printing, pressing or blanking industrial machines. Additionally, damping of the system and of, e.g., an additional vibrating tool can improve the performance in the precision of positioning and wear, reduce fatigue problems and increase the operational lifetime. An example of an application for a high-speed milling machine (Fig. 2.7) of Niles-Simmons (Chemnitz, Germany) in cooperation with the Fraunhofer-Institut für Werkzeugmaschinen und Umformtechnik (IWU, Chemnitz, Germany) (79)

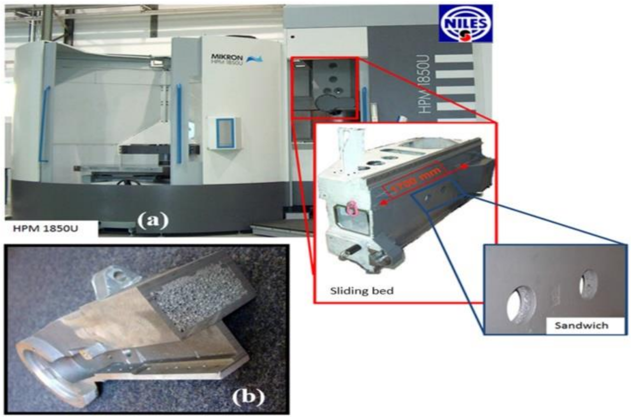

Figure 2.7 (a) Sliding bed of a milling machine made of welded aluminum foam sandwich (courtesy of Thomas Hipke, IWU, Chemnitz, Germany); and (b) a beam of a textile machine filled with Alporas foam (courtesy of the Au Metallgießerei, Sprockhövel, Germany). (79)

The sliding bed is made of 11 welded AFS parts, and the construction is 28% lighter than the cast part with the same stiffness, but improving vibration damping. Around 15 parts per year are manufactured. This part is 1590 mm × 280 mm × 160 mm and provides a 60% reduction in the amplitude at the resonance frequency. The production is ~1000 pieces per year. A similar hybrid material concept was applied to a tool column prototype of the Technical University Prague for a cutting machine (Model Prisma S) from TOS Varnsdorf s.a. (Varnsdorf, Czech Republic) in which an Alporas foam core is integrated.


(a) (b)

Figure 2.8. (a) Prototype of German high velocity train ICE made of welded aluminum foam sandwich; and (b) view of the interior with the low number of components required (courtesy of Thomas Hipke, IWU, Chemnitz, Germany and Voith Engineering, Chemnitz, Germany). (79**)**

We can find aerodynamic noise reduction prototypes in the railway industry, e.g., in pantographs for the Shinkansen train in Japan (Fig. 2.8). There, open cell Al-foam is used for shape smoothing of the pinhead and its support and covering. Applications for aerodynamic noise reduction of jet turbines of airplanes are also under discussion.

2.1.13. Functional Applications

A wide palette of functional applications based on metallic foams can be found on the market. Again, a multi-purpose approach has the best chances to offer a competitive or unique product. Ceilings in auditoriums or large rooms are very often planked with perforated metal sheets for sound control. As an alternative to this traditional construction material, applications of metallic foam panels for sound absorption are already available on the market, offered by different companies. At the open foam surface, the sound waves are guided and redirected to the foam interior, where they are caught and damped after several reflections (Fig. 2.9). The pore size distribution and the different orientations allow for a very effective damping over a broad frequency spectrum. These applications could be considered also as architectural, but we include them here as their main function is sound absorption. They combine the advantage of the lightweight, self-supporting capability of large metallic foam panels made of open cell or just sliced closed cell foams, with a design component.


(a) (b)

Figure 2.9 (a) audience hall, (b) restaurant covered by Alusion foam for sound control (courtesy of Cymat) (79)

Further sound absorption applications made by Alporas foams provided by Shinko Wire (Amagasaki City, Japan) can be found in train rails, metro tunnels, elevators, on the under-side of an elevated highway, etc. Newer products based also on Alporas foams were developed by Foamtech (Daegu, Korea) and applied to concert halls, conference rooms, auditoriums, sport centers and walls and ceilings of the machinery and operating rooms of industrial plants as non-flammable, acoustic absorbers. Further applications can be found in the ship industry, where, e.g., prevention of noise from the engine room, the combustive exhaust pipe and the air cleaning system are provided by foamed inside walls between cabins. Metallic foams are also used by Foamtech for sound absorption in metro tunnels, in the railway and on the tunnel and station walls, where they have to support high air pressure changes and vibration, being at the same time non-flammable.

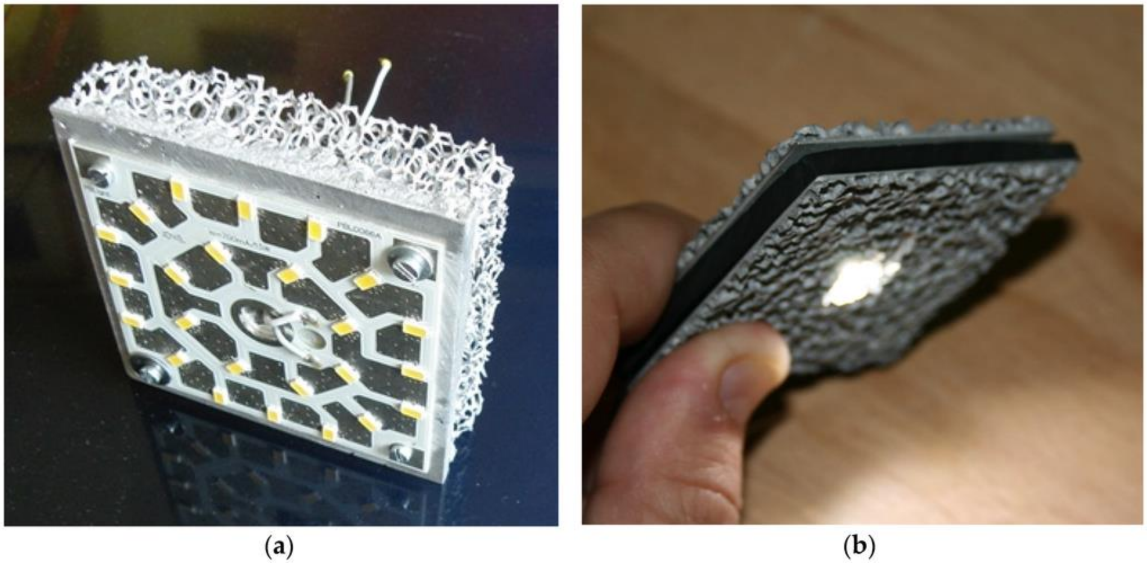
(a) (b)

Figure 2.10 Passive thermal cooling of LED lamps made of Al open cell foam: (a) Al open cell foam from M-pore (courtesy of M-pore); and (b) cut AFS from the Technical University Berlin (79)

Bio-medical applications are another field of interest. Here, high quality products based on Ti-foams provide excellent bio-compatibility properties. The trend goes into the direction of porous structures to improve Osseo integration. where a tomography of a Ti-based dental implant (Fig. 2.11) shows its porous structure. Although Ti is quite difficult to foam, foam-like structures can be created through different production methods. This field should be exploited more deeply in the future.

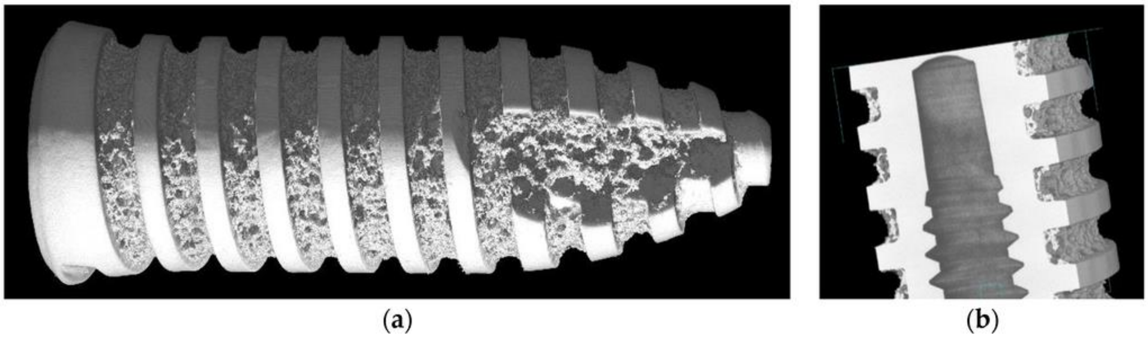

Figure 2.11 (a) Tomography of a Ti-based porous dental implant for Osseo integration improvement; and (b) detail of the inner structure and porous surface (courtesy of Louis-Philippe Lefebvre). (79)

2.1.14. Applications of metallic foams produced through Liquid metallurgy route

- In many cases sponge aluminum has proved itself a good energy absorbing material. It can be used for safety pads in systems for lifting and conveying and also in high-speed grinding machines by using sponge aluminum as an energy absorber.
- Sponge aluminum is also suitable for forming the deformable zones of car bodies in front and behind the passenger compartment so as to improve the safety of car occupants
- Shinko Wire in Japan is the aluminum foam manufacturer has developed vacuum elevator tool manufactured by using aluminum foam through liquid metallurgy (ALPORAS). The tool is used to lift glass panels produced in the floating glass process. The replacement of the full aluminum part by Alporas foam led to a weight reduction from 82 to 32 kg, makes it possible for easy manual handling of the tool.

Fig 2.12. Vacuum lifting tool for Pilkington containing an Alporas aluminum foam ring (79)

- *Alulight* (Austria) is now producing a crash element for an Audi car with 100,000 parts per year. (80)
- *Alcoa* (USA) is a new player in the aluminum foam market. They are producing aluminum continuous foam and make it possible to reduce the cost of the foam.
- Another closed cell aluminum foam part in production is the girder shown in Figure. It contains two Alporas foam cores encased in a cast aluminum alloy produced by low pressure die casting. The part is used in cutting and milling machines and serves as a load-bearing structure with a good vibration damping capacity.

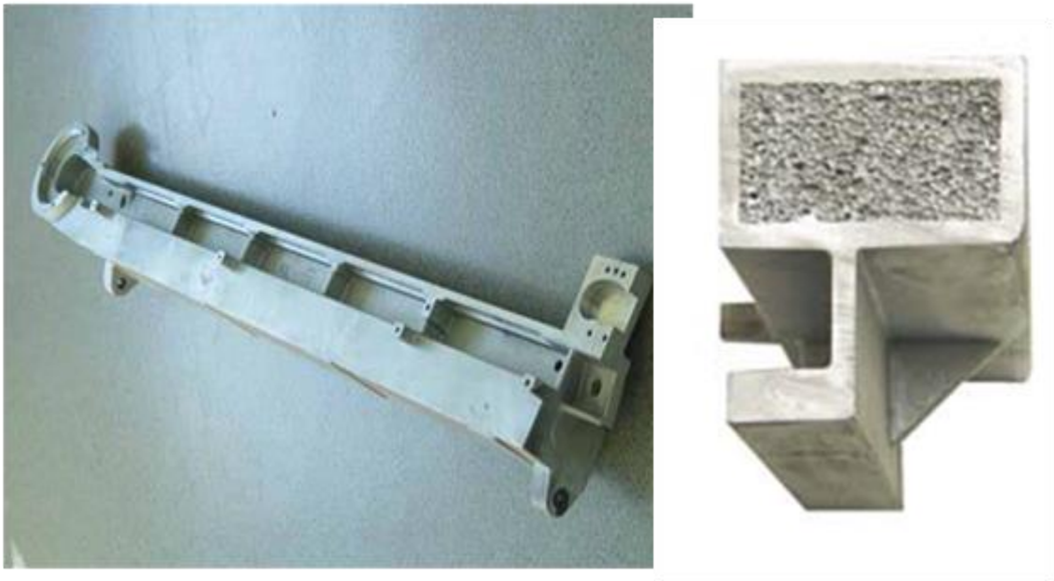

Fig 2.13 Alporas metal foam made of aluminum foam crash element in the front tip of the chassis of a racing car. [80]

2.1.15. Applications of metallic foams produced through powder metallurgy route

1. Boeing (USA) has evaluated the use of large titanium foam sandwich parts made by the gas entrapment technique and aluminum sandwiches with aluminum foam cores for tail booms of helicopters.

2. Copper foam of 5 to 10% density has been reported to out-perform rubber for shock absorbing mounts

3, The most widely used metallic filter materials are porous bronze and porous stainless steel

4. For space applications, the use of highly reactive but very light alloy foams such as Li–Mg foams has been considered Experiments have shown that Ni-Cr alloy foam filled with a solid lubricating composite can be successfully used in the contact seals for a rotating generator in a gas turbine engine

5. Ceramic foams are typically made either by replication techniques (e.g., using a polymer foam as a form) or direct foaming of a liquid in which a ceramic powder is dispersed.

6. Applications for ceramic foams include filters for metal-casting operations, porous-medium burners, and traps for diesel particulate emissions

7. Calcium-phosphate-based foams are being developed for biomedical applications, particularly for bone-graft materials and scaffolds for tissue engineering of bone.

8. Walther et al. presented a process to produce high temperature resistant Fe-Ni-Cr-Al foams using the deposition and transient liquid phase sintering of fine pre-alloyed particles onto thin commercially available nickel foam strip.

9. heat-resistant foams using vapor deposition of Al and Cr (pack-aluminization and chromizing) on nickel foam strips followed by a homogenization treatment to produce Ni-Cr and Ni-Cr-Al foams.

10. Development of porous titanium for the production of dental implants

Fig. 2.14. Crash protector in a model racing car built by students at the University of Technology of Stralsund, Germany; a) view of car with the front encasement taken off. [80]

11. Thin porous coating on metallic foams can be used as in the development of various new and improved treatments (i.e. bone augmentation, graft free vertebra fusion for the treatment of degenerative disk diseases for example).

Fig. 2.15. Porous titanium coating on an acetabular cup for hip replacement (Courtesy of National Research Council Ca4rnada, Industrial Materials Institute) (80)

12. Open-cell materials***:*** ***-***. Vale Inco produces Nickel open cell foams for Electrodes for NiMH and NiCd batteries are probably the largest industrial applications of metallic foams.

CHAPTER 3

Experimental set-up

3.1 Overview of SHPB

In this study, an aluminum SHPB apparatus shown from Fig. 3.1 to Fig. 3.3 was used to investigate the dynamic properties of GR-aluminum composite foam over a range of strain rates. When gas gun launches, the striker bar hits to the incident bar causing an elastic compression wave to travel in the incident bar towards the specimen. When the impedance of the samples is less than that of the bars, an elastic tensile wave is reflected into the incident bar; concurrently, an elastic compression wave is transmitted into the transmitted bar. Strain gages mounted in the middle of incident and transmitted bars collect these waves from incident and transmitted bars, respectively. Specimen response, including average engineering stress and engineering strain, are calculated by using equations (14) and (15).

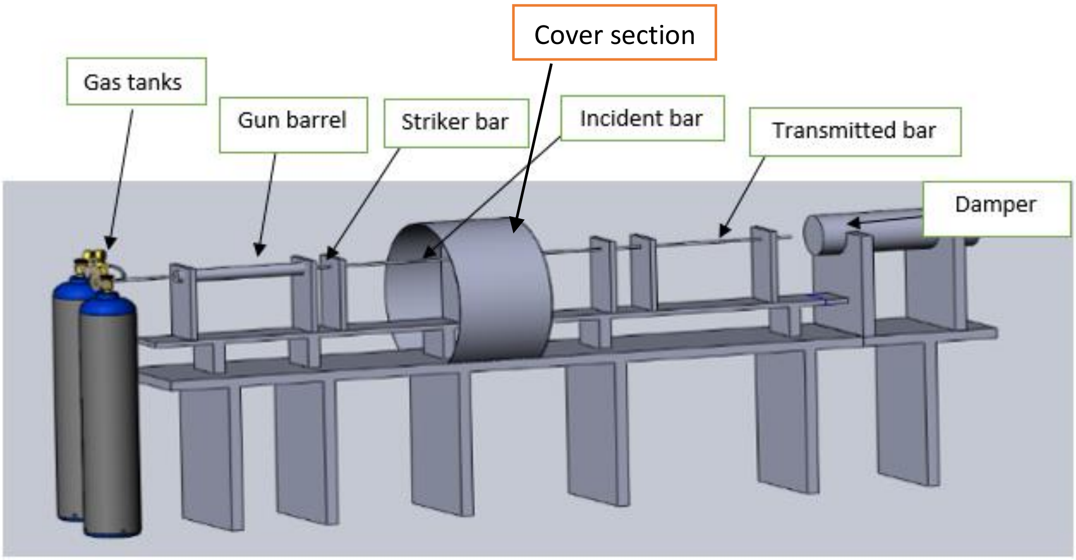

Fig 3.1: A scheme of typical CAD model of compressive Split Hopkinson Pressure Bar apparatus designed in UG-NX_Sourav Das©

Fig 3.2: SHPB apparatus as viewed from transmitter bar end

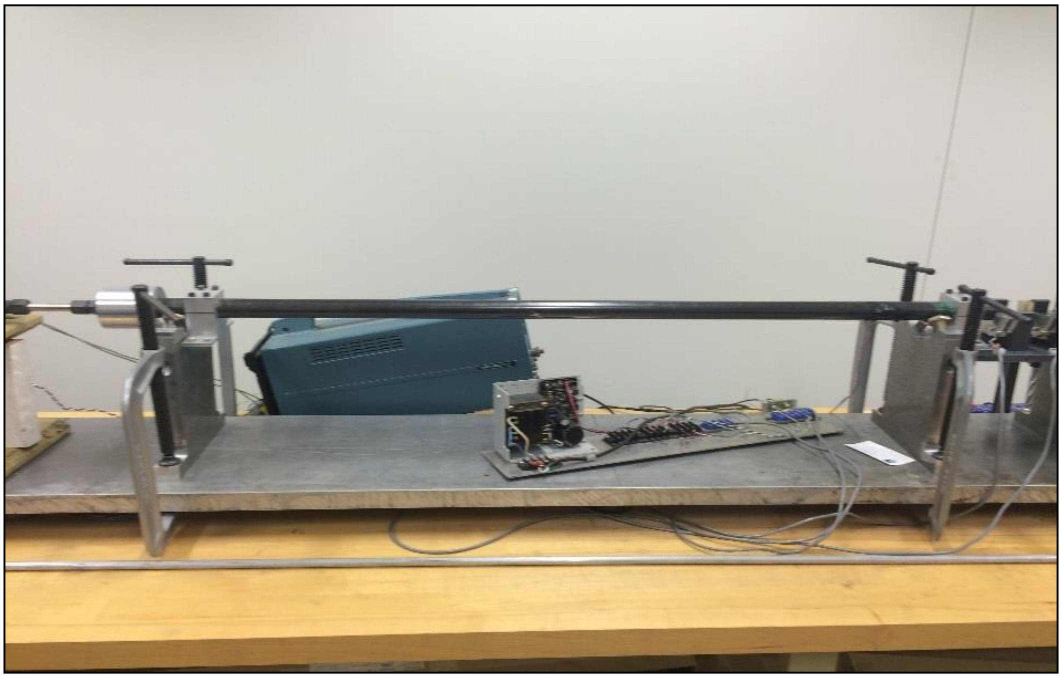

Fig 3.3: SHPB apparatus as viewed from striker bar end

3.2 Details of SHPB

The SHPB apparatus has four main parts:

- Gas launcher assembly
- Pressure bar assembly
- Data acquisition system
- Damping system

3.2.1 Gas launcher Assembly

SHPB works with compressed gas, this assembly is crucially important to the whole SHPB apparatus. It includes the following main components: Solenoid valve, pressure tanks, pressure regulator, and gas-gun barrel.

Solenoid valve

Fig. 3.4 gives a view of a quick-acting solenoid valve. It is connected with two compressed nitrogen tanks by sealed piping and pressure regulator as shown in Fig. 3.5 and Fig. 3.6 respectively. The operating pressure of the value is nearly 2000 psi. The function of a solenoid valve is described as follows. The computerized control system opens the solenoid valve; compressed nitrogen gas is expanded to the gas-gun barrel (see Fig. 3.8) and forces the striker bar out. When the striker bar reaches the end of the gun barrel, it blocks laser beams shining at the sensor, at the end of gun barrel. The interrupting of striker bar through the laser beam causes voltage recorded in system change. Upon recognizing the existence of the striker bar, the control system automatically closes the solenoid valve, to stop compressed nitrogen from releasing.

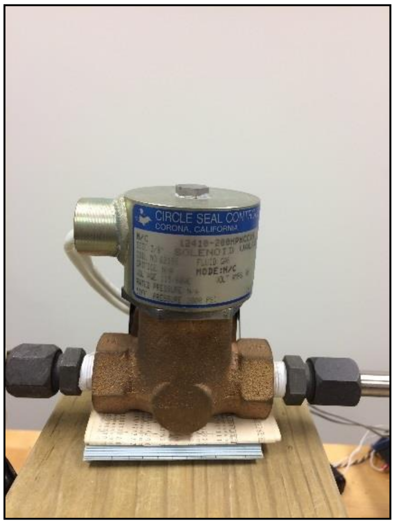

Fig 3.4: Solenoid valve

Pressure tanks

Two high-pressure tanks are connected through sealed piping and pressure regulator as shown in Fig. 3.5. The black tank in Fig 3.5 is a reservoir storing compressed nitrogen gas with maximum pressure of 3000 Psi. The blue tank is used to achieve desired pressure by adjusting the pressure regulator.

Fig 3.5: Two pressure tanks

Pressure regulator

As shown in Fig. 3.6, the pressure regulator includes a pressure adjustment handle and an outlet gage (on the left) and inlet gage (on the right). It shows the current pressure in the tank (inlet gage) and also shows the current pressure value or limits the delivery pressure to the solenoid valve (outlet gage). Using the pressure adjustment handle to reach the desired pressure when the inlet flow is equal to the outlet flow between two tanks, the gas flow is automatically cut off to conform to the optimum pressure. The releasing pressure can be set up to a maximal value of 2000 psi, which is the safe working pressure of the solenoid valve. Because of leakage, after control is set to desired pressure, the pressure may start decreasing; therefore, one must double check pressure before shot.

Fig 3.6: Pressure regulators

Gun barrel

Gun barrel or launching tube, in Fig. 3.7, is one of the crucial components for stress generating. It is made of steel and is in the shape of a hollow cylindrical tube providing the driving force for striker bar. Its ends are screwed onto flanges connecting to the rest of the SHPB apparatus. Dimensions of gun barrel for both aluminum striker bars of 9 inches and 12 inches are 120 mm long, with a 32 mm external diameter and a 20 mm internal diameter.

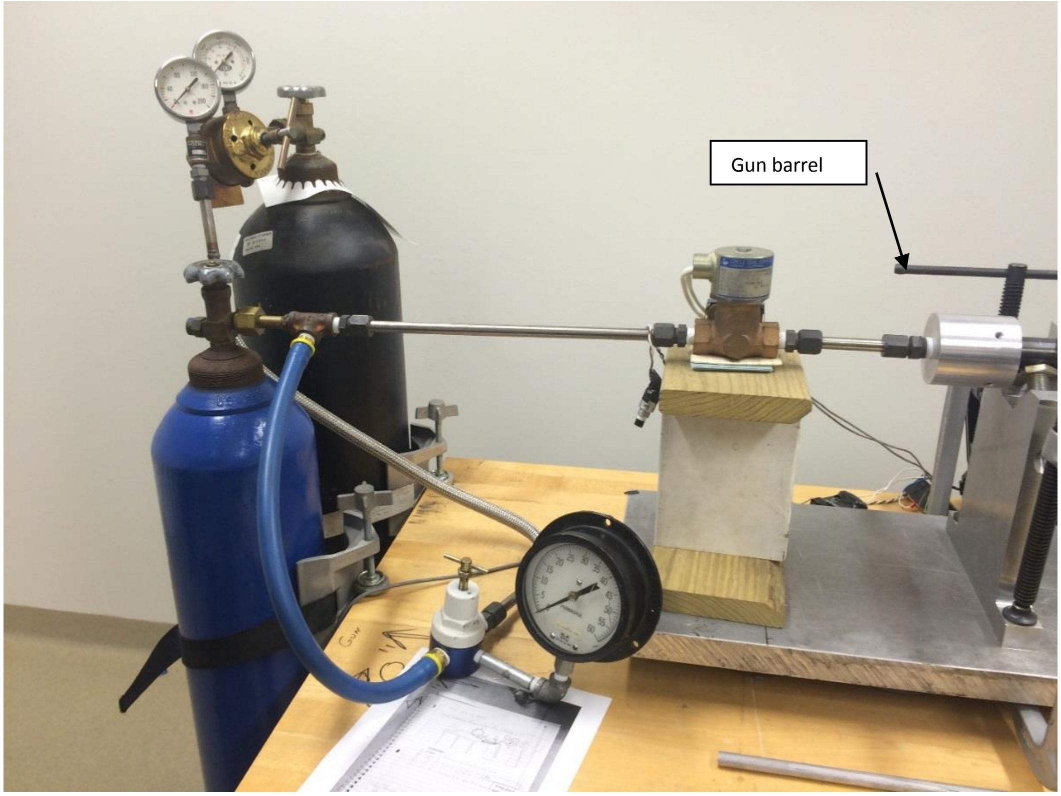

Fig 3.7: Gun barrel (launching tube)

Pipes

Pipes are used to connect the pressure tank to the solenoid valve. They are made from stainless steel with an inner diameter of 0.446 inches and outer diameter of 0.5 inches.

3.2.2 Pressure bar assembly

Pressure bar assembly consists of striker bar, incident bar and transmitted bar made of the same diameter and material. Bar material and bar dimension are the two most important factors of the pressure bar assembly.

An ideal pressure-bar material should have low wave attenuation on both radial and longitudinal dimensions (small Poisson’s ratio) and high sensitivity to signal-to-noise. Besides, signal loss is almost zero. High strength structural material like steel is traditionally used for SHPB bar material; however, the SHPB test will not guarantee accuracy. The reason is due to significant strength differences between the bar and specimen materials. Wave impedance ($\rho.C_0$) of Graphene al foam composite specimen is much lower than that of the al pressure bar; therefore, most of the incident pulse is reflected backward into the incident bar and only a small portion of loading is transmitted through specimen to transmitted bar. As a result, transmitted pulses become very weak. Even if a high strain-gage gain is used, e.g., 500, making it impossible to get the precise and complete transmitted pulses. Even when such small transmitted signals are collected precisely and completely, it is not easy to check stress equilibrium with these signals. In dynamic equilibrium checking, a comparison is made between transmitted signal and the difference of incident and reflected signals. Obviously, the comparison of a very small signals with two large-amplitude ones must be inaccurate.

Another reason for not using the steel bars to test such material is the very short pulse duration of incident pulse. Typically, for a steel bar, the incident pulse duration is less than 10 μs, which is not enough time because the specimen deforms homogeneously before damage. Non-homogeneous deformation in specimen leads to invalid stress equilibrium.

In order to receive fairly large and accurate transmitted signals as well as facilitate stress equilibrium in specimen, low-strength material such as polymer, aluminum, titanium, and magnesium are usually employed, as long as the bar-material strength is higher than specimen-material strength. For SHPB apparatus under investigation, aluminum 7075-T6 was chosen as pressure-bar material with following mechanical properties as shown in Table 3.1 (provided by ASM (Aerospace Specification Metals Inc.). See their website *http://asm.matweb.coms ̄1earch/ SpecificMaterial.7075T6*) for more information. Pressure-bar dimensions will be mentioned in detail in striker bar, incident and transmitted sections.

Table 3.1: Mechanical properties of Aluminum

Mechanical Properties	*Density (kg/m^3)*	*Poisson's ratio*	*Young's modulus (GPa)*	*Shear modulus (GPa)*	*Elongation (%)*	*Peak tensile strength (MPa)*	*Ultimate strength (MPa)*
Aluminum	ρ = 2800	*0.33*	*71.7*	*26.9*	*11*	*503*	*572*

Additionally, since SHPB theory is followed by one-dimensional wave propagation, these bars must be typically straight and freely moved in supporters with the friction as minimized as possible. Besides, the bar system should be aligned perfectly on the common loading axis. The bar ends are designed orthogonal to the common bar axis with high accuracy to ensure good contacts of the striker bar with the first end of incident bar, and the bar ends with specimen.

Striker bars

Striker bars, made of aluminum, 18 inches in length (Fig. 3.8), with diameter of 12.8 mm which is the same to incident and transmitted bar diameter. For a smooth movement, the inside diameter of the gun barrel is slightly greater than the striker bar's diameter as stated in gun barrel section.

Fig 3.8: Striker bar

The striker bar's function is to change the pulse duration in the incident pulse or incident propagating wavelength. The amplitude of the pulse is not only directly proportional to the impact velocity of the striker bar, but also to the length of striker bar. Striker bar velocity changes with pressure. The higher pressure is adjusted, the higher the striker-bar velocity.

Incident and Transmitted bars

These two bars are vital parts of the apparatus as shown in Fig 3.9 (a, b). Incident bar is the one that gets contact directly from striker bar when shot. While the transmitted bar makes contact indirectly despite the fact that in the presence of a small pulse shaper at the front end of incident bar (discussed later in Pulse shaper section) makes the contact indirectly. The energy from the striker bar is transferred almost entirely through the incident bar before reaching the specimen. When the compressive loading pulse in the incident pressure bar meets a specimen sandwiched between two bars, some part of the pulse gets reflected to the incident-specimen interface, while the remainder is transmitted to the second main bar or transmitted bar. Strain gages mounted in the middle of each bar provide magnitude and shape of the incident, reflected and transmitted pulses.

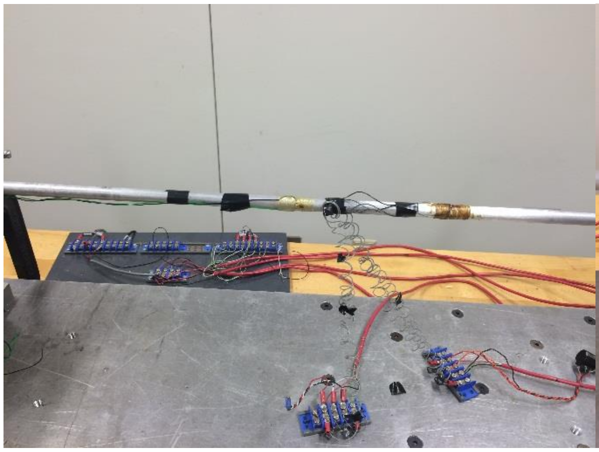

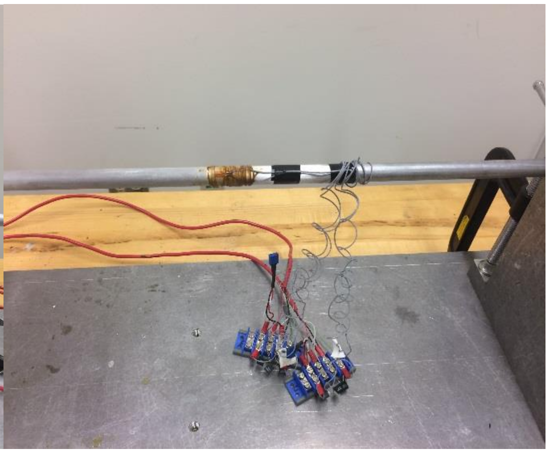

Fig 3.9 (a) Incident bar

Fig 3.9 (b) Transmitted bar

Dimensions of pressure bars including length (l) and diameter (d), are chosen to meet a criteria of 1-D wave propagation for a given pulse length. For experimental measurements on most engineering materials, this propagation requires about 10 bar diameters. Table 3.2 illustrates length and diameter of both incident and transmitted bars. Obviously, the length-to-diameter ratio meets the requirement of 1-D wave propagation which SHPB theory is based on. Additionally, to avoid overlapping between the incident reflected pulses, the incident bar length should be as least twice as long as the striker bar's.

Table 3.2: Dimensions of incident and transmitted bars used in SHPB unit

	Length (mm)	Diameter (mm)	Length-to-diameter ratio
Incident bar	182	12	15.16
Transmitted bar	137	12	11.41

3.2.3. Data acquisition system

Data acquisition system includes strain gage, preamplifier, LabVIEW and sensors as shown in Fig. 3.10.

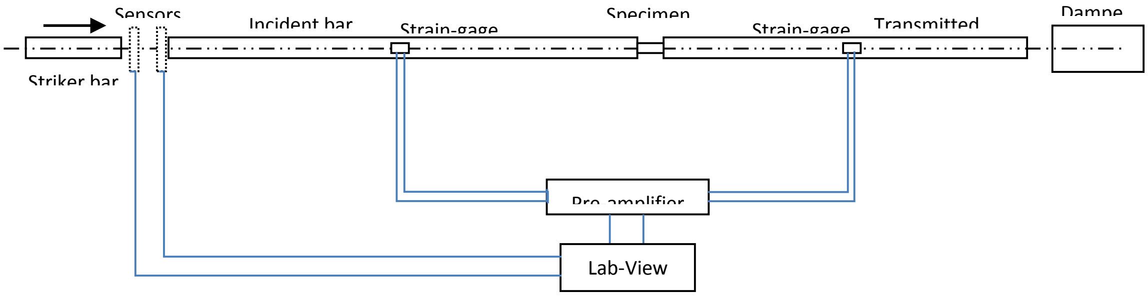

Fig 3.10: A schematic of a data-acquisition system

Strain gage

Strain gage, a device whose electrical resistance varies proportionally to the change of strain, is the most common method of measuring strain because of its convenient size and simple installation.

As shown in Fig 3.11, a strain gage commonly is made from strips of metallic films arranged in a grid pattern. The purpose of using metallic strips is not only to maximize the strain received from the bar during elastic deformation, but also to reduce the possible shear strain and Poisson strain. The grid is attached onto a very thin non-conducting backing (called carrier) which is glued directly on the aluminum bars. After bonded on the bar, the strain gage is tied to keep it unmoved in a fixed position as illustrated.

It is clear that the adhesive between carrier and aluminum bars is very important since it can result in adverse measurement results in cases where the carrier is not properly mounted on the bar. In addition, some errors can come from the fact that the direction of strain gage is not parallel to the common loading axis of bar system (the direction of strain deformation); or the adhesion applied is too thick. Since these errors may happen, calibration tests should be carried out before actual tests to eliminate the influence of these errors on the measurement accuracy. Note that since each strain gage has a particular limit on elastic deformation, if applied load is larger than that limit, plastic deformation will ruin the strain gage. Therefore, strain gage elastic limitation needs to be chosen so that it can stand allowed deformation of the bar, in order to avoid destroying the strain gage with too large of a strain.

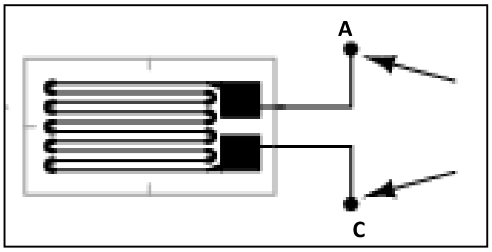

Fig 3.11: Strain gage

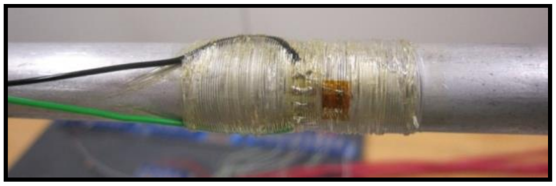

Fig 3.12: A view of strain gage on the incident bar

The black and green wires in Fig 3.12 correspond to point A and C in Fig 3.11, they link to resistances to measure the electrical change in the strain gage. The circuit employed to measure such small changes in resistance is popularly known as a quarter-bridge circuit in which four resistances are arranged as shown in Fig 3.13. At the beginning, R_1 and R_3 are set up equal to each other, while R_2 is set with a value equal to strain gage resistance; hence, without applied force the quarter-bridge circuit is symmetrical and a voltmeter will indicate zero point at this status. However, when the bar is loaded with compressive or tensile forces, metallic strips deform elastically. As a result, the value shown in the voltmeter is not zero because of the decrease or increase of strain gage resistance, respectively.

Equation of $\frac{V_0}{V_{EX}}$ as a function of strain is (*Source: http://www.ni.com/white-paper/3642/en*):

$$\frac{V_0}{V_{EX}} = -\frac{GF.\varepsilon}{4}\left(\frac{1}{1+GF.\frac{\varepsilon}{2}}\right) \tag{16}$$

Typically, strain gage resistance ranges from 120Ω to 2kΩ. The value of the strain gage used here is 350Ω. The distance between strain gage and other resistances is considered as resistances in two black and green wires; however, these resistances are not counted when calculating the circuit. This type of error will be covered in calibration tests.

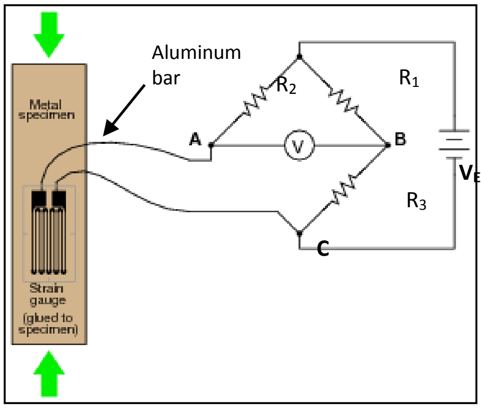

Fig 3.13: A quarter-bridge strain-gage circuit

A fundamental parameter of strain gage presented the sensitivity to strain, defined as the ratio of fractional change in electrical resistance to the fractional change in length is gage factor (GF).

$$GF = \frac{\Delta R/R}{\Delta L/L} = \frac{\Delta R/R}{\varepsilon} \tag{17}$$

Strain gage with GF = 2.07 is used for this SHPB.

In Fig. 3.14(a, b), show data collected from strain gages mounted on Incident and Transmitted bars are shown.

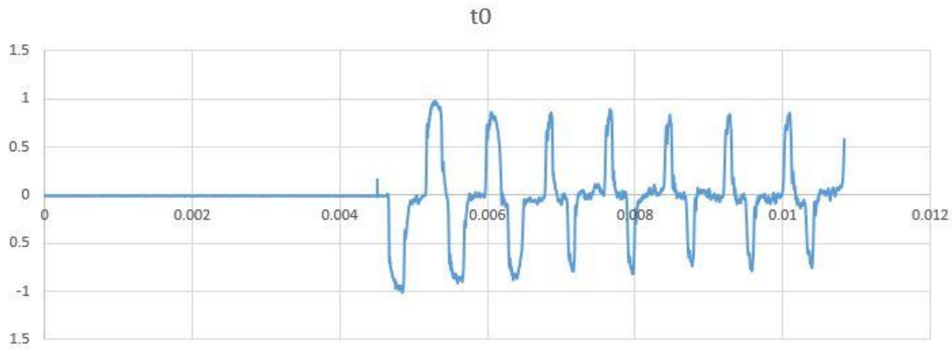

(a) Incident and Reflected signals

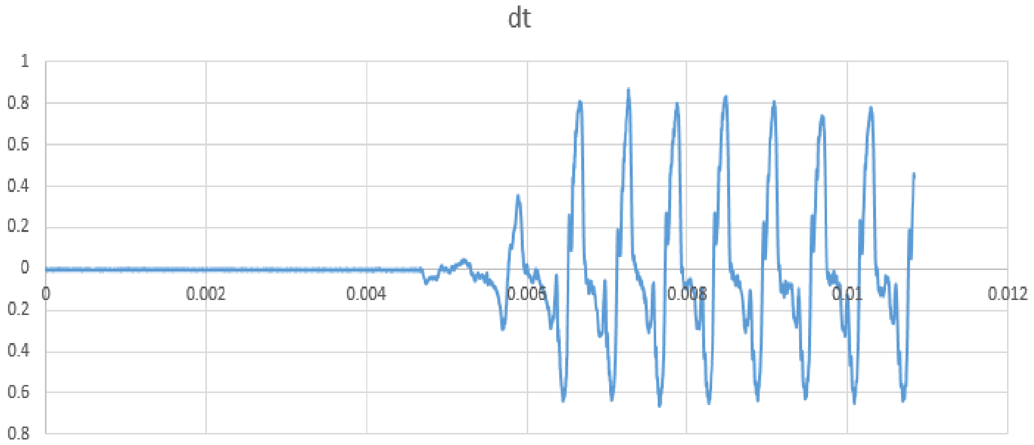

(b) Transmitted signals

Fig. 3.14: Data collected from strain gage on: (a) Incident bar and (b) Transmitted bar

Differential preamplifier

Since the signals collected from the strain gages are in milli volts, it hinders the accurate measurement at these low-magnitude voltages; hence, a differential preamplifier and oscillator are necessary to facilitate the measurement. This research used a Tektronix

ADA400A Differential Preamplifier shown in Fig 3.15 with upper bandwidth filters of 100Hz, 3kHz, 100kHz and Full (>1MHz). As mentioned in [47], the preamplifier and oscillator should be the types with high frequency response to record signal, at least 100Hz. However, when the filters are applied with 3kHz or 100Hz, the recorded signals are not distorted, especially in level of 100 Hz, signals are changed totally, while the results in 100kHz provide rectangular shaped signals. Therefore, following the suggestion, the preamplifier is applied with 100kHz to obtained desired signal shapes.

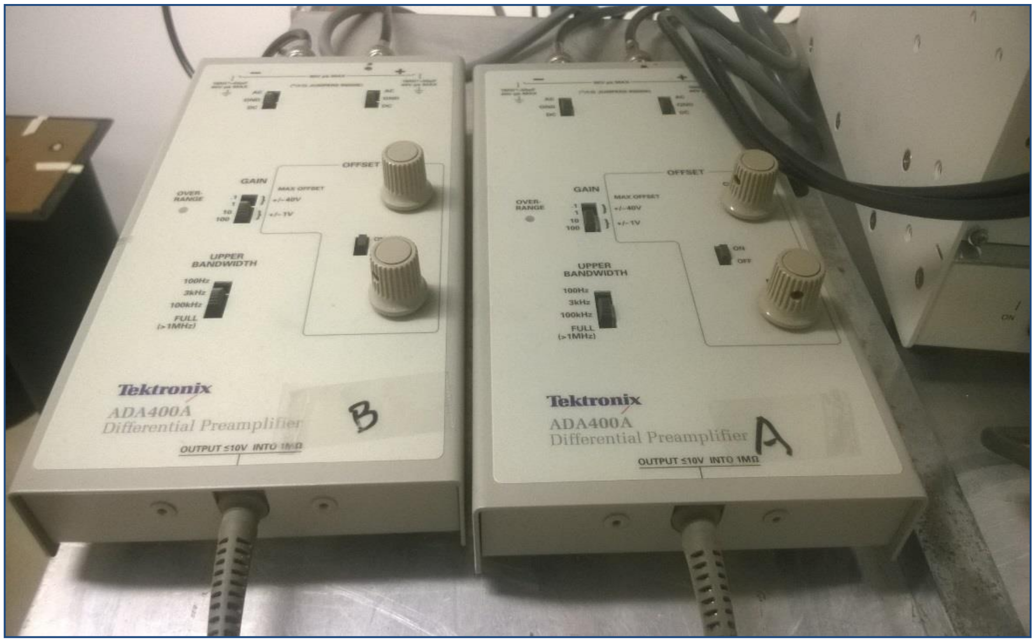

Fig 3.15: Differential Preamplifier of SHPB

LabVIEW

LabVIEW is a graphical programming environment designed for measurement, test, and control systems. In this study, a National Instruments PXI-1002 combined with a PC running LabVIEW to gather and report the experimental data. In Fig. 3.16, LabVIEW shows essential constants of SHPB testing and incident & reflected window, transmitted window and laser-data window.

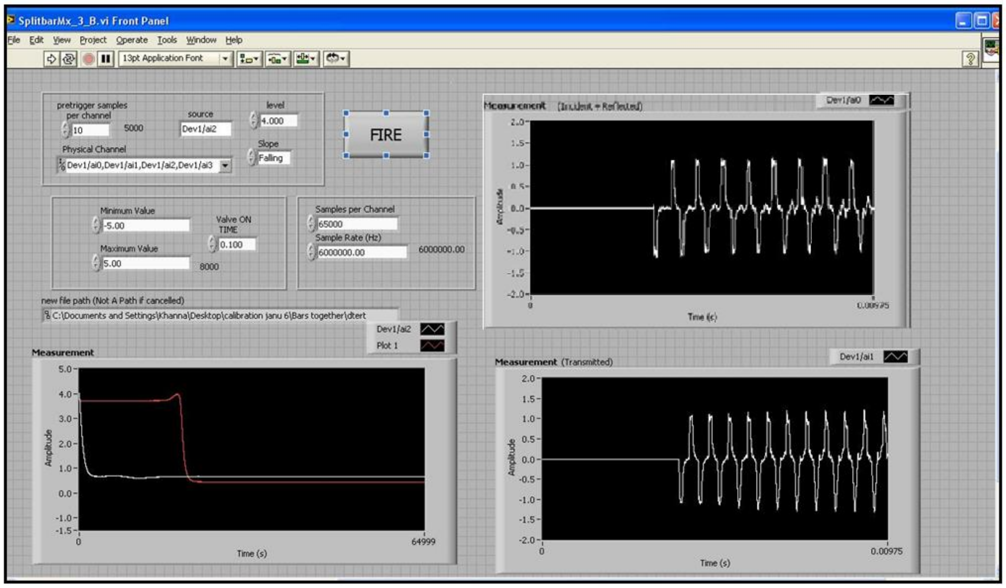

SplitbarMx_3_B.vi Front Panel

pretrigger samples per channel: 10 5000
source: Dev1/ai2
level: 4.000
Slope: Falling
Physical Channel: Dev1/ai0,Dev1/ai1,Dev1/ai2,Dev1/ai3
Minimum Value: -5.00
Maximum Value: 5.00 8000
Valve ON TIME: 0.100
Samples per Channel: 65000
Sample Rate (Hz): 6000000.00 6000000.00
new file path (Not A Path if cancelled): C:\Documents and Settings\Khanna\Desktop\calibration janu 6\Bars together\dtert

Fig 3.16: Experimental data presented on LabVIEW

Sensors

Fig 3.17 gives a view of two sensors positioned in SHPB apparatus. As described in solenoid valve section, when the solenoid valve opens, nitrogen gas pushes the striker bar out. Until the striker bar blocks the laser beam that is shining at the sensor and changes the voltage, control system will close the solenoid valve and stop delivering gas. This process is illustrated in laser-data window on LabVIEW where red lines show laser data of sensor 1 and sensor 2, respectively. When the striker bar begins blocking the laser beam of sensor 1, a white line starts going down to a constant value, while the red line keeps the original value. The value of red line falls off as sharply as the white line, as the striker bar cuts off the laser beam of sensor 2.

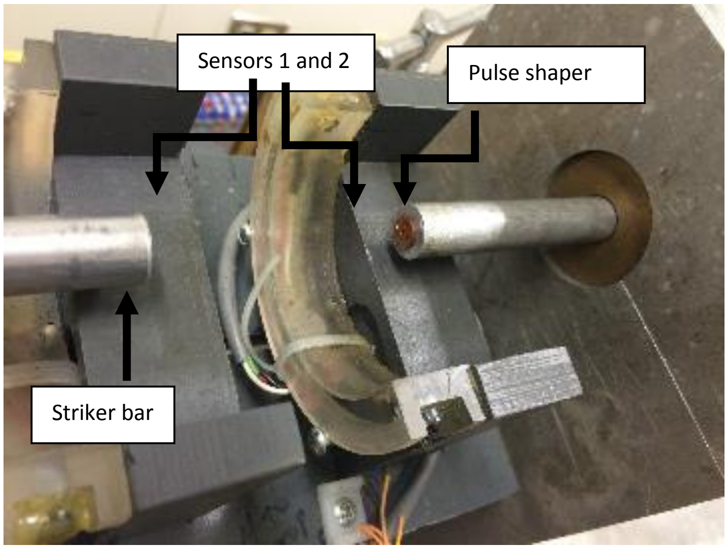

Fig 3.17: Sensors

3.2.4. Supporting and damping system

A reference plane of 415 mm long and 32 mm wide is designed for most of what the apparatus sits on except the tanks and pressure regulator as shown in Fig 3.17.

Each bar supporter (flange) shown in Fig 3.18, is fitted with a bronze busing machined to the proper tolerance; it allows the bar to slide freely in the axial direction and removes any bending waves due to the impact in order to satisfy the 1-D wave propagation conditions.

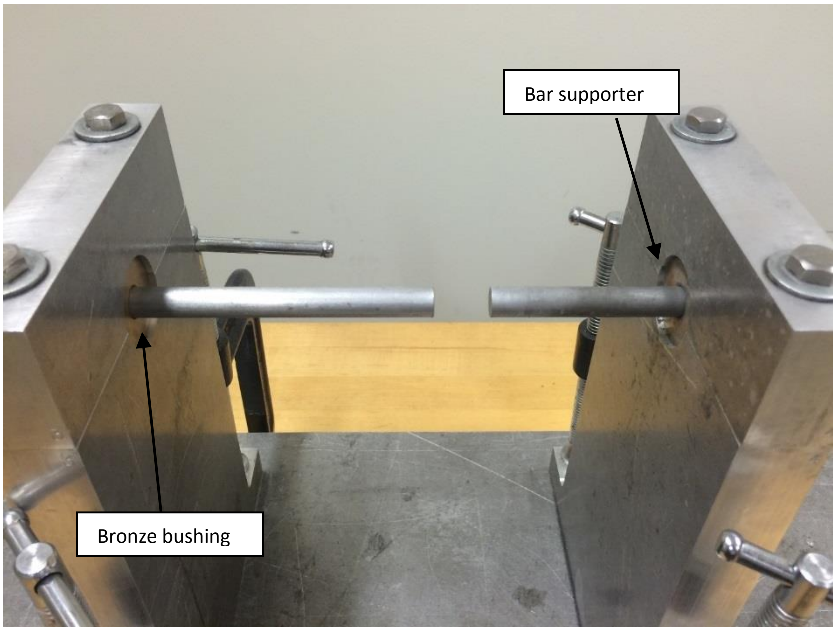

Fig 3.18: Bar supporters

Damping system, shown in Fig. 3.19, is designed to stop the transmitted bar after firing. The front end of damper is filled with lead for protecting the transmitted-bar end from ruining.

Fig 3.19: A damper

3.2.5. Manual operation and recommendations for use

Check incident and transmitted signals

- Open NI Measurement & Automation program on desktop
- Under Configuration Tab, expand My System; then expand Devices & Interfaces
- If you do not see Configuration Tab; click View; then check Configuration
- Expand NI-DAQmx Devices; then right click on NI PXI-6115, and choose Test Panels as shown in Fig. 3.20.

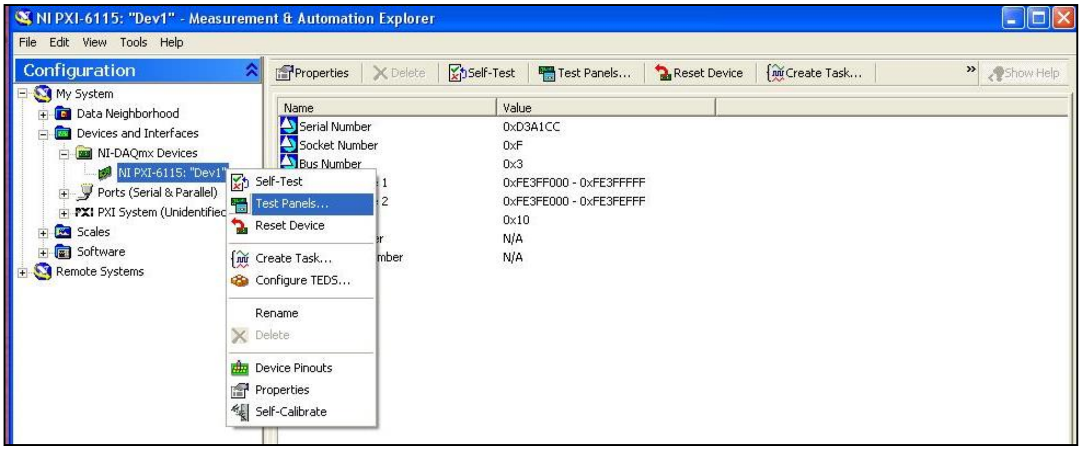

Name	Value
Serial Number	0xD3A1CC
Socket Number	0xF
Bus Number	0x3
1	0xFE3FF000 - 0xFE3FFFFF
2	0xFE3FE000 - 0xFE3FEFFF
	0x10
r	N/A
mber	N/A

Fig. 3.20: NI Measurement and Automation program

- Under Analog Input Tab, choose Channel Name: Dev1/a0 (to check incident signal), and channel Dev1/a1 (to check transmitted signal)
- Click start to see the signal of Dev1/a0, the window should be shown as in Fig 3.21 a. Uncheck "Auto-scale chart" as shown in Fig. 3.21 b.
- Push the bars manually to see if the signal changes as shown in Fig. 3.21 c; if it does, the equipment is good for doing experiment.

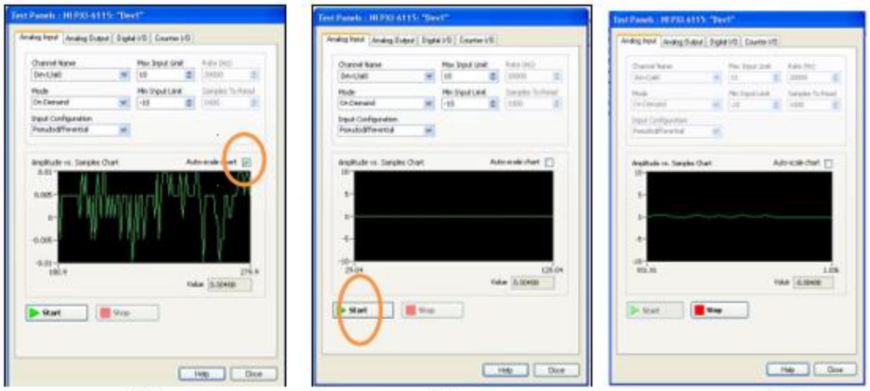

(a.) (b.) (c.)

Fig 3.21: Checking signal of Dev1/a0

- Do the same procedure to see the signal of Dev1/a1
- However, if after uncheck “Auto-scale chart” the window is shown as in Fig 3.21, the signal of Dev1/a0 must be fixed as the following steps:

+ Measure the resistance across the Quarter-bridge circuit and zero the resistance by rotating the small dial connected to it.

+ Zero the signal on the NI Measurement & Automation by using the coarse and fine offset dials on the amplifier (Amplifier B for channel a0_incident signal),

+ Increase the resistance across the Quarter-bridge circuit to 0.1 mV

+ Use the amplifier again to make sure the signal in NI Measurement & Automation is 0.1 V or -0.1V

+ Zero the resistance across the quarter-bridge circuit again.

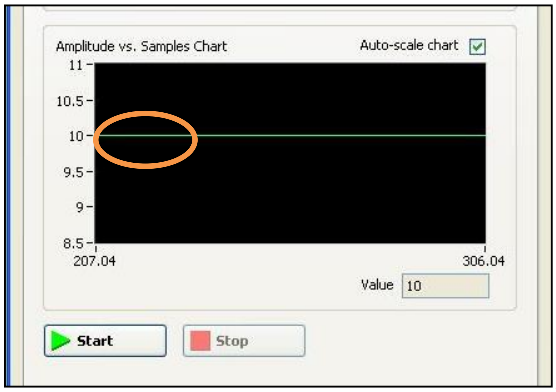

Auto-scale chart ☑

Value 10

Fig 3.22: Error in the Amplitude vs. Samples chart

- If signals shown as Fig 3.22 a, incident or transmitted signal may go beyond limit

+ Check the amplifiers to see if Over-Range light is on

+ Check the Quarter-bridge circuit to see if there is any loose connection

+ If the Over-Range light is still on, the wire is most likely broken.

- Push the bars manually to see if the signal changes; if it does, the equipment is good for doing experiment.
- Do the same procedure to see the signal of Dev1/a1

Open pressure tanks and adjust pressure

- Open the blue tank by turning the knob counter clockwise
- Open the black tank by turning the knob counter clockwise
- The pressure displayed on the small tank is the pressure used
- Turn the middle valve to the far left (counter clockwise) to decrease pressure (listen to the hissing sound)
- Turn the middle valve to the far right (clockwise) to increase pressure (listen to the hissing sound)

- Have the middle valve in the position at which no hissing sound is heard to have constant desired pressure.

Set up the experiment

- Close NI Measurement & Automation program
- Open LabVIEW 8.0 program on desktop
- Under Open Tab, choose C:\...Instruments\Drop\SplitbarMx_3_B.vi file as shown in Fig. 3.23. Testing constants should be double-checked.

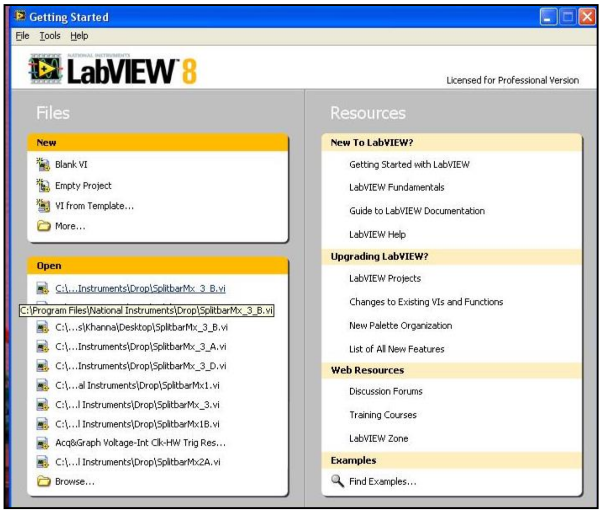

Fig. 3.23: LabVIEW 8.0 program

- Push the strike bar inside and at the end of the barrel
- Put the shaper on the front of the incident bar by using some grease.
- Adjust the incident such that it does not block either sensors as shown in Fig 3.24
- Put the specimen on between the incident and transmitted bars with a little oil on both sides of specimen (Fig. 3.24)

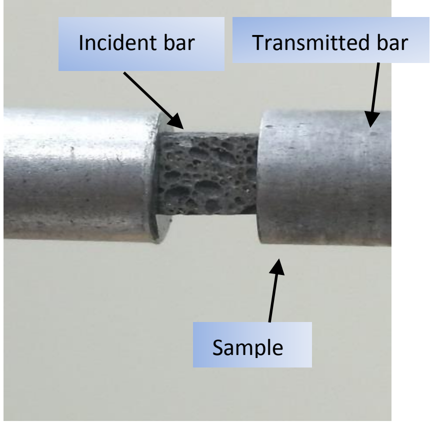

Fig 3.24: Specimen sandwiched between incident and transmitted bars

- Cover the specimen area like a small chamber, so that after experiment specimen would not fly far away.
- Make sure the damper is in the right place behind the transmitted bar. The distance from transmitted bar end to the in-front surface of damper (Fig. 3.25 a) is approximately equal to the distance between the pulse shaper and bronze busing (Fig. 3.25 b), enabling shot incident bar to keep right position in bronze bushing.

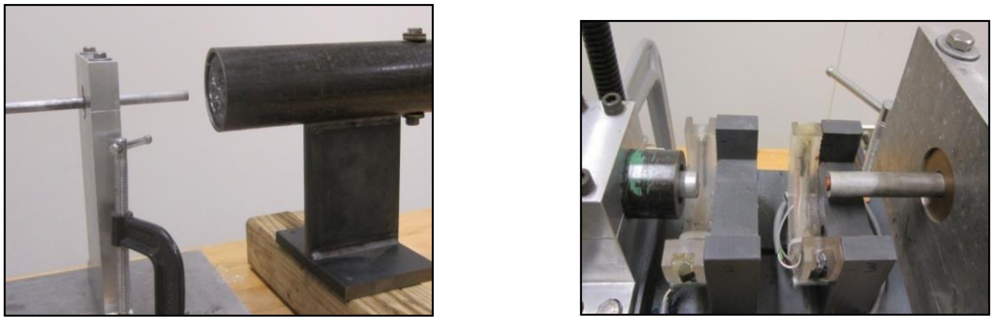

(a) (b)

Fig. 3.25: Distance from the end of transmitted bar to the damper

- Make sure the constants are in LabVIEW program are correct
- Click the Run button on NI LabVIEW 8.0 (⇨)
- Choose folder to store the data and data file name

- Click Fire. The time between clicking "Run" and "Fire" is within 20 seconds.

- If the signal appears on the screen, the test is good.

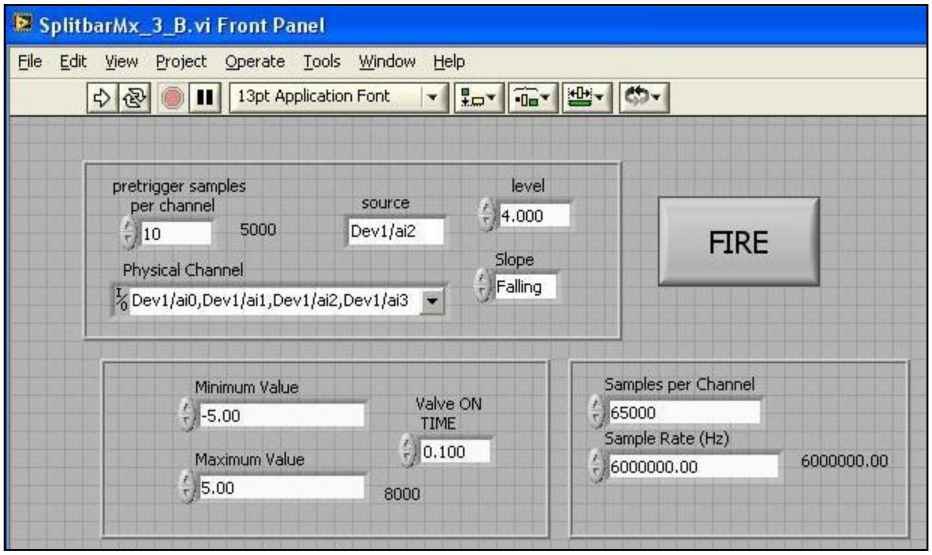

pretrigger samples per channel: 10 5000
source: Dev1/ai2
level: 4.000
Physical Channel: Dev1/ai0,Dev1/ai1,Dev1/ai2,Dev1/ai3
Slope: Falling
Minimum Value: -5.00
Maximum Value: 5.00 8000
Valve ON TIME: 0.100
Samples per Channel: 65000
Sample Rate (Hz): 6000000.00 6000000.00

Fig 3.26: Testing constants used in LabVIEW

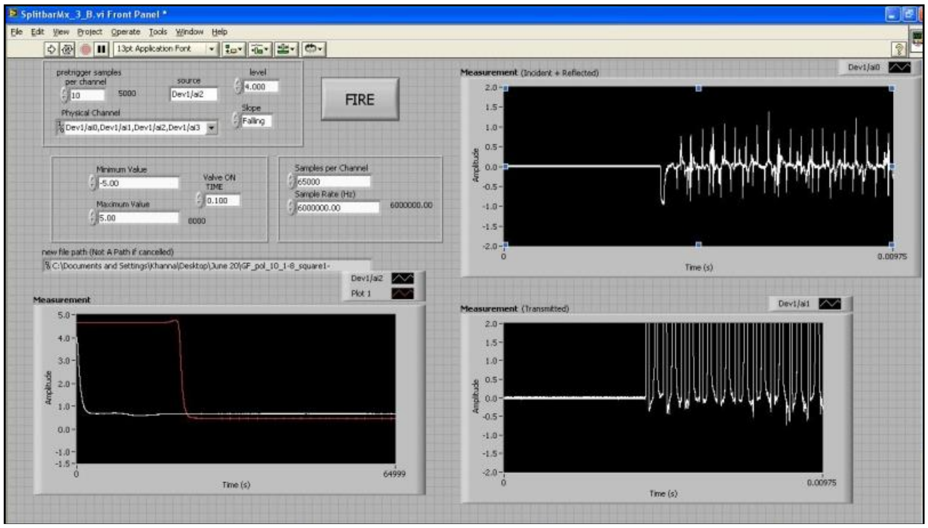

pretrigger samples per channel: 10 5000
source: Dev1/ai2
level: 4.000
Physical Channel: Dev1/ai0,Dev1/ai1,Dev1/ai2,Dev1/ai3
Slope: Falling
Minimum Value: -5.00
Maximum Value: 5.00 8000
Valve ON TIME: 0.100
Samples per Channel: 65000
Sample Rate (Hz): 6000000.00 6000000.00
new file path (Not A Path if cancelled): C:\Documents and Settings\Khanna\Desktop\June 20\GF_pol_10_1-8_square1-

(a)

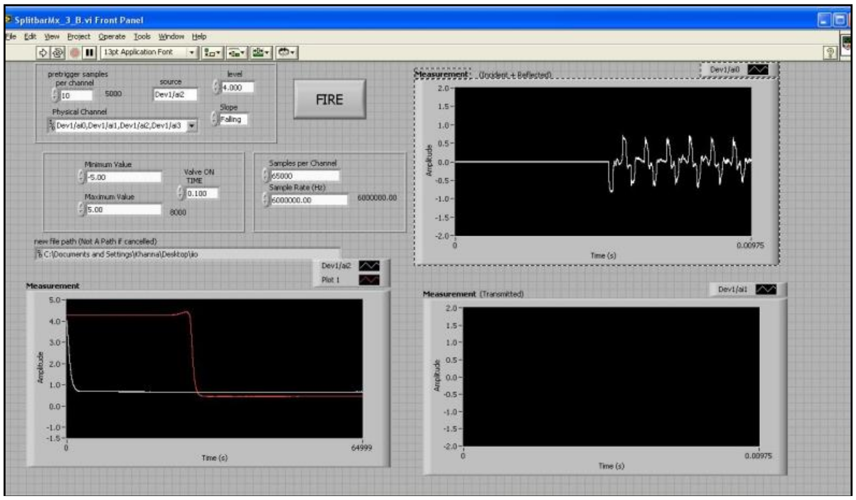

pretrigger samples per channel: 10 5000
source: Dev1/ai2
level: 4.000
Slope: Falling
Physical Channel: Dev1/ai0,Dev1/ai1,Dev1/ai2,Dev1/ai3
Minimum Value: -5.00
Maximum Value: 5.00 8000
Valve ON TIME: 0.100
Samples per Channel: 65000
Sample Rate (Hz): 6000000.00 6000000.00
new file path (Not A Path if cancelled): C:\Documents and Settings\Khanna\Desktop\io

(b)

Fig. 3.27: Examples of operating errors presented on LabVIEW

3.3. Specimen Preparation

3.3.1. Process of preparation of Graphene aluminum composite foam

The Graphene Al foam was fabricated at AMPRI India and the specimens made at University of Missouri, Columbia. In last several years, many technologies had been established for the production of metallic foams, but it has been specified that only some of these process will be appropriate for the manufacture of metal foams in an engineering scale. These technologies can be divided into two categories:

a. Liquid metal (melt route process)
b. Metal powder (Powder Metallurgy methods)

In current literature, common ways of making GR reinforced aluminum foam is by liquid metal (melt route process). Maximum commercially accessible metal foams are based on alloy containing: aluminum, nickel, and magnesium, and lead, titanium, steel, copper, and even gold. Among the metal foams, Al alloy is designated for commercially the most exploited ones because of their low density.

Methodology

The preparation of aluminum foam will be completed in three phases:

Phase 1: Laboratory scale synthesis of Al foam:

(a.) Electrical Resistance Furnace: Laboratory scale process development for making Al foam. For this first instance, we need an electrical resistance furnace having a capacity to melt at least 5-6 kg of Al alloy. The furnace will be closed on all the sides and open at top. The electrical resistance furnace would be interfaced with a thermocouple to measure melt temperature and recorder to read the temperature. It is interfaced with also a temperature controller to control the temperature. The maximum temperature of the furnace should be around 1000 degree Celsius.

(b.) A mechanical stirrer: A mechanical stirrer is to be fabricated with mild steel coated with graphite. The stirrer is required to fix in a motor to rotate the stirrer at least a speed of 700-800 RPM.

(c.) Cast iron die: A cast iron split die, cylindrical in shape, is to be made. The size of the die will be depending on the dimensions of the furnace.

(d.) Air compressor: An air compressor will be used to cool the hot foam in the mold.

Phase 2: Raw materials required for making foam:

(a.) Aluminum alloy reinforce with SiC and Graphene: An Al alloy will be selected (AA5083) as the matrix alloy and SiC particle of 10 wt.% (size: 20-40 micron) will be used as reinforced phase. Graphene (wt.0.5%) are used as thickening agent.

(b.) Foaming agent: TiH_2 (titanium hydride) 1 wt.% of metal used, will be used as foaming agent.

Activities carried out

Step 1. Step for making foam

(a.) First of all, we should coat the cast iron mold with graphite paste and dry the mold. Fix the split die with the help of nut-bolt. There should not be any gap between the two parts, otherwise liquid metal will leak through the gap. For precautionary measure the joint portion should be filled with graphite paste.

(b.) Place the mold in the furnace.

(c.) Put raw material al alloy in the mold

(d.) Switch on the furnace and heat up to temperature of 750 degrees Celsius. Once the Al alloy is melted then place the stirrer in to the mold. The stirrer blade should be dipped in the liquid metal.

(e.) Start the motor and raise the stirrer speed up to 700 RPM.

(f.) Then add SiC and Graphene in the melt and mix the particles nicely in liquid Al alloy melt.

(g.) Once the particle is mixed in Al alloy melt, foaming agent 1Wt% should be added in the melt. The foaming agent should be wrapped in Al foil. The total foaming agent should be divided into 10 parts and then wrapped in Al foil; there will be 10 balls of foaming agent wrapped with Al foil.

(h.) After adding foaming agent stir for 1 minute and then take out immediately the stirrer from the melt.

(i.) Once the foaming is over. Take out the mold with foam and cool the mold with compressed air. Finally, the mold with foam is to be left over for around 24 hours. Next day one can open the die out the Al foam.

3.3.2. Specimen dimension

Al alloy foam sample is prepared by melt route using a patented process of AMPRI India. The foam samples are cut conforming to the size of the mild steel sections (round and square). The foam samples of 21mm x 21mm x 30mm have been cut from the cast foam blocks. The samples were cut using diamond cutter at very slow speed (in University of Missouri, Columbia) so that the surface of cell structure does not get distorted. The size of the foam sample was cut in dimension of 7.5mm*7.5mm*7.5mm (Fig. 3.28). The sample was polished by sandpaper and grinding wheel so that all sample is very finished and very accurately in measurement and test for quasi-static compressive behaviour and high strain rate test using Universal Testing Machine (ADMET) and Split Hopkinson Pressure Bar (SHPB) respectively.

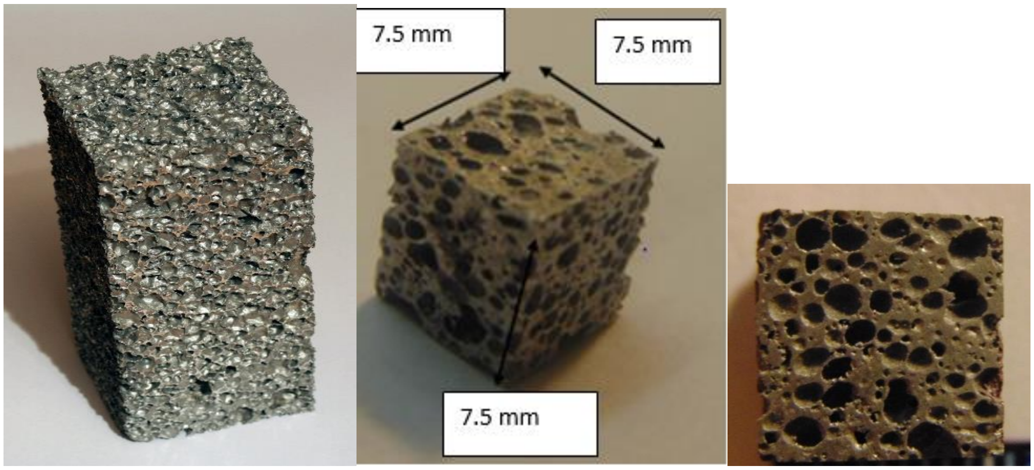

(a) **(b)** **(c)**

Fig. 3.28.Graphene - SiC hybrid Al foam sample (a) Cast block, (b) polished sample before test and (c) polished sample showing one of the faces of the foam block

Density Measurement

The density of AA5083 alloy (Al-5.5% Mg-0.3%Mn)-10wt% SiC and 0.5wt%Graphene composite foam is found out by mass and volume measurements. Samples of dimensions 7.5 mm x 7.5 mm x 7.5 mm are used for density measurements. The relative density of AA5083 alloy 10 wt % SiC ,Graphene (wt.0.5%) composite foam is calculated by dividing density of foam by density of solid Al (2.8 gm/cc) .Around 37 samples were cut in the dimension prepared from different places as received from casting. The average relative density is found around 0.23- 0.29 gm/cc and the porosity is 75.6%.

3.4. Pulse shaper Design

3.4.1. Pulse-shaper dimension and shape

Fundamental equations of SHPB theory are derived from one-dimensional stress wave theory in which uniaxial stress equilibrium is assumed within the specimen. Therefore, SHPB experiment results are valid and reliable if and only if the specimen deforms at a constant strain rate and uniaxial stress equilibrium is achieved in specimen.

Taylor-von Karman theory gives the relation of specimen pulse duration t and (specimens length) H_S as follow:

$$t^2 = \frac{\pi^2 \rho_S H_S^2}{\frac{\partial \sigma}{\partial \varepsilon}} \qquad (32)$$

where t is pulse duration required for a uniform uniaxial stress state to be achieved in specimen, ρ_s is the specimen density, and $\partial\sigma/\partial\varepsilon$ is the rate of true stress/ true strain curve for the material to be tested (81). For the high-work-hardening-rate and low-sound-speed materials like Graphene aluminum foam composites, in order to increase the pulse duration, a shorter length specimen is required to facilitate rapid ring-up followed by rapid attainment of uniaxial stress state in specimen.

However, as discussed, the reduction of H_S affects the aspect ratio. It can be seen that choosing (diameter) D_S is based on the SHPB condition (bar diameter) and aspect ratio chosen to ensure minimizing the inertia and friction effects, so in most of cases length reduction is impossible. That is why pulse-shaper technique becomes popular in a modified SHPB with plenty of advantages such as achieving constant strain rate, smoothing the stress pulses, eliminating the high frequency oscillations in incident pulse, and extending the pulse duration to facilitate tress equilibrium. Pulse-shaper is generally an elastic-plastic metal disk (tip material) attached to one end of incident bar by a little bit of grease. When testing, the striker bar's impact on the pulse shaper transfers energy indirectly to the incident bar, causing the pulse duration to increase as expected. Pulse shaper thickness 1.59 mm and thickness-to-diameter ratio $T_P/D_P = 0.25$ inches. This research used a pulse-shaper with $D_P = 6.35$ mm., $T_P = 1.59$ mm.

Fig. 3.29. Pulse shaper design with holes**

3.4.2. Pulse-shaper material

Even though some researchers believe that pulse shaper material should be the same as specimen material, i.e., playing the role of a dummy specimen to shape incident pulses as wanted, Vecchio and Jiang [82] stated that pulse-shaper material does not have to possess similar strength as that of specimen nor does it have to be made of the same material as the test specimen

** ***Personal Communication with Abdelhakim Aldoshan, Ph.D. candidate, University of Missouri, Columbia***

For polymer or composites with polymer matrix, soft materials such as brass, Plexiglas, hard or annealed copper, and low-strength stainless steel are recommended as pulse-shaper materials. Among these materials, copper is the most popular because a copper shaper can easily deform plastically to a relative large strain without fracture. Pulse shaper material chosen for this work is C14500 Tellurium copper with basic physical and mechanical properties shown in Table 3.3.

Table 3.3: Physical and mechanical properties of Copper No. C14500

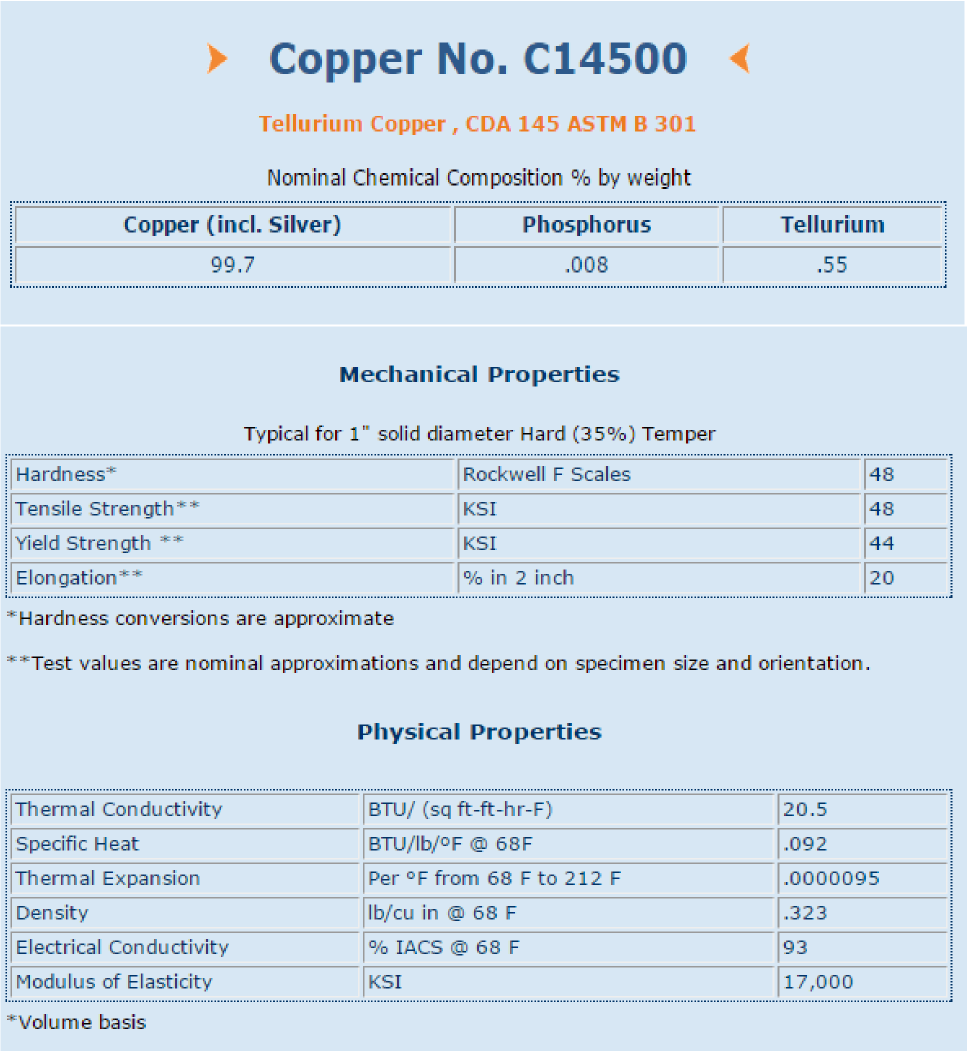

Copper No. C14500

Tellurium Copper , CDA 145 ASTM B 301

Nominal Chemical Composition % by weight

Copper (incl. Silver)	Phosphorus	Tellurium
99.7	.008	.55

Mechanical Properties

Typical for 1" solid diameter Hard (35%) Temper

Hardness*	Rockwell F Scales	48
Tensile Strength**	KSI	48
Yield Strength **	KSI	44
Elongation**	% in 2 inch	20

*Hardness conversions are approximate

**Test values are nominal approximations and depend on specimen size and orientation.

Physical Properties

Thermal Conductivity	BTU/ (sq ft-ft-hr-F)	20.5
Specific Heat	BTU/lb/°F @ 68F	.092
Thermal Expansion	Per °F from 68 F to 212 F	.0000095
Density	lb/cu in @ 68 F	.323
Electrical Conductivity	% IACS @ 68 F	93
Modulus of Elasticity	KSI	17,000

*Volume basis

Reference: http://copper-casting-alloys.brass-copper- fittings.com/c14500_tellurium_copper.htm

In literature, some trial tests was conducted to determine which types of material become effective pulse-shapers for this research.C14500-copper pulse shaper and annealed C14500-copper pulse shaper is employed. Obviously, C14500-copper pulse shaper results were constant in reflected pulse, while the others gave either complicated pulses or varying ones. It is well known that the test with constant reflected pulse leading to unvarying stain rate in specimen. In addition, pulse shaper with low work-hardening property obstructs the tests performed at high strain rate. The pulse shaper shrinks while testing for Graphene foam specimen at strain rate of 2700 s^{-1} or higher.

3.5 Data Analysis

3.5.1. Data Analysis with MS-Excel

The purpose of SHPB data in Excel is to select needed data for running SHPB MATLAB file. Then, from that input, running SHPB MATLAB file will give output of incident, transmitted, reflected pulses, and material-behavior relations including strain rate time, stress time, stress-strain, and views of stress equilibrium check.

An Excel data file of SHPB experiment presented in Fig. 3.30. Appearing on screen (Fig. 3.30) are columns A and B referring to data collected from incident and transmitted strain gages, respectively. Two rows from top as marked in Fig. 3.30 was deleted in order to draw plots of incident and transmitted pulses, while two columns of ascending order and time were added as shown in Fig. 3.30.

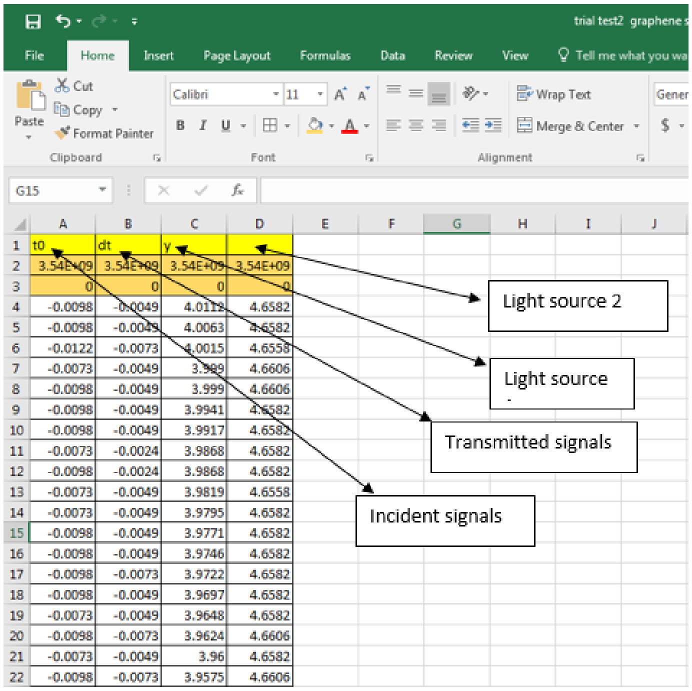

	A	B	C	D
1	t0	dt	y	
2	3.54E+09	3.54E+09	3.54E+09	3.54E+09
3	0	0	0	0
4	-0.0098	-0.0049	4.0112	4.6582
5	-0.0098	-0.0049	4.0063	4.6582
6	-0.0122	-0.0073	4.0015	4.6558
7	-0.0073	-0.0049	3.999	4.6606
8	-0.0098	-0.0049	3.999	4.6606
9	-0.0098	-0.0049	3.9941	4.6582
10	-0.0098	-0.0049	3.9917	4.6582
11	-0.0073	-0.0024	3.9868	4.6582
12	-0.0098	-0.0024	3.9868	4.6582
13	-0.0073	-0.0049	3.9819	4.6558
14	-0.0073	-0.0049	3.9795	4.6582
15	-0.0098	-0.0049	3.9771	4.6582
16	-0.0098	-0.0049	3.9746	4.6582
17	-0.0098	-0.0073	3.9722	4.6582
18	-0.0098	-0.0049	3.9697	4.6582
19	-0.0073	-0.0049	3.9648	4.6582
20	-0.0098	-0.0073	3.9624	4.6606
21	-0.0073	-0.0049	3.96	4.6582
22	-0.0098	-0.0073	3.9575	4.6606

Light source 2

Light source

Transmitted signals

Incident signals

Fig. 3.30. (a.) SHPB data before modifying

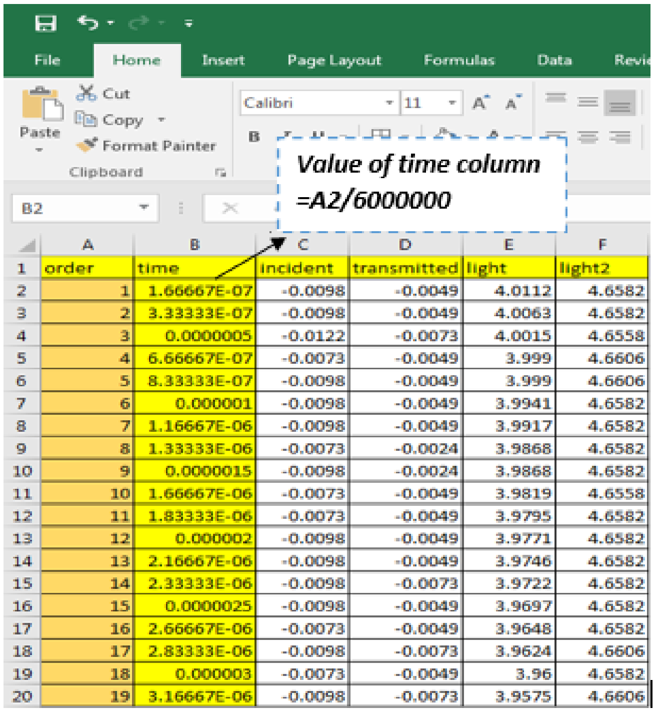

Value of time column

=A2/6000000

	A	B	C	D	E	F
1	order	time	incident	transmitted	light	light2
2	1	1.66667E-07	-0.0098	-0.0049	4.0112	4.6582
3	2	3.33333E-07	-0.0098	-0.0049	4.0063	4.6582
4	3	0.0000005	-0.0122	-0.0073	4.0015	4.6558
5	4	6.66667E-07	-0.0073	-0.0049	3.999	4.6606
6	5	8.33333E-07	-0.0098	-0.0049	3.999	4.6606
7	6	0.000001	-0.0098	-0.0049	3.9941	4.6582
8	7	1.16667E-06	-0.0098	-0.0049	3.9917	4.6582
9	8	1.33333E-06	-0.0073	-0.0024	3.9868	4.6582
10	9	0.0000015	-0.0098	-0.0024	3.9868	4.6582
11	10	1.66667E-06	-0.0073	-0.0049	3.9819	4.6558
12	11	1.83333E-06	-0.0073	-0.0049	3.9795	4.6582
13	12	0.000002	-0.0098	-0.0049	3.9771	4.6582
14	13	2.16667E-06	-0.0098	-0.0049	3.9746	4.6582
15	14	2.33333E-06	-0.0098	-0.0073	3.9722	4.6582
16	15	0.0000025	-0.0098	-0.0049	3.9697	4.6582
17	16	2.66667E-06	-0.0073	-0.0049	3.9648	4.6582
18	17	2.83333E-06	-0.0098	-0.0073	3.9624	4.6606
19	18	0.000003	-0.0073	-0.0049	3.96	4.6582
20	19	3.16667E-06	-0.0098	-0.0073	3.9575	4.6606

Fig. 3.30. a^{1}. SHPB data before modifying

After plotting the full incident and transmitted signals on separate graphs shown in Fig. 3.31.b, since the first set of pulses used, we zoomed in both incident and transmitted graphs, and then selected the first set as shown in Fig. 3.31 b. To select the needed incident data, one should notice the time value on x-axis at the beginning (region A in Fig. 3.31 c) and end values of incident pulse. Starting point is the one close to the intersection of the pulse and the X axis, we can easily find the actual time starting point of incident bar in column B (time column) corresponding to the incident value, because from incident data of the continued incident values keep negative. From time value shown in Fig. 3.31 d, incident data starts to get value zero, and then keeps going to positive values. In addition, from region B as shown in Fig. 3.31 d, therefore, it concluded that the incident data belonging to the actual time value from 0.004966 to 0.00529 corresponds to incident pulse.

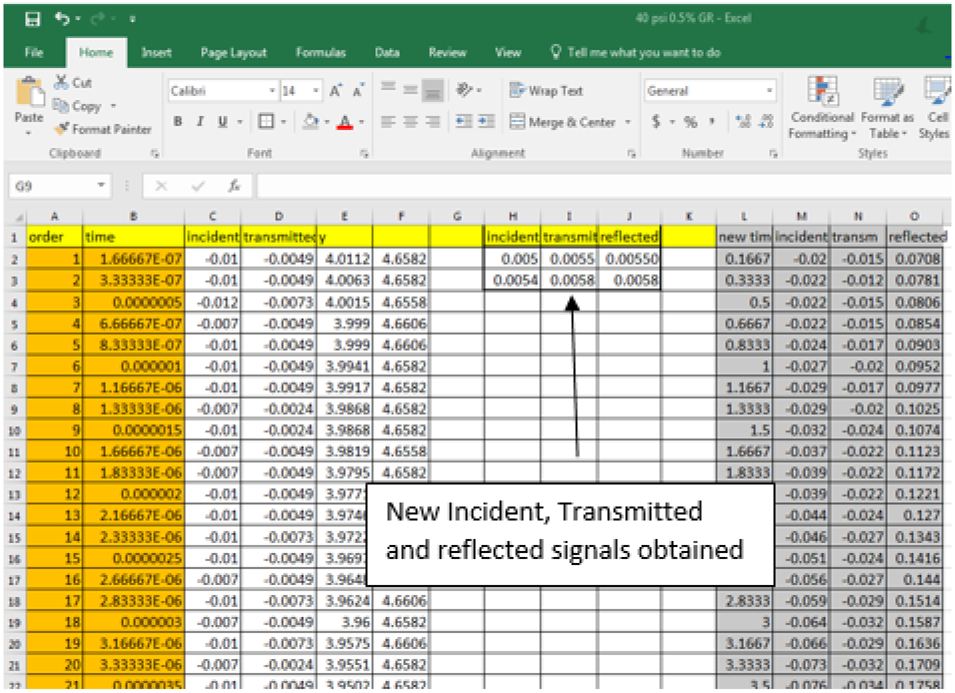

	A	B	C	D	E	F	G	H	I	J	K	L	M	N	O
1	order	time	incident	transmitte	y			incident	transmit	reflected		new tim	incident	transm	reflected
2	1	1.66667E-07	-0.01	-0.0049	4.0112	4.6582		0.005	0.0055	0.00550		0.1667	-0.02	-0.015	0.0708
3	2	3.33333E-07	-0.01	-0.0049	4.0063	4.6582		0.0054	0.0058	0.0058		0.3333	-0.022	-0.012	0.0781
4	3	0.0000005	-0.012	-0.0073	4.0015	4.6558						0.5	-0.022	-0.015	0.0806
5	4	6.66667E-07	-0.007	-0.0049	3.999	4.6606						0.6667	-0.022	-0.015	0.0854
6	5	8.33333E-07	-0.01	-0.0049	3.999	4.6606						0.8333	-0.024	-0.017	0.0903
7	6	0.000001	-0.01	-0.0049	3.9941	4.6582						1	-0.027	-0.02	0.0952
8	7	1.16667E-06	-0.01	-0.0049	3.9917	4.6582						1.1667	-0.029	-0.017	0.0977
9	8	1.33333E-06	-0.007	-0.0024	3.9868	4.6582						1.3333	-0.029	-0.02	0.1025
10	9	0.0000015	-0.01	-0.0024	3.9868	4.6582						1.5	-0.032	-0.024	0.1074
11	10	1.66667E-06	-0.007	-0.0049	3.9819	4.6558						1.6667	-0.037	-0.022	0.1123
12	11	1.83333E-06	-0.007	-0.0049	3.9795	4.6582						1.8333	-0.039	-0.022	0.1172
13	12	0.000002	-0.01	-0.0049	3.977								-0.039	-0.022	0.1221
14	13	2.16667E-06	-0.01	-0.0049	3.974								-0.044	-0.024	0.127
15	14	2.33333E-06	-0.01	-0.0073	3.972								-0.046	-0.027	0.1343
16	15	0.0000025	-0.01	-0.0049	3.969								-0.051	-0.024	0.1416
17	16	2.66667E-06	-0.007	-0.0049	3.964								-0.056	-0.027	0.144
18	17	2.83333E-06	-0.01	-0.0073	3.9624	4.6606						2.8333	-0.059	-0.029	0.1514
19	18	0.000003	-0.007	-0.0049	3.96	4.6582						3	-0.064	-0.032	0.1587
20	19	3.16667E-06	-0.01	-0.0073	3.9575	4.6606						3.1667	-0.066	-0.029	0.1636
21	20	3.33333E-06	-0.007	-0.0024	3.9551	4.6582						3.3333	-0.073	-0.032	0.1709
22	21	0.0000035	-0.01	-0.0049	3.9502	4.6582						3.5	-0.076	-0.034	0.1758

New Incident, Transmitted and reflected signals obtained

Fig. 3.31 a. New Incident, Transmitted, reflected originate from the signals

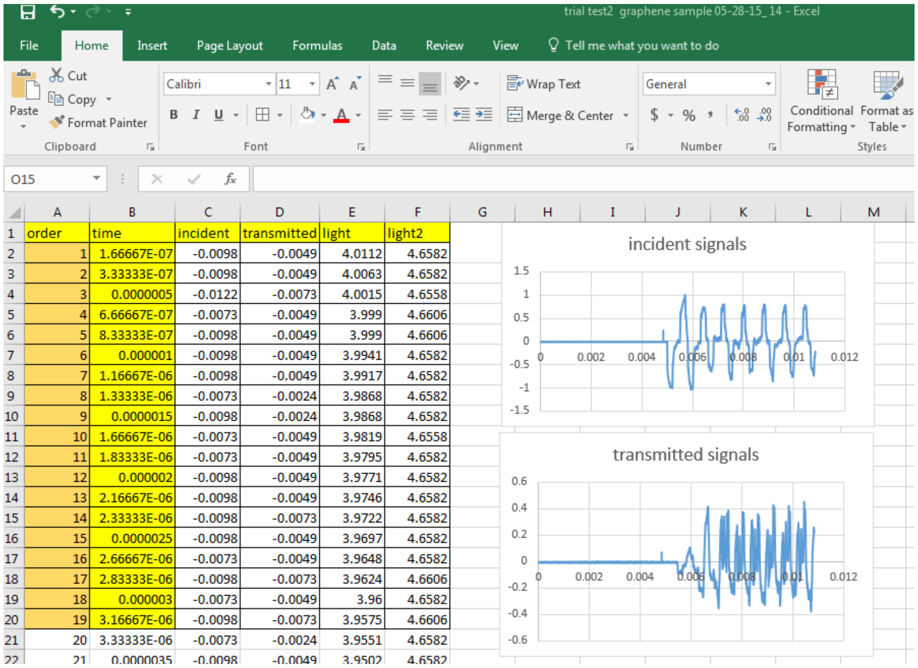

	A	B	C	D	E	F
1	order	time	incident	transmitted	light	light2
2	1	1.66667E-07	-0.0098	-0.0049	4.0112	4.6582
3	2	3.33333E-07	-0.0098	-0.0049	4.0063	4.6582
4	3	0.0000005	-0.0122	-0.0073	4.0015	4.6558
5	4	6.66667E-07	-0.0073	-0.0049	3.999	4.6606
6	5	8.33333E-07	-0.0098	-0.0049	3.999	4.6606
7	6	0.000001	-0.0098	-0.0049	3.9941	4.6582
8	7	1.16667E-06	-0.0098	-0.0049	3.9917	4.6582
9	8	1.33333E-06	-0.0073	-0.0024	3.9868	4.6582
10	9	0.0000015	-0.0098	-0.0024	3.9868	4.6582
11	10	1.66667E-06	-0.0073	-0.0049	3.9819	4.6558
12	11	1.83333E-06	-0.0073	-0.0049	3.9795	4.6582
13	12	0.000002	-0.0098	-0.0049	3.9771	4.6582
14	13	2.16667E-06	-0.0098	-0.0049	3.9746	4.6582
15	14	2.33333E-06	-0.0098	-0.0073	3.9722	4.6582
16	15	0.0000025	-0.0098	-0.0049	3.9697	4.6582
17	16	2.66667E-06	-0.0073	-0.0049	3.9648	4.6582
18	17	2.83333E-06	-0.0098	-0.0073	3.9624	4.6606
19	18	0.000003	-0.0073	-0.0049	3.96	4.6582
20	19	3.16667E-06	-0.0098	-0.0073	3.9575	4.6606
21	20	3.33333E-06	-0.0073	-0.0024	3.9551	4.6582
22	21	0.0000035	-0.0098	-0.0049	3.9502	4.6582

Fig 3.31 b. plotted incident signals and transmitted signals from BC and BD

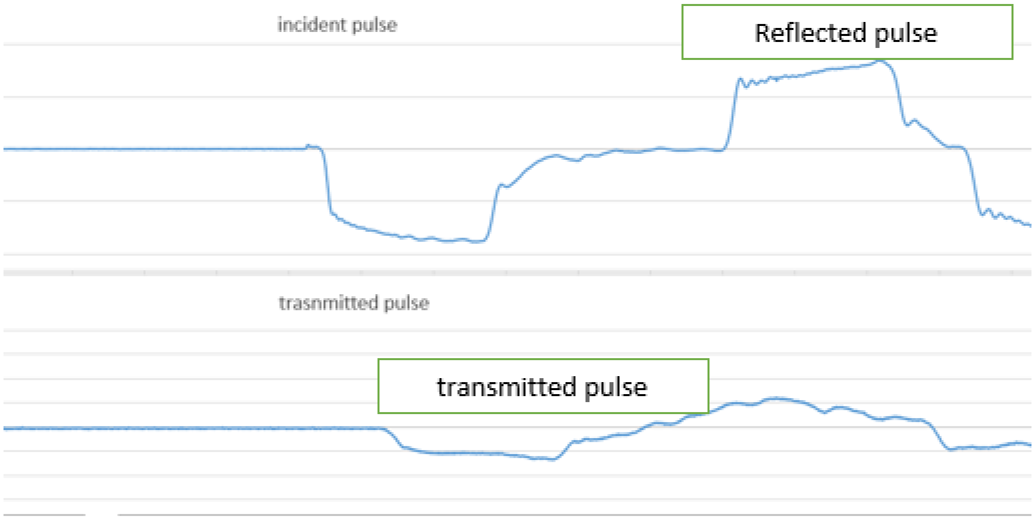

Fig 3.31 c. New incident, transmitted, reflected signals obtained from the original signals

Once the new incident, transmitted and reflected pulse are generated with the above signals, we need to find those values in the original signals and generate another new signals of incident, transmitted and reflected.

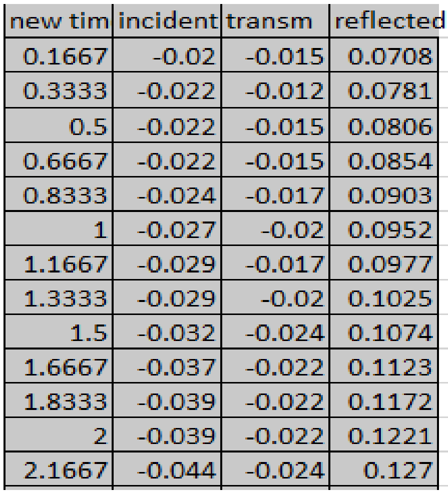

new tim	incident	transm	reflected
0.1667	-0.02	-0.015	0.0708
0.3333	-0.022	-0.012	0.0781
0.5	-0.022	-0.015	0.0806
0.6667	-0.022	-0.015	0.0854
0.8333	-0.024	-0.017	0.0903
1	-0.027	-0.02	0.0952
1.1667	-0.029	-0.017	0.0977
1.3333	-0.029	-0.02	0.1025
1.5	-0.032	-0.024	0.1074
1.6667	-0.037	-0.022	0.1123
1.8333	-0.039	-0.022	0.1172
2	-0.039	-0.022	0.1221
2.1667	-0.044	-0.024	0.127

Fig. 3.31 d. New signals generated from 3.31

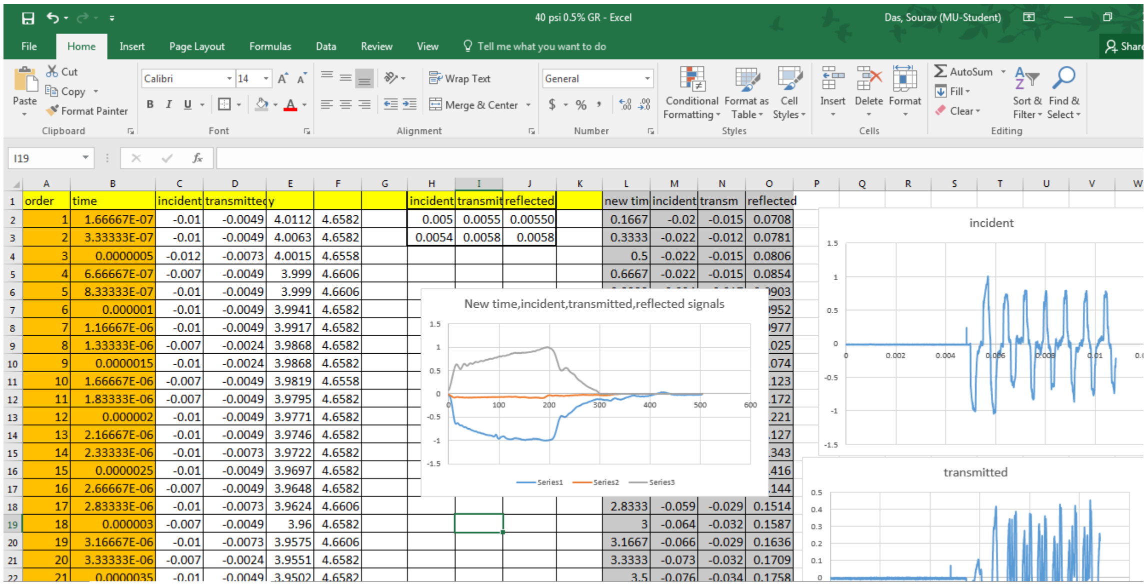

	A	B	C	D	E	F	G	H	I	J	K	L	M	N	O
1	order	time	incident	transmitted	y			incident	transmit	reflected		new tim	incident	transm	reflected
2	1	1.66667E-07	-0.01	-0.0049	4.0112	4.6582		0.005	0.0055	0.00550		0.1667	-0.02	-0.015	0.0708
3	2	3.33333E-07	-0.01	-0.0049	4.0063	4.6582		0.0054	0.0058	0.0058		0.3333	-0.022	-0.012	0.0781
4	3	0.0000005	-0.012	-0.0073	4.0015	4.6558						0.5	-0.022	-0.015	0.0806
5	4	6.66667E-07	-0.007	-0.0049	3.999	4.6606						0.6667	-0.022	-0.015	0.0854
6	5	8.33333E-07	-0.01	-0.0049	3.999	4.6606									903
7	6	0.000001	-0.01	-0.0049	3.9941	4.6582									952
8	7	1.16667E-06	-0.01	-0.0049	3.9917	4.6582									977
9	8	1.33333E-06	-0.007	-0.0024	3.9868	4.6582									.025
10	9	0.0000015	-0.01	-0.0024	3.9868	4.6582									.074
11	10	1.66667E-06	-0.007	-0.0049	3.9819	4.6558									.123
12	11	1.83333E-06	-0.007	-0.0049	3.9795	4.6582									.172
13	12	0.000002	-0.01	-0.0049	3.9771	4.6582									.221
14	13	2.16667E-06	-0.01	-0.0049	3.9746	4.6582									.127
15	14	2.33333E-06	-0.01	-0.0073	3.9722	4.6582									.343
16	15	0.0000025	-0.01	-0.0049	3.9697	4.6582									.416
17	16	2.66667E-06	-0.007	-0.0049	3.9648	4.6582									.144
18	17	2.83333E-06	-0.01	-0.0073	3.9624	4.6606						2.8333	-0.059	-0.029	0.1514
19	18	0.000003	-0.007	-0.0049	3.96	4.6582						3	-0.064	-0.032	0.1587
20	19	3.16667E-06	-0.01	-0.0073	3.9575	4.6606						3.1667	-0.066	-0.029	0.1636
21	20	3.33333E-06	-0.007	-0.0024	3.9551	4.6582						3.3333	-0.073	-0.032	0.1709
22	21	0.0000035	-0.01	-0.0049	3.9502	4.6582						3.5	-0.076	-0.034	0.1758

Fig. 3.31 e. shows the new signals data selections

The same procedure performed for reflected and transmitted pulses with the note that while incident and transmitted data admit negative values, reflected ones select positive values. The selected data from incident, transmitted and reflected pulse put in the order as shown in Fig. 3.31 e. This order, which stated in SHPB MATLAB file, cannot be changed because these selected data will be inputs for the MATLAB file. A change on time values at column O shown in Fig. 3.41 e is due to the conversion from second (Fig. 3.30 b) to microsecond (Fig. 3.31 e), so the final graphs after running SHPB MATLAB file with be versus microsecond as shown in Fig. 3.31 e. All the selected data must end in the same row as shown in Fig. 3.31 e; in other words, they are in the form of a matrix. The last row of the matrix is the one right before the row on which any pulse data comes to zero (see Fig. 3.31e) or switches from negative values to positive ones with respect to incident and transmitted pulses. Conversely, reflected data stops selected when any change makes from positive values to negative ones.

3.5.2. Data Analysis using MATLAB

SHPB MATLAB file named “Current_Split_Hopkinson_Code.m” run in MATLAB program. One must follow the instructions in the command window and call stress and strain correction factors from calibration part, allowing the MATLAB program to give the final graphs as for each experiment as seen in Fig. 3.32. The experiment conducted with an 18-inch striker bar with a specimen of 0.5% Graphene aluminum foam composite wt.0.5 percentage GR at 25 psi corresponding to the impact velocity of 8.89 ms^{-1}. Pulse shaper used in this experiment is with five holes, Copper C14500 with the dimensions D_P = 0.25 in., H_P = 0.0625 in.

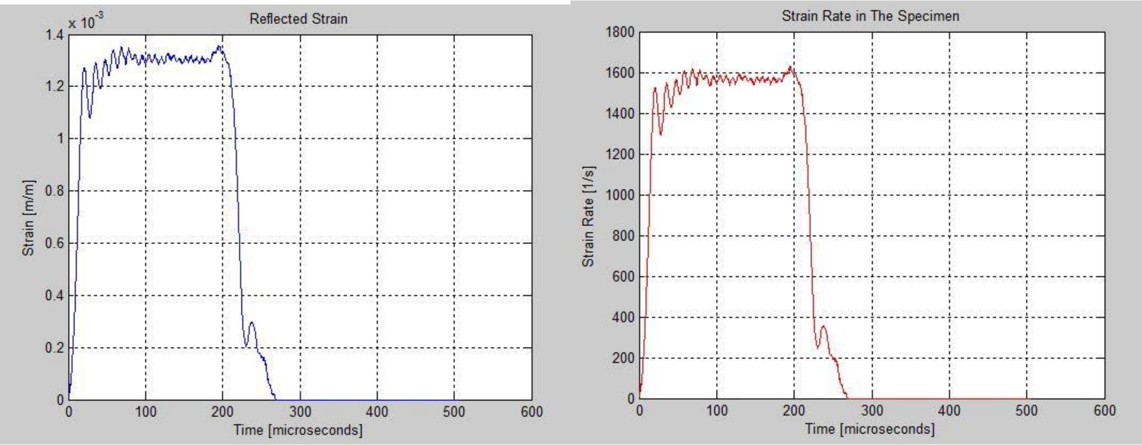

A. B.

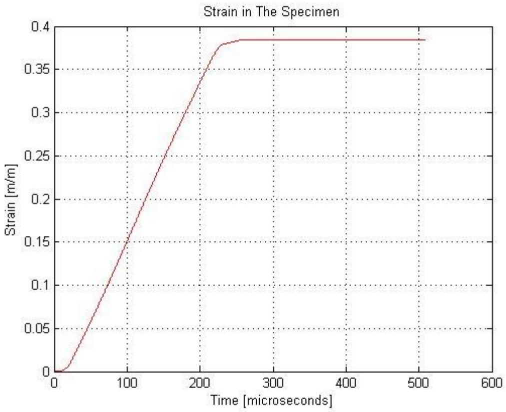
Strain in The Specimen
Strain [m/m]
Time [microseconds]
0.4
0.35
0.3
0.25
0.2
0.15
0.1
0.05
0
0
100
200
300
400
500
600

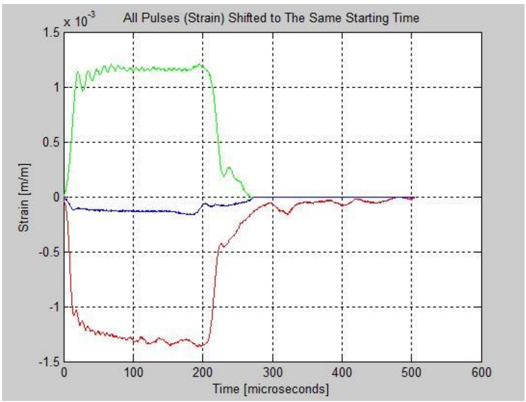
All Pulses (Strain) Shifted to The Same Starting Time
x 10^-3
Strain [m/m]
Time [microseconds]
1.5
1
0.5
0
-0.5
-1
-1.5
0
100
200
300
400
500
600

C.

D.

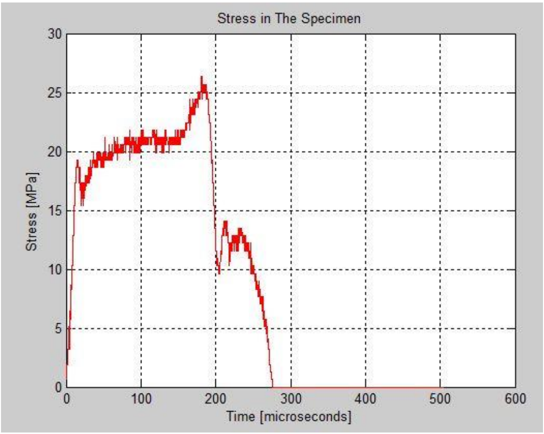
Stress in The Specimen
Stress [MPa]
Time [microseconds]
30
25
20
15
10
5
0
0
100
200
300
400
500
600

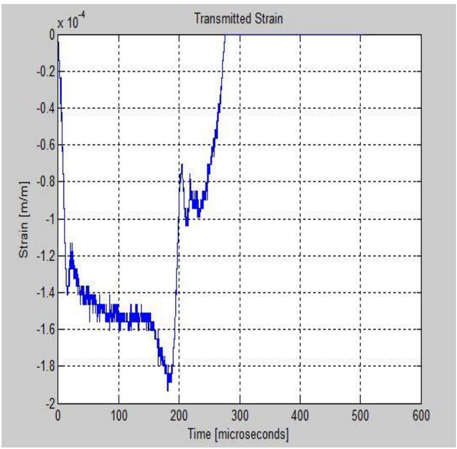
Transmitted Strain
x 10^-4
Strain [m/m]
Time [microseconds]
0
-0.2
-0.4
-0.6
-0.8
-1
-1.2
-1.4
-1.6
-1.8
-2
0
100
200
300
400
500
600

E.

F.

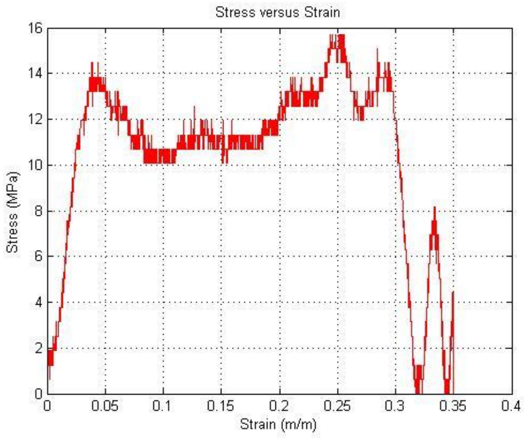
Stress versus Strain
Stress (MPa)
Strain (m/m)
16
14
12
10
8
6
4
2
0
0
0.05
0.1
0.15
0.2
0.25
0.3
0.35
0.4

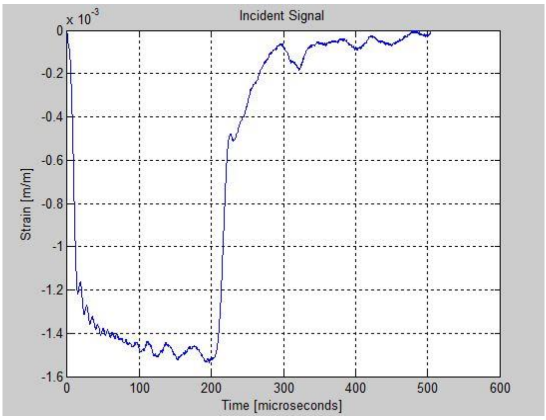
Incident Signal
x 10^-3
Strain [m/m]
Time [microseconds]
0
-0.2
-0.4
-0.6
-0.8
-1
-1.2
-1.4
-1.6
0
100
200
300
400
500
600

G. H.

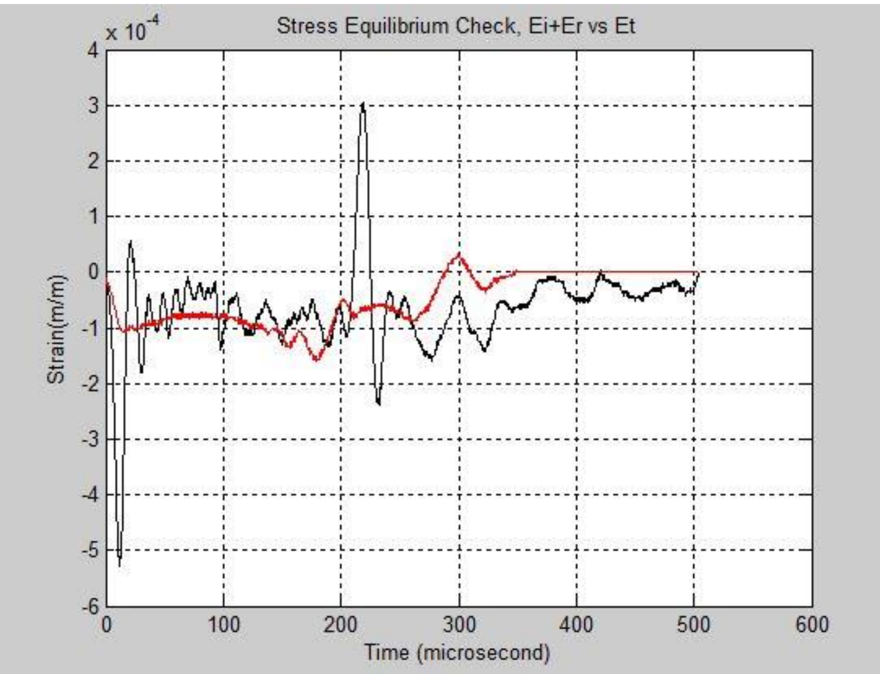

I.

Fig. 3.32. Final results of 0.5wt.% GR composite aluminum foam, given by the MATLAB program: (a) reflected pulse vs. time; (b) strain rate vs time; (c.) strain vs Time (d) 3 pulses shifted to the same starting time. (e.) stress vs time (f.) strain vs time. (g.) Stress vs strain (h.) Incident signals (i.) stress equilibrium checking.

Chapter 4
Results

4.1 Compressive strength

Al alloy based cellular material possesses application essentially in the areas of crashworthiness in which material should have a property to absorb mechanical energy. In order to know the crashworthiness of the material one should understand the compressive strength behaviour of the material at low and high strain rate. Figure 1 shows a theoretical stress-strain diagram of metallic cellular material. The stress-strain diagram shows three distinct regions; these are (i) initial linear elastic region (ii) flat plateau region and (iii) densification region. This kind of behaviour is observed in quasi static and in dynamic compression of metallic cellular material.

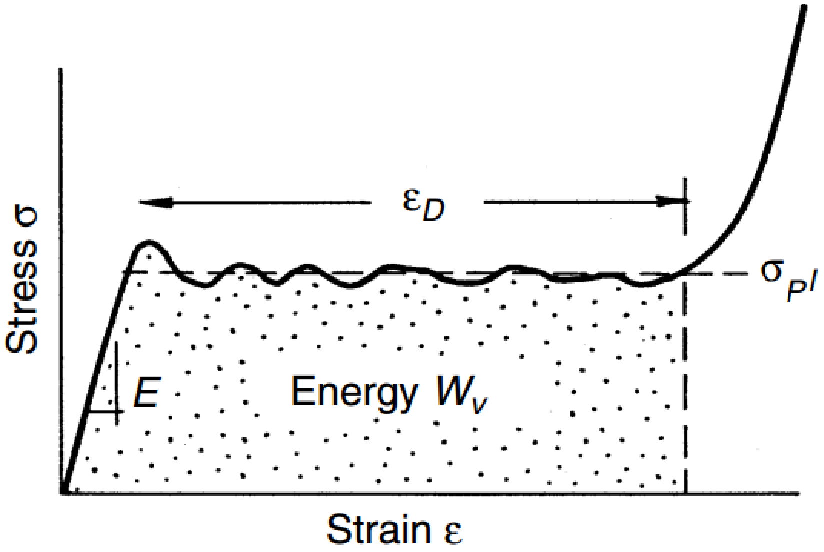

Fig 4.1 Typical Stress-strain curve for aluminum foam under compressive loading

(Reference : Metal foams: A Design guide by M.F Ashby)

In the last few years, there has been a considerable increase in interest in using metal cellular metallic material (metal foams) for lightweight structural components and energy absorption parts such as in the automobile, railway and aerospace industries, for that it should have a wide plateau in the compressive stress-strain curve. In these applications, the metal foam subjected to high-velocity (high strain rate) deformations. Designing for these applications therefore demands a full characterization of their mechanical properties under a wide range of strain rates. The quasi-static mechanical properties of aluminium alloy foams, such as compressive strength, and elastic modulus, have been extensively studied. However, under dynamic load conditions there has been relatively limited study due to the difficulty of characterizing the high strain rate behaviour of aluminium alloy foams. A servo hydraulic machine is common and convenient to study at lower strain rates (below $10s^{-1}$). A drop weight impact test can be used for different specimen geometries and allows easy variation of strain rate in the range $100s^{-1}$ – $500s^{-1}$. However, the system is very sensitive to the contact conditions between the impactor and specimen. Hence, in the present investigation static as well as dynamic compressive tests carried out using a servo hydraulic test machine and a Hopkinson pressure bar unit respectively. The static test carried out over a strain rate of $0.001s^{-1}$ to $1s^{-1}$ and the dynamic test was done over strain rates in the range of $500\ s^{-1}$ to $2700s^{-1}$. The results of low and high strain rates deformation behaviour described in the sections to follow:

4.2 Compressive tests of Al composite foam without Graphene at strain rates of $0.001s^{-1}$ to $1s^{-1}$ under quasi-static load

Static compressive tests were carried out using a servo hydraulic machine over strain rates of 0.001s^{-1}, to 1s^{-1}. The relative density of the samples was 0.21. Figure 4.2 shows a typical stress-strain diagram of Al alloy wt.15 % SiC composite foam over strain rates of

0.001s^{-1}, 0.01s^{-1}, 0.1s^{-1} and 1s^{-1}. The stress-strain diagram clearly shows initial linear elastic region with peak stress of 7.5 MPa, 8.0 MPa, 8.0 MPa and 6.5 MPa at strain rates of 0.001s^{-1}, 0.01s^{-1}, 0.1s^{-1} and 1s^{-1} respectively. The stress - strain diagram shows flat plateau region of plateau stress in the range of 8.00 MPa to 8.70 MPa. The densification strain is found to be around 0.28. The densification region may be seen after the strain value of 0.28. It is worth noticing that the plateau region stress increases with strain, which is mainly due to strengthening of the cell wall due to strain hardening behaviour.

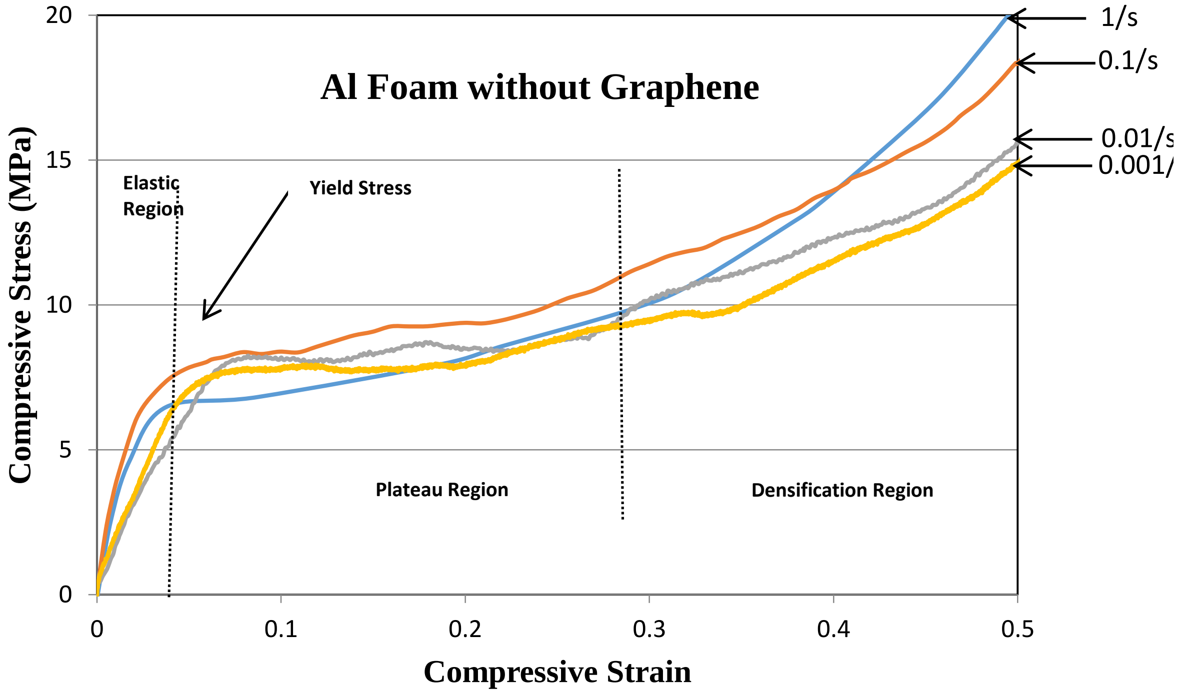

Fig. 4.2: compressive stress-strain diagram of Al-SiC composite foam without Graphene over a strain rates of 0.001s^{-1} to 1s^{-1}.

The energy absorption by the Al composite foam is calculated using a relation as given below:

$$E_{ab}= \text{E (absorbed energy)}= \int_0^{\varepsilon} \sigma_{pl} \varepsilon d \quad (4.1)$$

σ_{pl} = Plateau stress, εd= Nominal Strain

The energy $_{\text{absorption}}$ is calculated to be around 2.24 MJ/m^3.

Table 4.1 shows the peak stress, plateau stress and energy absorption of Al Alloy-SiC composite foam without Graphene at different strain rates under quasi-static load condition.

Table 4.1 Effect of strain rate on the plateau stress and energy absorption of Al composite foam without Graphene under quasi-static load condition.

Strain Rate (s^{-1})	**Peak Stress(MPa)**	**Plateau Stress (MPa)**	**Energy Absorption (MJ/m^3)**
0.001	7.5	8.00	2.24
0.01	8.0	8.00	2.24
0.1	8.0	8.70	2.18
1.0	6.5	8.00	2.24

Figure 4.3 shows the effect of strain rates on the plateau stress of Al-SiC composite foam without Graphene under quasi-static load condition. It is seen that plateau stress is more or less same in quasi-static load condition, in the entire range of strain rate used in the present

investigation. It depicts that plateau stress is insensitive to strain rate under quasi-static load condition. Densification strain is also found independent of strain rate. Figure 4.4 shows the effect of strain rate on the energy absorption of Al Alloy-SiC composite foam without Graphene under quasi-static load condition. Energy absorption is nearly constant at approximately 2.24 MJ/m^3.

4.3. Compressive tests of Al composite foam with 0.5% Graphene at a strain rate of 0.001s^{-1} to 1s^{-1} under quasi-static load

In Al-SiC composite, 0.5wt. % Graphene is mixed with SiC particles and added in liquid Al alloy for foaming. Figure 4.5 shows compressive stress-strain diagram of Al Composite foam with 0.5% GR, deformed over a strain rates of 0.001s^{-1}, 0.01s^{-1}, 0.1s^{-1} and 1s^{-1}. The figure shows initial elastic region showing peak stresses and flat plateau region of plateau stresses in the range of 11 MPa to 12 MPa. The densification strain is found around 0.32. After, densification strain, the stress is found to increase with strain. The densification region is clearly seen in the diagram and marked in Fig. 4.5. The energy absorption is calculated and found around 3.30 MJ/m^3 to 3.83 MJ/m^3. It is noted that dispersing Graphene particle in Al alloy composite foam enhances the plateau stress from 8.0 MPa in without Graphene composite foam to 11 MPa in with Graphene composite foam tested over a strain rates of 0.001s^{-1} to 1s^{-1} (Fig. 4.6). The energy absorption by the foam with Graphene is found around 3.5 MJ/m^3 (Fig. 4.7), Present result shows that by dispersing

0.5 wt. % Graphene with 10% SiC particle, the plateau stress of Al composite foam is increased by 37% and energy absorption is enhanced by 56%.

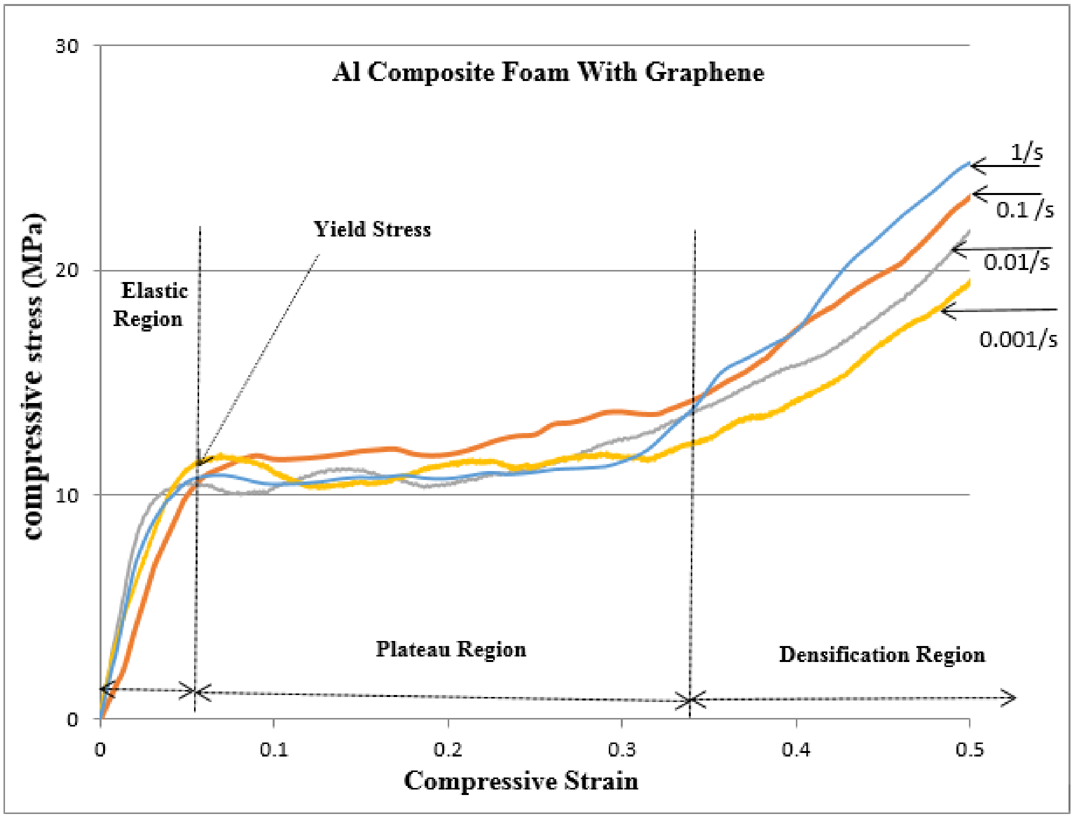

Figure 4.3. Compressive stress-strain diagram of Al composite foam with Graphene at different strain rates of $0.001s^{-1}$, $0.01s^{-1}$, $0.1s^{-1}$ and $1s^{-1}$.

Table 4.2 shows the peak stress, plateau stress, densification strain and energy absorption of Al alloy composite with 0.5% Graphene tested over a range of strain rates $0.001s^{-1}$ to $1.0s^{-1}$.

Table 4.2 Effect of strain rate on the plateau stress and energy absorption of Al-SiC-composite foam reinforced withGraphene under quasi-static load condition.

Strain Rate (s^{-1})	Peak Stress(MPa)	Plateau Stress (MPa)	Energy Absorption (MJ/m^3)
0.001	11	11	3.52
0.01	10.5	11	3.30
0.1	11	12	3.84
1.0	11	11	3.3

The above results inferred that addition of Graphene in Al alloy composite foam shows improved properties in terms of plateau stress and energy absorption. Seeing this behaviour, it is opined that further detailed dynamic carry out tests with Graphene reinforced Al alloy composite foam using Split Hopkinson pressure bar (SHPB) unit. Hence, the results described in the following sections are solely restricted to Graphene Al alloy composite foam with Graphene at dynamic test condition.

4.4. Stress-Strain Diagram of Al composite foam with Graphene (relative density: 0.23) under dynamic loading condition

The stress-strain diagram clearly shows an initial elastic region followed by a peak stress and then after the stress falls to a lower value and mentioned a constant load on which the metal foam deformed i.e., plateau stress. The peak stress is the maximum stress that the metal foam can withstand there is a slight drop in stress following the peak stress to a nearly constant stress level known as the plateau stress. Table 4.4 shows the peak stress at various strain rate of deformation. Figure 4.4 depicts a typical stress-strain diagram of Al composite foam with Graphene of relative density 0.23 and various strain rates ranging from 500 s^{-1} to 2750 s^{-1} shown by different line gradient. The diagram clearly shows that the peak and plateau stress increase with strain rate. For example, at a strain rate of 500s^{-1}, the plateau stress is found around 10 MPa and is increased to 20 MPa when the material tested at a strain rate of 2750 s^{-1}. Fig. 4.4 shows the effect of strain rate on the plateau stress.

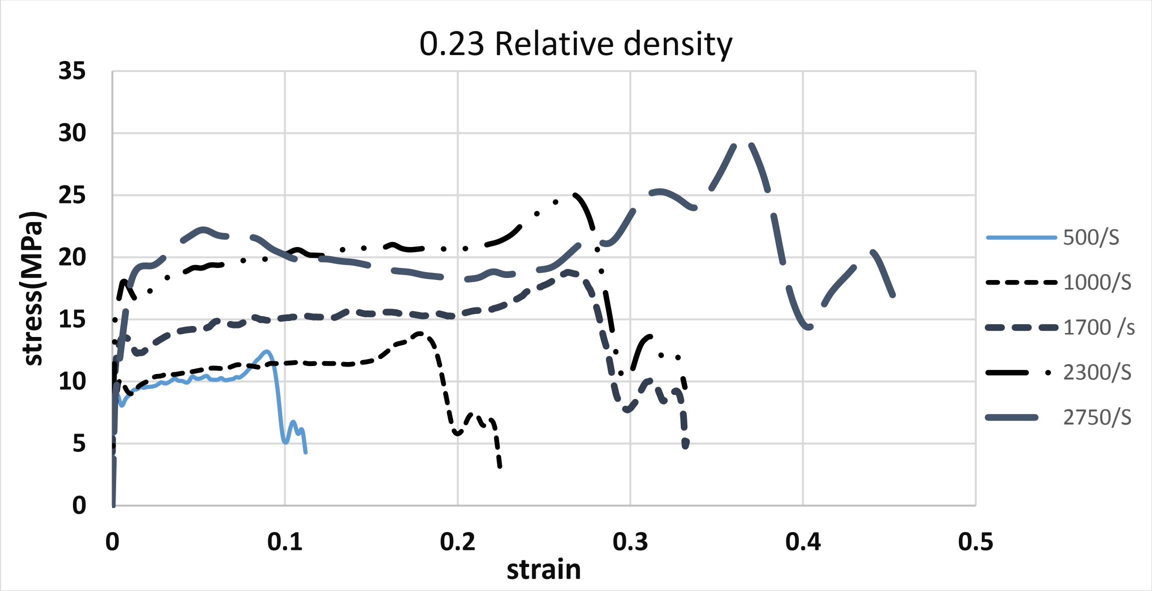

Fig. 4.4. Stress-strain diagram of Al composite foam with Graphene (Relative Density: 0.23) at different strain rate (500 s^{-1}- 2750s^{-1})

Table: 4.3. Effect of Strain rate on the response of foam with relative density of 0.23

Strain Rate (s^{-1})	**Peak Stress (MPa)**	**Plateau Stress(MPa)**	**Energy Absorption (Eab) (MJ/m^3)**
500	8	10	0.08
1000	10	12	1.8
1700	14	15	3
2300	18	20	4
2750	22	22	4.4

The energy absorption per unit volume by the hybrid foam material is calculated by the equation 4.1. These results shows in Table 4.5 clearly indicate that increasing the strain rate of deformation enhances the plateau stress and the energy absoption. The results are also plotted in Fig 4.5 and Fig. 4.6 to show the variation of plateau stress and energy absoption as a function of strain rate respectively.

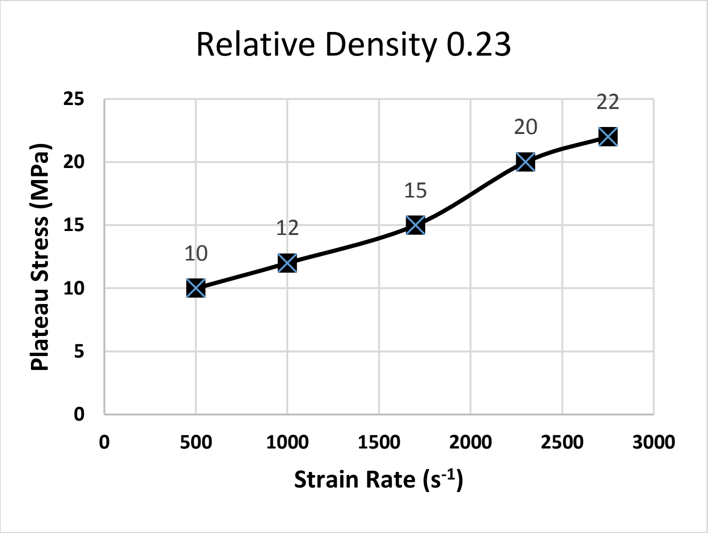

Fig. 4.5 Effect of Strain rate on Plateau stress

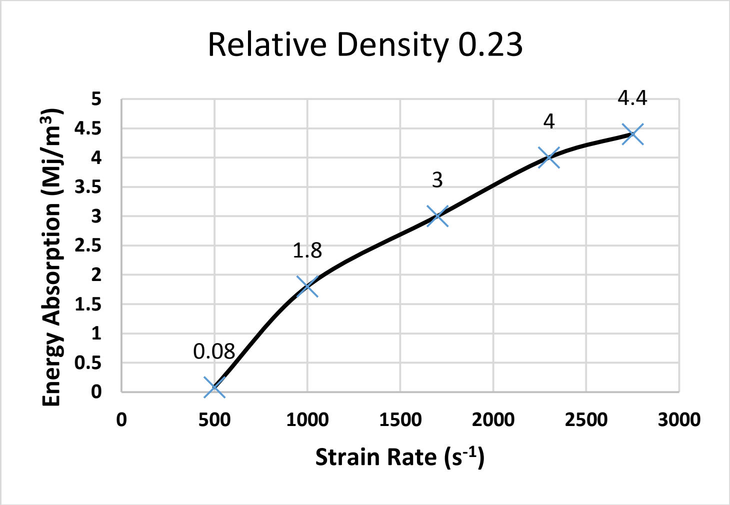

Fig.4.6 Effect of strain rate on the energy absorption

4.5. Stress-Strain Diagram of Al composite foam with Graphene (relative density: 0.24)

Figure 4.7 shows a typical stress-strain diagram of Al composite foam with Graphene of relative density 0.24 tested at various strain rates. The nature of stress-strain diagram is similar to previous diagram (Fig. 4.5). It also shows initial elastic region with a peak stress, and plateau region. It may be noted from the diagram that at a strain rate of 500 s^{-1}, the plateau stress is found to be around 11 MPa. The plateau stress is noted to be increased with strain rate i.e. 1300s^{-1}, the plateau stress is 13 MPa and it is increased to 20 MPa when the foam is tested at a strain rate of 2500s^{-1}. Further, at a strain rate of 2760 s^{-1}, the plateau stress is found 21 MPa (Fig. 4.6). The energy absorption by the hybrid foam is also found out by the equation 4.1.

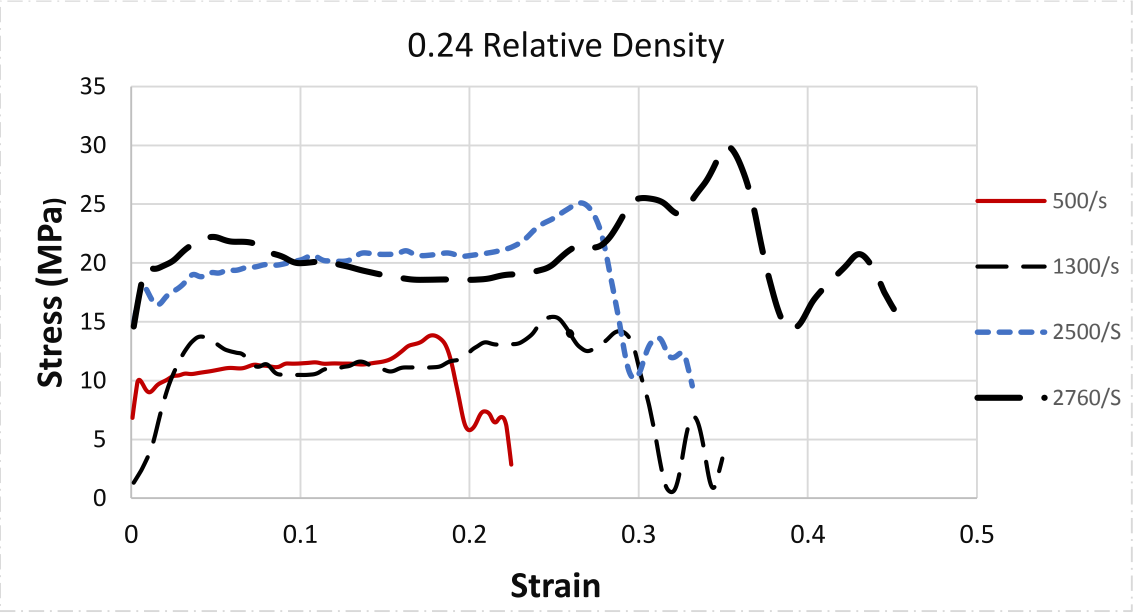

Fig. 4.7 Stress-strain diagram of Al composite foam with Graphene (Relative Density: 0.24) at different strain rate (500 s^{-1} to 2760 s^{-1})

It is noted that the energy absorption is increased from 1.65 MJ/m^3 at a strain rate of

$500s^{-1}$ to 4.20 MJ/m^3 at a strain rate of 2760 s^{-1}. All the values are tabulated and shown in Table. 4.4

Table: 4.4 Effect of Strain rate on the response of foam with relative density of 0.24

Strain Rate (s^{-1})	**Peak Stress (MPa)**	**Plateau Stress (MPa)**	**Energy Absorption (MJ/m^3)**
500	10	11	1.65
1300	14	13	2.6
2500	18	20	4.0
2760	23	21	4.20

Table 4.4 shows that that stress of the foam material increases with strain rate

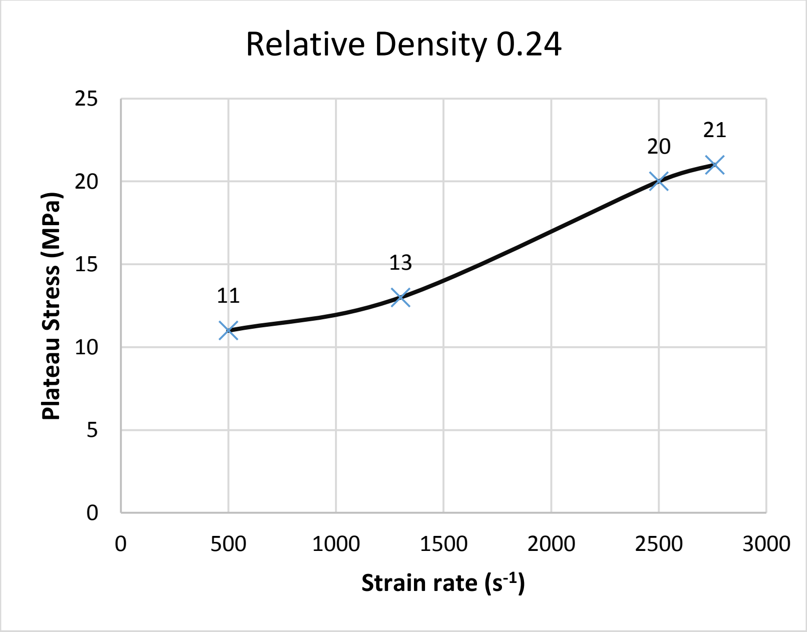

Fig.4.8 Effect of strain rate on plateau stress

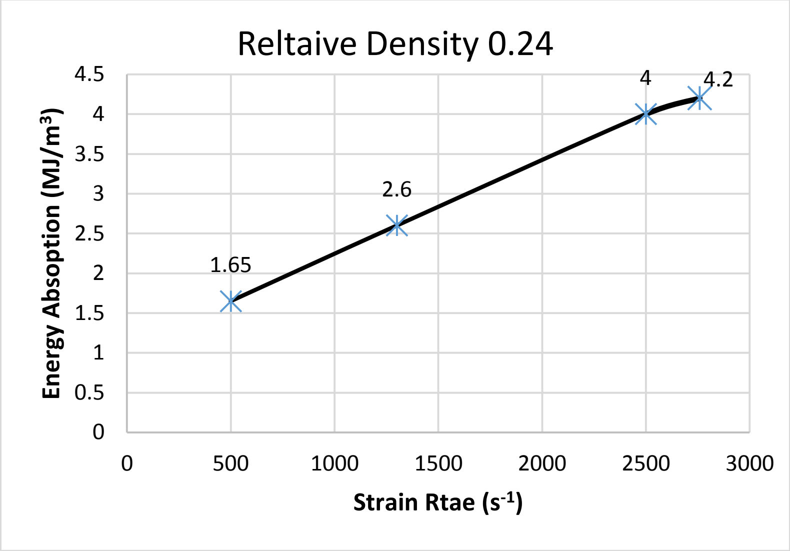

Fig.4.9 Effect of strain rate on the energy absorption

Figure 4.8 shows the effect of strain rate on the plateau stress. It is been noted that plateau stress increases with strain rate. Figure 4.9 depicts the effect of strain rate on the energy absorption of Graphene Al composite foam. It is been noted that energy absorption increases when the material is tested at higher strain rate. This clearly depicts that when the material is been deformed at higher strain rate the energy absorption by the material also increased.

4.6. Stress-Strain Diagram of Al composite foam with Graphene (relative density: 0.25)

Figure 4.10 shows the stress-strain diagram of Al composite foam with Graphene of relative density 0.25. It also shows similar nature of stress-strain diagram as discussed above. It depicts from the diagram that material examined at a strain rate of 1300s^{-1} has an initial elastic region with a peak stress of 11 MPa and a plateau region of plateau stress of 12 MPa. Similarly, when the material tested at a strain rate of 2200s^{-1}, the peak stress is noted around 13 MPa and the plateau stress is observed 15 MPa. When the material is tested at a strain rate of 2620s^{-1}, the peak stress is recorded 22 MPa and the plateau stress is 20 MPa. It may be noted that initially the stress is increased with strain to a value of 22 MPa, and then it progressively decreasing to a lower value of 18 MPa and then it again is increased to higher value. Usually, the deformation is progressing layer-by-layer mechanism at a constant load. The lowering of stress value is observed mainly due to defects exist in the material. The stress-strain diagram depicts that plateau stress is increased with strain rates as shown in the Fig. 4.10

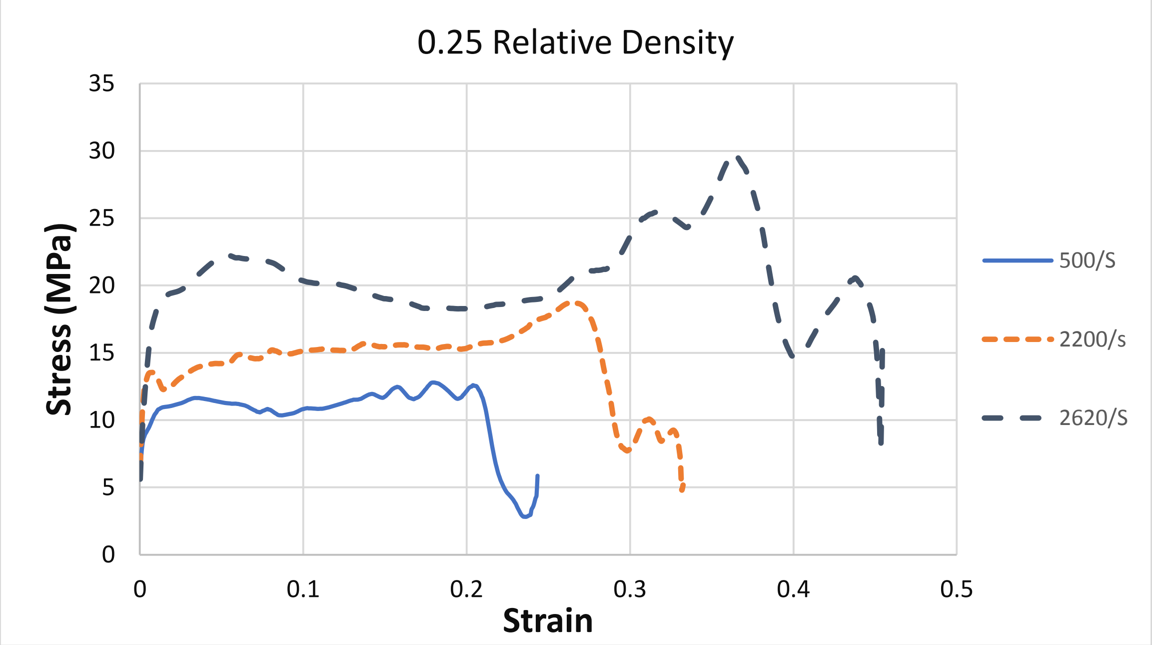

Fig. 4.10 Stress-strain diagram of Al composite foam with Graphene (Relative Density: 0.25) at different strain rate (500 s^{-1} to 2620 s^{-1})

Table: 4.5 Effect of Strain rate on the response of foam with relative density of 0.25

Strain Rate (s^{-1})	Peak Stress (MPa)	Plateau Stress (MPa)	Energy Absorption (MJ/m^3)
500	11	12	2.4
2200	13	15	3
2620	22	20	4

Table 4.5 shows the values of peak stress, plateau stress, etc. at various strain rates. The effect of strain rate on the plateau stress is shown in Fig. 4.11. It can be seen that plateau stress increases with strain rate. The energy absorption by the Al composite foam with Graphene at different strain rates is shown in Fig. 4.12. It is noted that at a strain rate of $500s^{-1}$, the energy absorbed by the material is 2.4 MJ/m^3 and material tested at higher strain rate say at $2620s^{-1}$, the energy absoebed by the foam material is 4.0 MJ/m^3 . Figure 4.12 clearly shows the increasing tendency of energy absorpsion with strain rate. It is an well understood fact that at higher strain rate usually higher pressure is being used and the primary bar strikes the sample with higher stress which inturn compresses the sample more and also the plateau stress observed is more. This results clearly indicated that deformation of Al composite foam with Graphene from a strain rate of $500s^{-1}$ to $2620s^{-1}$, the energy absorbtion increased to an amount of 70%, whereas plateau stress is increased to a value of 79%.

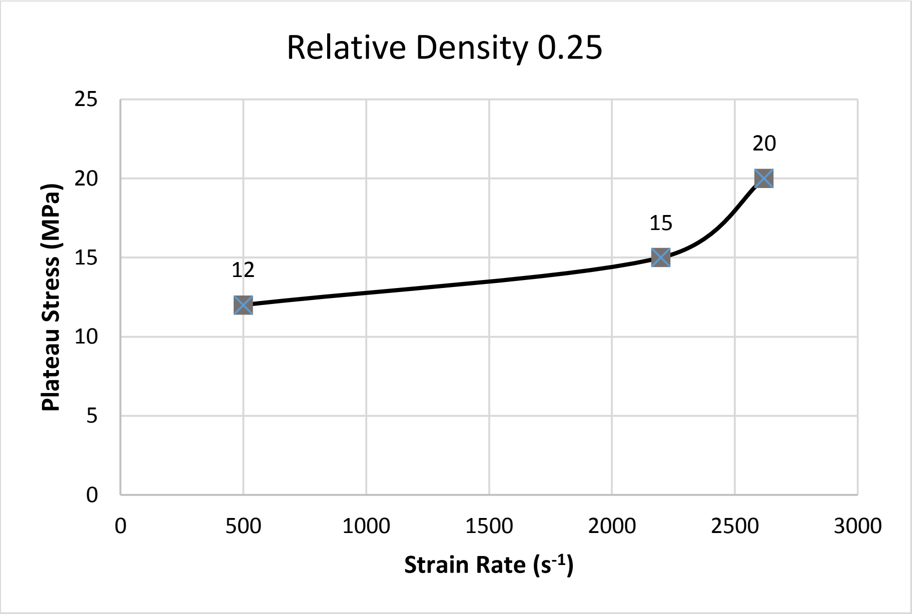

Fig.4.11 Effect of strain rate on plateau stress

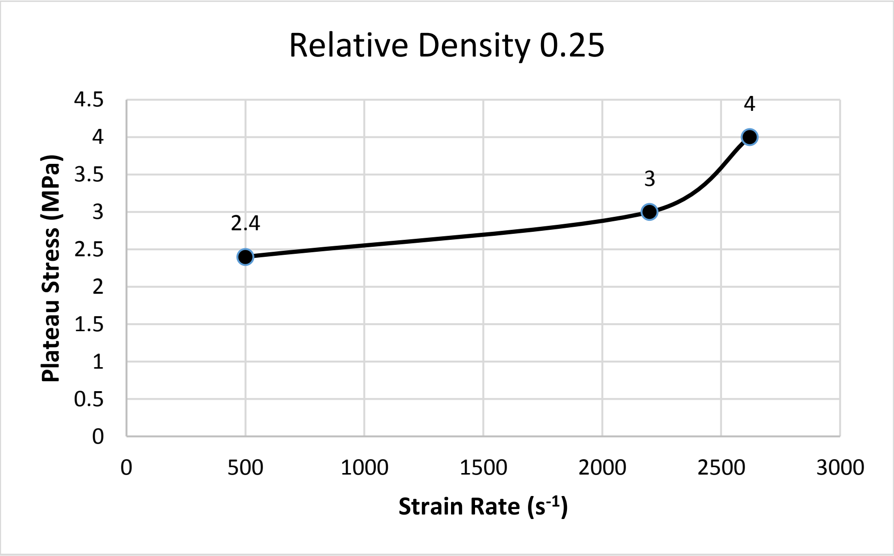

Fig.4.12 Effect of strain rate on the energy absorption

4.7. Stress-Strain Diagram of Al composite foam with Graphene (relative density: 0.26)

The stress-strain diagram of hybrid composite of relative density 0.26, at various strain rates is shown in Fig. 4.13. The strain rates used in this figure are 1000s^{-1}, 1500s^{-1} and

2500s^{-1}. The plots corresponding to the strain rate 1000s^{-1}, depicts initial elastic region of peak stress 11 MPa and a flat plateau region of plateau stress of 10 MPa. The second plot shows stress-strain diagram at a strain rate of 1500s^{-1} it also shows a peak stress of 13 MPa and a flat plateau region with a plateau stress of 15 MPa and densification strain of 0.22. It also shows densification region and decreasing tendency of stress value. The stress-strain diagram of the material tested at a strain rate of 2500s^{-1} shows a peak stress of 21 MPa, and there is a decreasing tendency of stress just after a strain value of 0.05. This decreasing tendency of stress signifies that there must be some defects in the sample in upper portion of the sample. Again, the stress is found to increase with strain and crosses a value of 20 MPa.

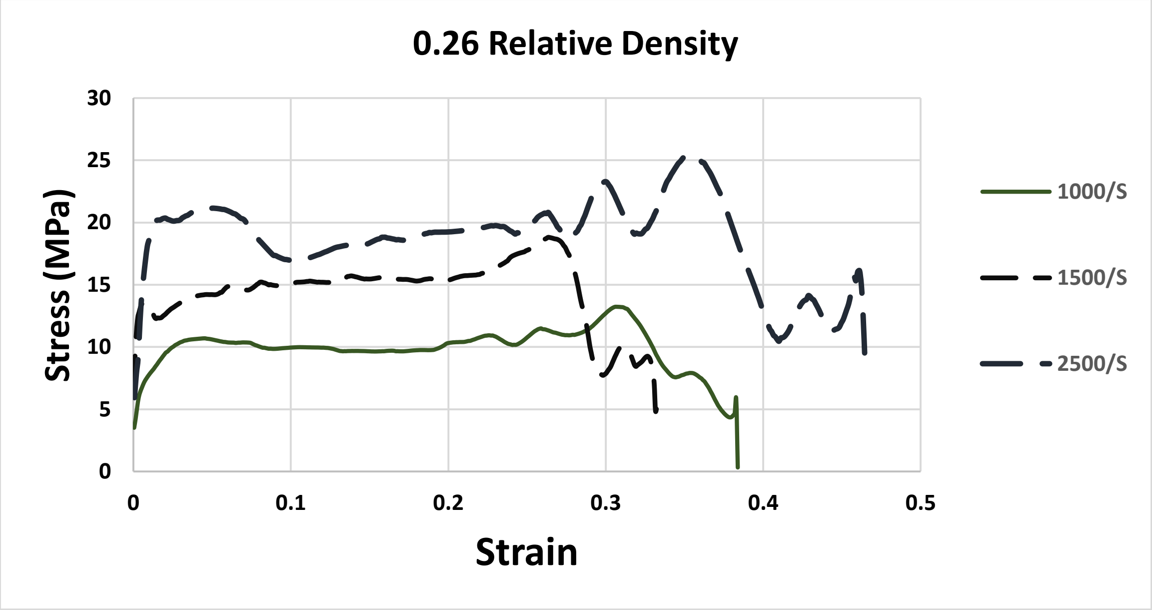

Fig. 4.13. Stress-strain diagram of Al composite foam with Graphene (Relative Density: 0.26) at different strain rate (1000 s^{-1} to 2500 s^{-1})

Table: 4.6. Effect of Strain rate on the response of foam with relative density of 0.26

Strain Rate (s^{-1})	**Peak Stress (MPa)**	**Plateau Stress (MPa)**	**Energy Absorption (MJ/m^3)**
1000	11	10	2
1500	13	15	3
2500	21	20	4

The energy absorption by the hybrid foam material is calculated and found around 2 MJ/m^3 at a strain rate of 1000s^{-1}. The energy absorption is found to increase to 3 MJ/m^3, when the material is tested at a strain rate of 1500s^{-1}. Further at a strain rate of 2500s^{-1}, the energy absorption is found 4 MJ/m^3. All the values are shown in Table 4.6. From the Table 4.6, it is clearly depicts that the plateau stress is increased with increasing strain rate. The energy absorption by the foam material is also increased with increasing strain rate of deformation. These behaviour are shown in Fig. 4.14 and 4.15. It is also to be mentioned at this juncture that all the sample tesed at different strain rate have almost same density. It is also to be mentioned that seeing the stress-strain diagram that the plateau region is almost flat and no sign of strain hardening effect of the cell walls was noted.

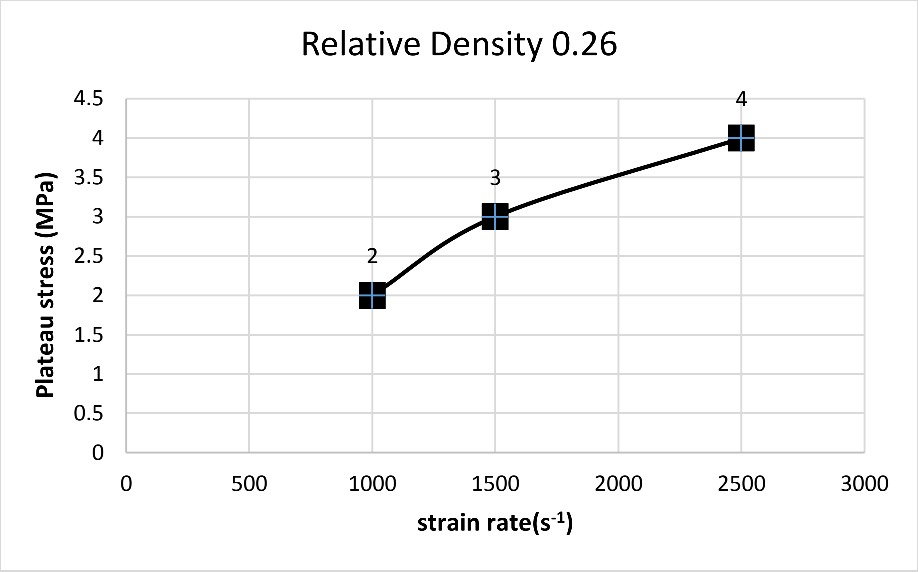

Fig.4.14 Effect of strain rate on plateau stress

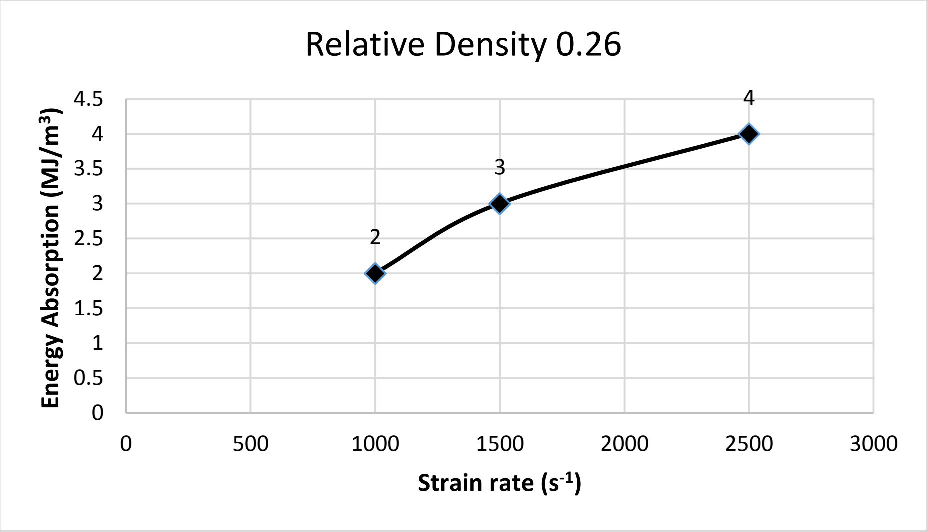

Fig.4.15 Effect of strain rate on the energy absorption

4.8 Stress-Strain Diagram of Al composite foam with Graphene (relative density: 0.27)

Figure 4.16 shows a typical stress-strain diagram of Al composite foam with Graphene of relative density 0.27, deformed at strain rates of 500s^{-1} to 2600s^{-1}. The stress-strain diagram of the material deformed at a strain rate of 500s^{-1} shows linear elastic region with a peak stress of 12 MPa and plateau stress of 12 MPa. The stress-strain diagram of the material also clearly shows an elastic region of peak stress 14 MPa and a plateau region and plateau stress 13 MPa. When the plateau region is not flat, enough on that case average of highest and lowest vales are taken. The densification strain is found around 0.14. The stress-strain diagram of the material deformed at 2300s^{-1} is also shows elastic region with a peak stress of 15 MPa and plateau stress of 14 MPa. In this case, the plateau stress is found by averaging the highest and lowest values of plateau region. The stress-strain diagram of the hybrid foam deformed at a strain rate of 2600s^{-1} is also showed a linear elastic region with a peak stress of 18 MPa and a flat plateau region of plateau stress of 20 MPa.

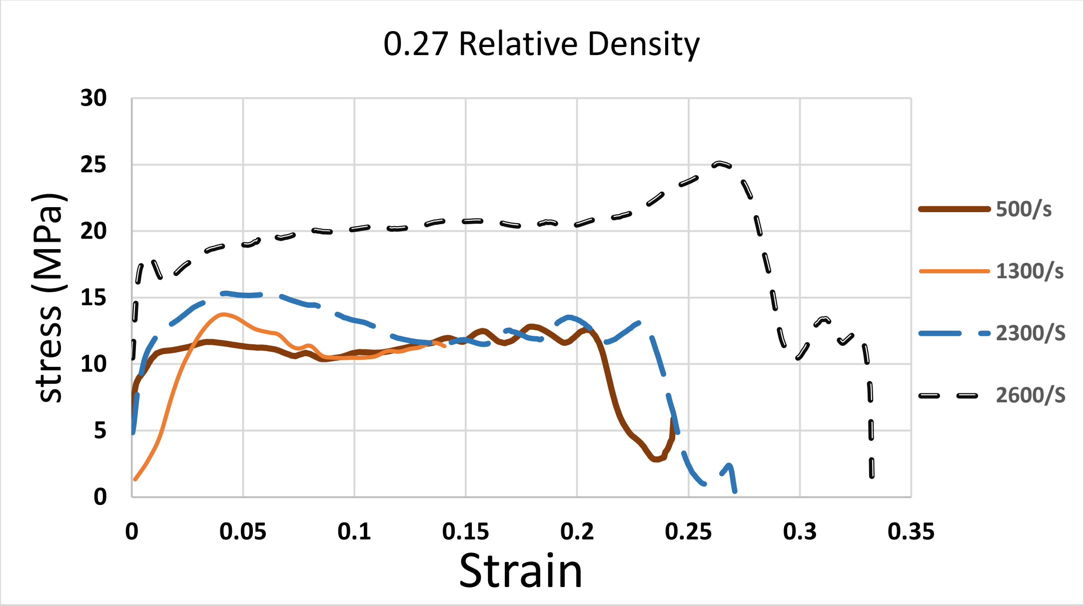

Fig. 4.16. Stress-strain diagram of Al composite foam with Graphene (Relative Density: 0.27) at different strain rate (500 s^{-1} to 2600 s^{-1})

Table 4.7 Effect of Strain rate on the response of foam with relative density of 0.27

Strain Rate(s^{-1})	**Peak Stress (MPa)**	**Plateau Stress(MPa)**	**Energy Absorption (MJ/m^3)**
500	12	12	2.4
1300	14	13	2.6
2300	15	14	2.8
2600	18	20	4

The energy absorption of Al composite foam with Graphene is calculated and shown in the Table 4.7 along with other values. It is noted from the Table 4.7 that the energy absorption is found 2.4 MJ/m^3 at a strain rate of 500s^{-1} and is increased to 4 MJ/m^3 at a strain rate of 2600s^{-1}. When the material is deformed at strain rates 1300s^{-1} and 2300s^{-1}, the energy absorption is found to be around 2.6 MJ/m^3 and 2.8 MJ/m^3 respectively. The results shown in Table 4.7, that the plateau stress is sensitive to strain rate of deformation. The energy absorption is also found sensitive to strain rate of deformation. Figure 4.17 and Fig. 4.18 show the effect of strain rate on the plateau stress and energy absorption. Both the curves showed increasing tendency with strain rate domain used in the present investigation.

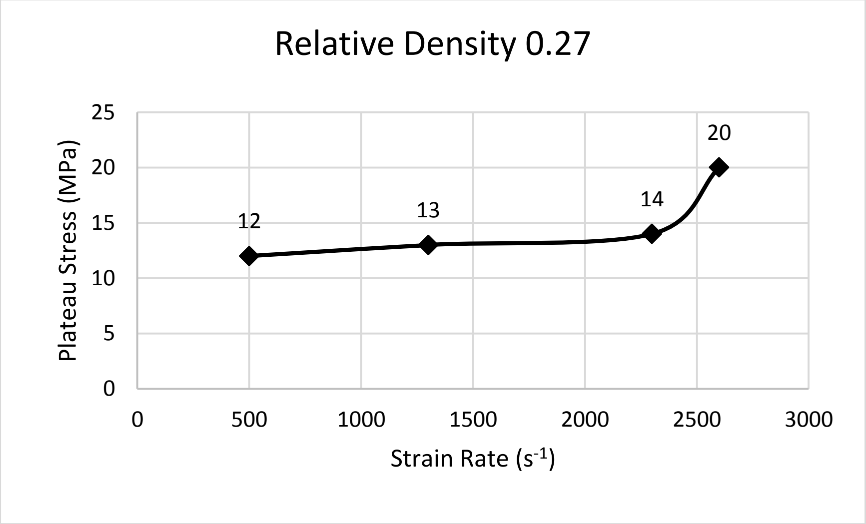

Fig.4.17 Effect of strain rate on plateau stress

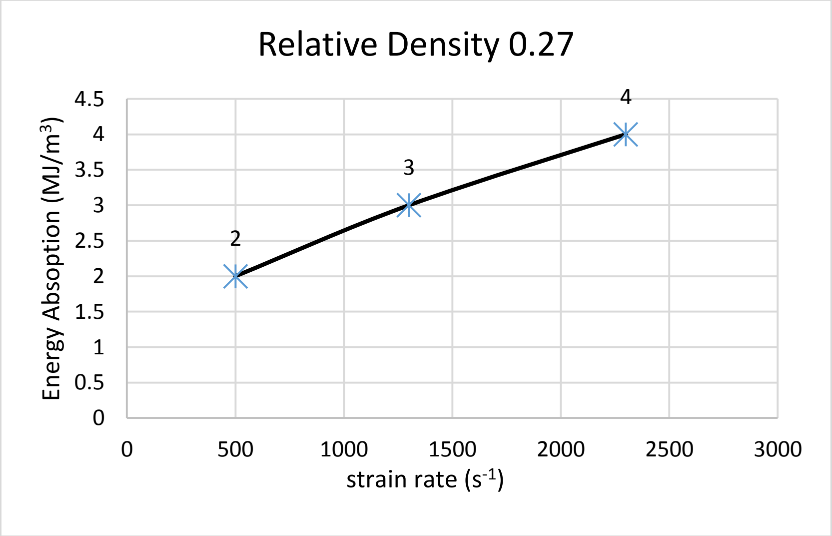

Fig.4.18 Effect of strain rate on the energy absorption

4.9 Stress-Strain Diagram of Al composite foam with Graphene (relative density: 0.28)

The stress-strain diagram of hybrid composite of relative density 0.28 is shown in Fig. 4.19. The stress-strain diagram is plotted in three-strain rate e.g., 1000s^{-1}, 2200s^{-1}, and 2600s^{-1}. The stress-strain diagram of hybrid foam deformed at 1000s^{-1} shows initial elastic region with a peak stress of 10 MPa and shows flat plateau region with a densification region of 0.26. After a strain value of 0.26, the stress is increased and then decreased to a lower value. In the case of sample deformed at 2200s^{-1}, the peak stress is found 13 MPa and then the stress is increased to 15 MPa up to a densification strain value of 0.25. After the strain value of 0.25, the stress value reduced drastically to a lower value indicating failure of material. Further, deforming the material at higher strain rate, i.e., at 2600s^{-1}, the peak stress is found around 21 MPa and the plateau stress is calculated to be around 21 MPa. This diagram also shows a similar nature of stress-strain diagram of sudden increase in stress and then decreased to a lower value.

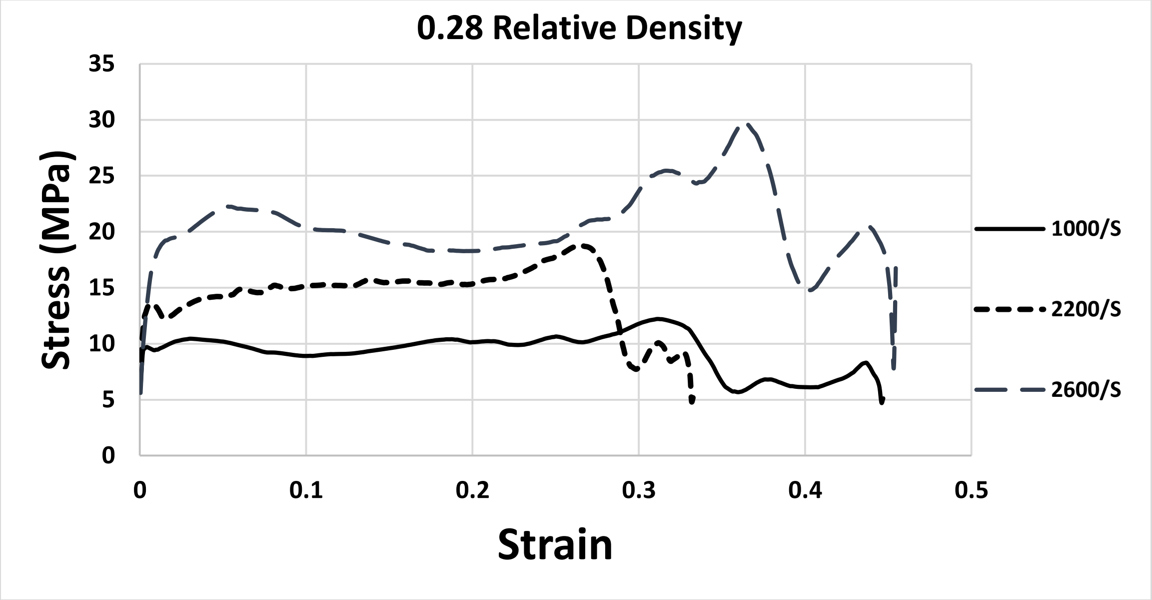

Fig.4.19. Stress-strain diagram of Al composite foam with Graphene (Relative Density: 0.28) at different strain rate (1000 s^{-1} to 2600 s^{-1})

Table 4.8: Effect of Strain rate on Plateau Stress (MPa) at a relative density of 0.28

Strain Rate (s^{-1})	**Peak Stress (MPa)**	**Plateau Stress(MPa)**	**Energy Absorption (MJ/m^3)**
1000	10	10	2
2200	13	15	3
2600	22	20	4

The energy absorption by the hybrid foam is calculated and found 2 MJ/m^3 at a strain rate of 1000s^{-1}. For the strain rates of 2200s^{-1} and 2600s^{-1} the energy absorption is calculated around 3 MJ/m^3 and 4 MJ/m^3 respectively. Table 4.8 shows all the values namely peak stress, plateau stress, densification strain and energy absorption. Fig. 4.24 shows the effect of strain rate on the plateau stress of the material. It is observed that plateau stress increases with the strain rate of deformation. Higher the strain rate of deformation achieves increased plateau stress and increased energy absorption (Fig. 4.25). It is observed that when the strain rate of deformation is increased from 1000s^{-1} to 2200s^{-1} the energy absorption is increased from 2 to 3, which is around 40% improvement. Further enhancing the strain rate to 2600s^{-1}, the energy absorption is increased to 4 MJ/m^3.

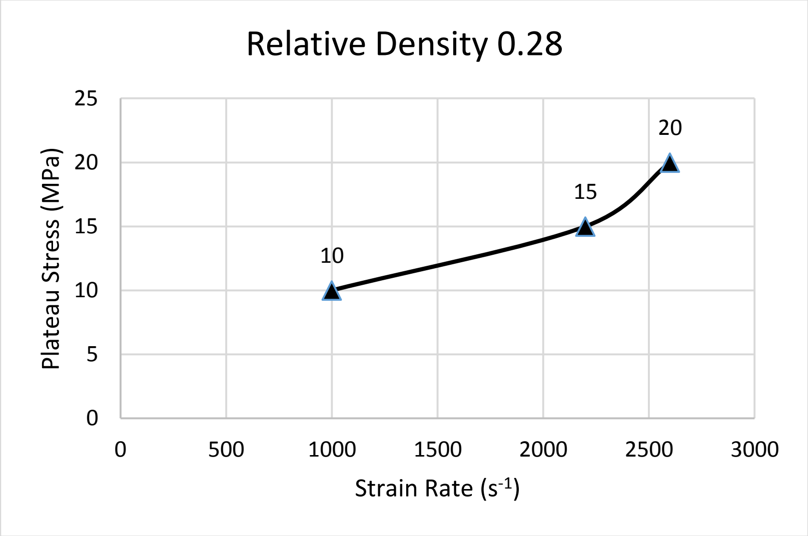

Fig.4.20 Effect of strain rate on plateau stress

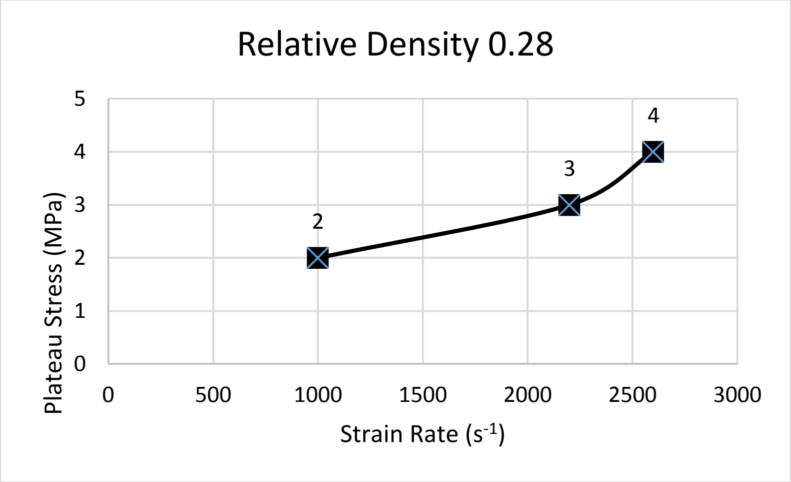

Fig.4.21 Effect of strain rate on the energy absorption

4.10. Stress-Strain Diagram Al composite foam with Graphene (relative density: 0.29)

Figure 4.22 shows the typical stress-strain diagram of hybrid foam of density 0.29 tested at strain rates of 500s^{-1}, 1000s^{-1}, 2200s^{-1} and 2760s^{-1}. It is noted that material tested at a strain rate of 500s^{-1} shows initial elastic region with a peak stress of 10 MPa and flat plateau region with a plateau stress of 10 MPa. The densification strain is found around 0.27. After densification strain of 0.27, the stress is increased with strain and then falls drastically to a lower lever indicating failure of material. The stress-strain diagram of the sample tested at a strain rate of 1000s^{-1} also shows initial elastic region with a peak stress of 11 MPa and flat plateau region with a plateau stress of 11 MPa. The densification strain is found around 0.20. After densification strain, the stress decreased to a lower value indicating failure of material. Similar trend for the testing of material at a strain rate of 2200s^{-1} is also shows initial elastic region with a peak stress of 14 MPa and flat plateau region of plateau stress of 15 MPa. The densification strain is found around 0.22. After densification, the stress value is found increased and then decreased to a lower value indication failure of material. The stress-strain diagram of the material tested at a strain rate of 2760s^{-1} is shown in Fig. 4.26. This shows an initial elastic region with a peak stress of 22 MPa and plateau stress of 20 MPa.

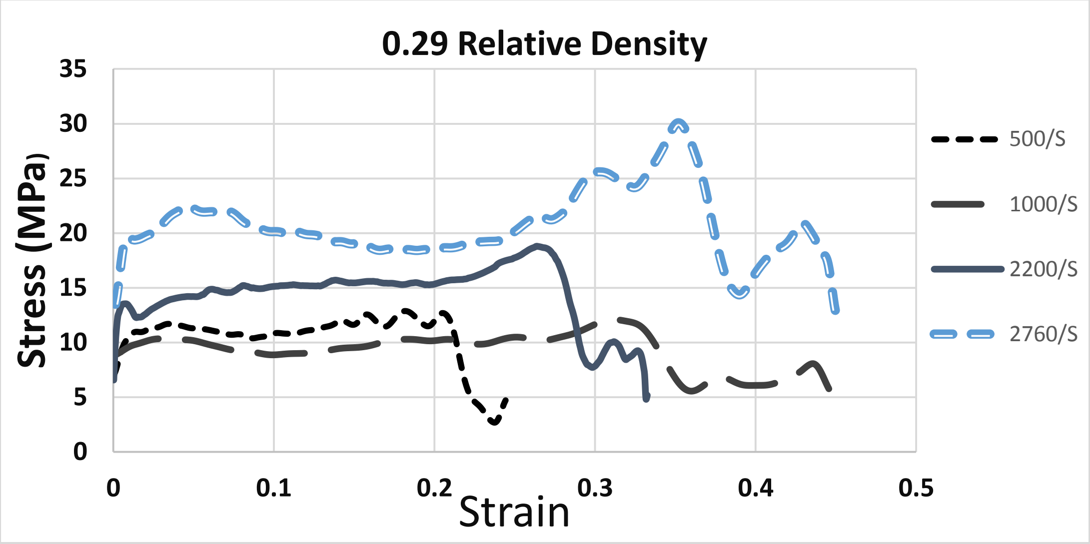

Fig. 4.22. Stress-strain diagram of Al composite foam with Graphene (Relative Density: 0.29) at different strain rate (500 s^{-1} to 2760 s^{-1})

Table 4.9: Effect of Strain rate on Plateau Stress (MPa) at a relative density of 0.29

Strain Rate (s^{-1})	**Peak Stress (MPa)**	**Plateau Stress(MPa)**	**Energy Absorption (MJ/m^3)**
500	10	10	2
1000	11	11	2.2
2200	14	15	3
2760	22	20	4

The energy absorption by the material having relative density of 0.29 is calculated and energy absorption value along with other values is shown in Table 4.9. When the material is tested at a strain rate of 500s^{-1}, the energy absorption is 2 MJ/m^3.Further when the material is tested at a strain rate of 2200s^{-1} the energy absorption by the material is 3 MJ/$m^{3.}$ Still higher strain rate deformation of material i.e., at 2760s^{-1}, the energy absorption is increased to 4.0 MJ/$m^{3.}$ There is a gradual increase of energy absorption with respect to strain rate.

Figure 4.23 shows the effect of strain rate on the plateau stress of Al composite foam with Graphene. It shows that plateau stress is increasing with strain rate. Figure 4.24 shows the effect of strain rate on the energy absorption of the foam. It also shows increasing tendency of energy absorption with strain rate. It may be observed from Table 4.9 that the energy absorption is just doubled when the strain rate is enhanced from $500s^{-1}$ to $2760s^{-1}$. It is also to be noted that the densification strain has no relation with strain rate of the experiments done in the present domain of experimental parameters. All the experimental results of dynamic tests are shown comprehensively.

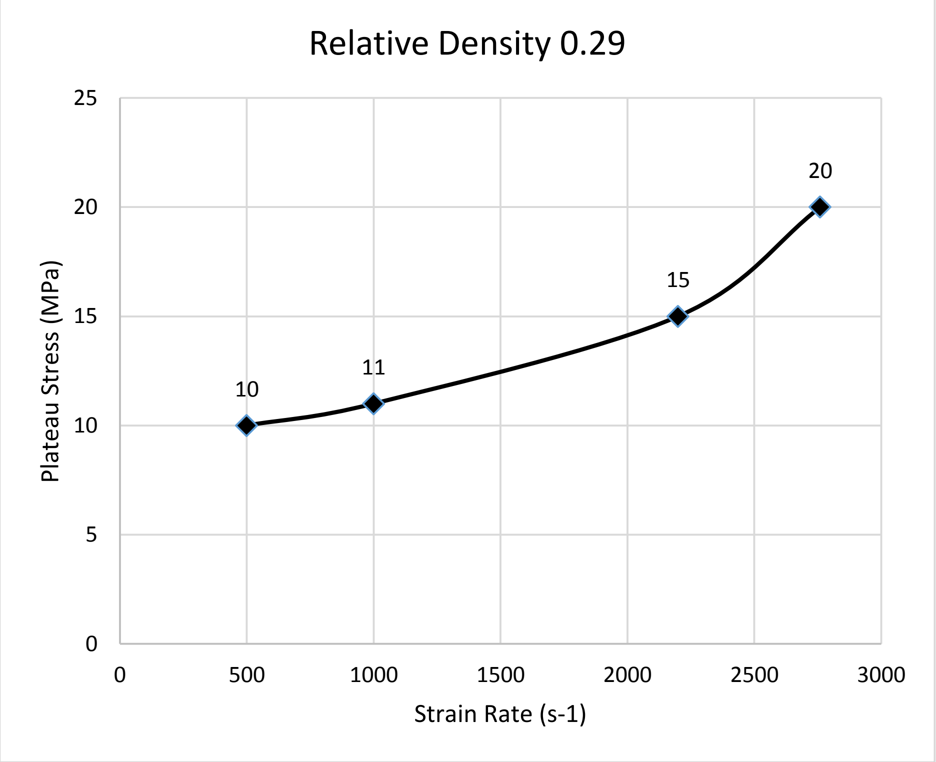

Fig.4.23 Effect of strain rate on plateau stress

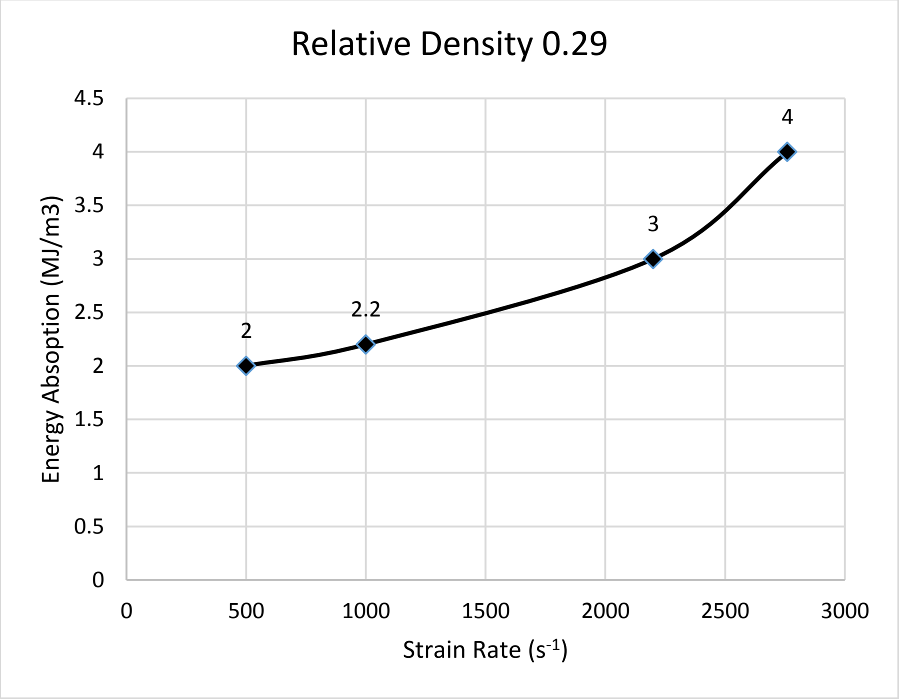

Fig.4.24 Effect of strain rate on the energy absorption

Table: 4.10. Values of peak stress, plateau stress, plateau strain, energy abrorption and density of Al composite foam with Graphene at various strain rates.

Relative Density	Actual Density of Foam (gm/cc)	Strain Rate (s^{-1})	Peak Stress MPa	Plateau Stress MPa	Energy Absorption MJ/m^3
0.23	0.64	500	8	10	0.08
		1000	10	12	2.4
		1700	14	15	3
		2300	18	20	4
		2750	22	22	4.4
0.24	0.67	500	10	11	1.5
		1300	14	13	2.04
		2500	18	20	4
		2760	23	21	4.2
0.25	0.70	500	11	12	2.4
		1300	11	12	2.4
		2200	13	15	3
		2620	22	20	4
0.26	0.728	1000	11	10	2
		1500	13	15	3
		2500	21	20	4
0.27	0.756	500	12	12	2.4
		1300	14	13	2.6
		2300	15	14	2.8
		2600	18	20	4
0.28	0.784	1000	10	10	2
		2200	13	15	3
		2600	22	21	4
0.29	0.812	500	10	10	2
		1000	11	11	2.2
		2200	14	15	3
		2760	22	20	4

Chapter 5

Discussion of Results

The deformation behavior of aluminum foams reinforced with Nano Graphene sheets to the best of our knowledge has not been studied in detail under dynamic condition (strain rate >100s^{-1}). If the energy absorption is higher at higher dynamic loading, it is better to use less foam materials; on the other hand, if the energy absorption of these materials is less at higher strain rate, one will under estimate the foam materials for using at higher strain rate. As a result, for efficient and optimum design of foam components for shock and impact energy absorption, one must examine and understood the deformation behavior and mechanism under dynamic condition (strain rate >100s‑1 and up to about 3000s^{-1}). The present thesis is addressed to understand the deformation behavior of Al composite foam with and without Graphene under static and dynamic loading conditions.

5.1 Graphene Al foam Microstructure

Figure 5.1 shows a SEM micrograph of foam structure. It shows pores of size 500 μm and SiC particles distributed in the cell walls. Figure 5.2 shows a higher magnification SEM micrograph showing SiC particles in the cell walls.

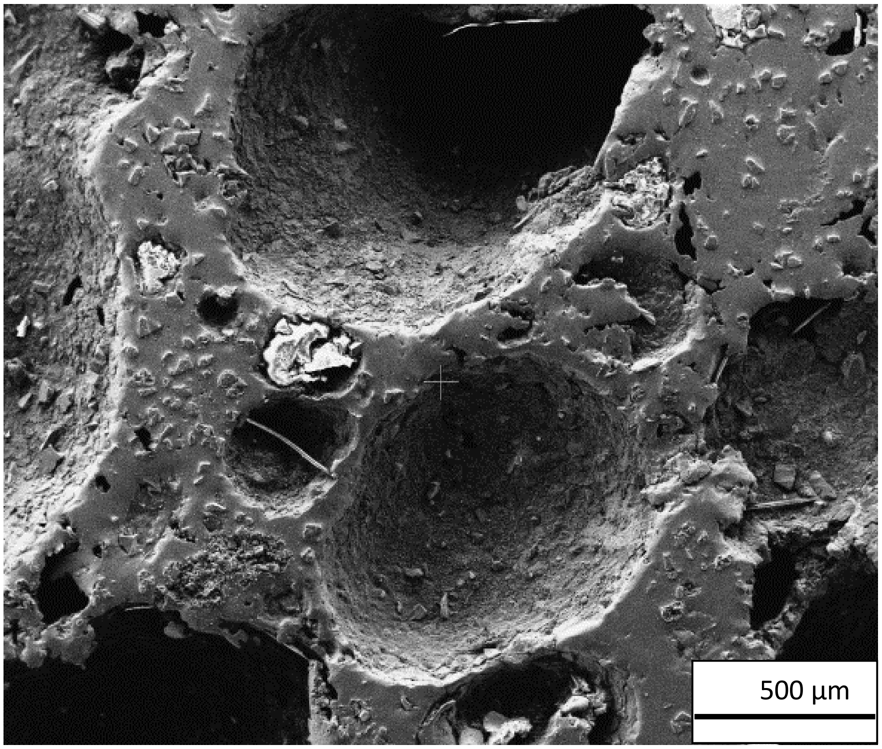

Fig. 5.1 SEM micrograph of Al-SiC foam with Graphene showing pores and distribution of SiC particles in the cell walls

Additionally, in the present work, 0.5wt. % Graphene was dispersed along with SiC particles. Figure 5.1 shows a typical microstructure of as such Graphene Nano sheets not in Al composite. A higher magnification micrograph clearly shows the sheet structure of Graphene Fig. 5.2. The Graphene Nano sheets are usually attached to the SiC particles and form an improved bonding between Al-SiC-and Graphene. Due to the addition of Graphene in composite foam the plateau stress as well as energy absorption of the foam is increased by 20-25 % (compare Table 4.1 and 4.2). Wang et.al (83) have also reported that addition of 0.3% of Nano Graphene sheets in Al alloy enhanced the tensile strength by 62% over the unreinforced alloy.

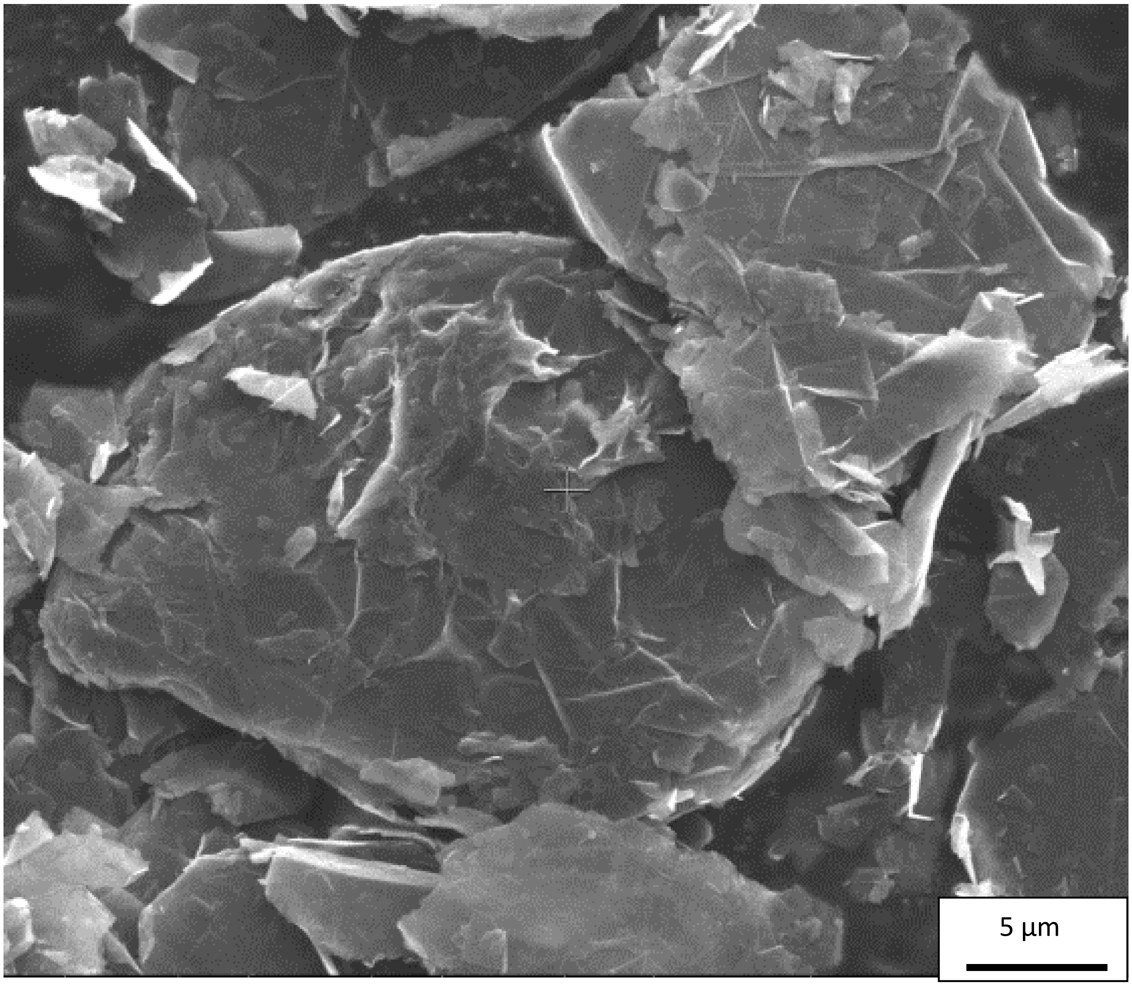

Fig. 5.2 Higher Magnification micrograph of Graphene sheets

It is obvious from the present investigation that SiC particles simply contributed towards the stability of the foam and on the other hand, Nano Graphene sheets facilitate strengthening of the cell walls apart from stability.

The stress-strain plots of compressive deformation study of Al Alloy-SiC foam and Al alloy composite foam with Graphene show three distinct regions. These are initial linear elastic region, secondly a flat plateau region, and then lastly a densification region. During compressive deformation of foam, the deformation mechanism proceeds by a layer-by-layer compression mechanism. At the initial stage, top layer is deformed, which shows the initial elastic region of stress-strain compressive deformation plot. At the initial elastic region, the bending of the cell walls and edges control the deformation and the load is transferred to the next layer. Further increasing the stress, the deformation of the next layer is taking place and in this way at a fixed stress the cellular material gets compressed with increasing strain (24). As the strain value increases the cell walls usually touching each other and material get densified at a constant plateau stress. The foam material experiences buckling of cell wall and the deformation band is found perpendicular to the loading direction in which plastic collapse of cells take place. It is also noted that marginal increase in plateau region, as seen mainly in quasi-static load, is mainly represented by strain hardening behavior of the cell wall material. It is a well-known fact that Al alloy is amenable to strain hardening and alloy like Al 5083 containing 5.5% of Mg sustain the ductility (59). The SiC particles that are added in the Al matrix are mainly to enhance the viscosity of the liquid metal and facilitate the stability of foam structure. The presence of SiC in the cell wall largely affects the elastic properties and the failure mechanism of the foam sample. In compressive deformation of Al 5083 Alloy-SiC composite foam, the sample gets compressed without fracturing. In some cases, it was observed that foam sample is fractured badly during compressive tests, which happen mainly due to segregation of SiC particles in the cell walls and it also depend upon the matrix alloy used for making foam. During the deformation process, the cracks nucleate mainly at the Al-SiC interfaces and latter it propagates and joins together to from the fracture of cell walls. In the case of Al composite foam with Graphene, the stress – strain diagram shows improved plateau stress over the Al-SiC composite foam. The energy absorption of Al composite foam with Graphene also shows improvement over the Al-SiC composite foam.

It is interesting to note that ratio of plateau stress of Al composite foam with Graphene to Al-SiC composite foam without Graphene is 1.2 to 2.0 times higher and as a function of strain rate. Similar trends of result reported by Kang Ying-an et.al. (84) in their experiments of closed cell Al-SiC foam of density 0.457 gm/cc (less density than ours (0.65 g/cc)) shows that peak stress and plateau stress increased with strain rate. The peak stress (2.8 MPa) and plateau stress (3.4 MPa) as reported by Kang Ying-an et.al (84) is less than our results. This may be due to lower density. However, their experiments in dynamic testing restricted up to a strain rate of 1600s^{-1}. The ratio of energy absorption of Al composite foam with Graphene to Al-SiC foam without Graphene is in the range of 1.29 to 2.08. Hamada et.al (85) studied the static and dynamic compressive tests of Al-Ca closed cell Al alloy foam and reported that the dynamic plateau stress of Al alloy foams was about 1.1 times larger than the static one. However, in our case it is 1.24 at strain rate of 500s‑1 to 1.6 times in the strain rate of 1300s^{-1}. This improvement is essentially due to effect of Nano Graphene sheets. This clearly infers that addition of Nano Graphene sheet in Al-SiC composite foam enhanced the plateau stress and also the energy absorption capability of Al alloy foam. It is observed in the present investigation that specific energy absorption in static test and dynamic test (up to a strain rate of 1300 $^{-1}$). Similar results reported by Kenny et.al (53). However, above a strain rate of 1300s^{-1}, the energy absorption is much higher than the static test. The above results are quite similar to the results observed in the present investigation. Deshpande and Fleck (54) studied the Alulight (closed pore) and Duocel (open pore) foam at quasi static (0.001s^{-1}) and dynamic test SHPB, (3680s^{-1}) and reported that plateau stress (10 MPa – 11 MPa) in both the cases are more or less same and found insensitive to strain rate only there is a change in the nature of curve (Duocel foam shows smoother curve than the Alulight foam). Pal and Ramamurthy (57) have studied the compression behavior of closed cell Alporas foam at a strain rate of $10^{-5}s^{-1}$ to $10^{-1}s^{-1}$. Their results depicted that plateau stress and energy absorption increased by 31 and 52.5 % as the strain rate increases. The plateau stress and energy absorption values reported by Pal and Ramamurthy (57) are slightly lesser than that of our values. This may be due to the effect of Nano Graphene sheets in cell walls of the foam.

In the present investigation attempt has been made to investigate the compressive deformation behavior of Al-Composite foam with Graphene at relative densities in the range of 0.23 to 0.29 tested at strain rates of $1000s^{-1}$, $-2760s^{-1}$ (Table 5.1, 5.2, 5.3). It has observed that strain rate at $1000s^{-1}$, the plateau stress found in the range of 10-13 MPa of densities 0.23 to 0.29. This clearly depicts that density of the foam material used in the present experimental domain has not effect much on the plateau stress. Similarly, at a strain rate of $2700s^{-1}$, the plateau stress found in the range of 20-22 MPa of the foam material of relative density 0.23-0.29. This again confirms that density, in the range 0.23-0.29, will not affect much on the plateau stress. It was also observed from the Tables that at a strain rate of 1000s‑1, the energy absorption of the foam material is found in the range of 2-2.4 MJ/m^3. Further foam tested at a strain rate of 2700s‑1, the energy absorption is found in the range of 4.0 – 4.4 MJ/m^3.

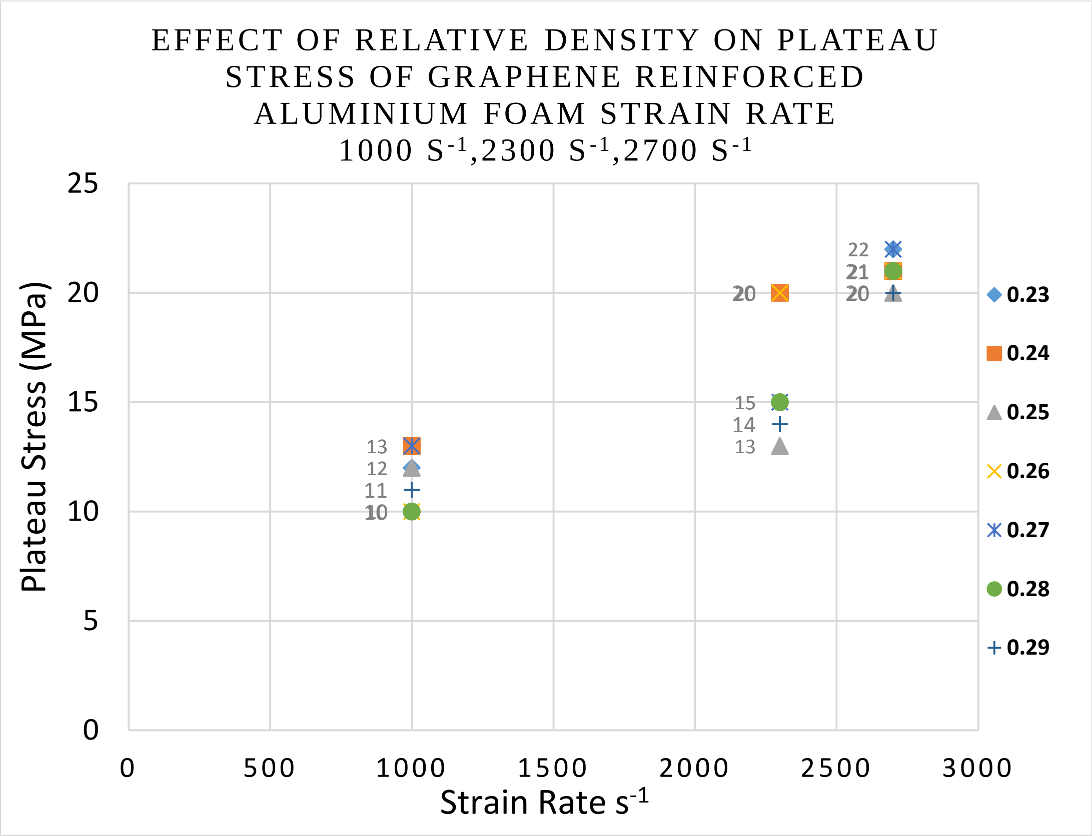

Fig.5.3. Shows the Effect of relative density on plateau stress of Graphene reinforced aluminium foam strain rate 1000 s^{-1},2300 s^{-1},2700 s^{-1}

CONCLUSIONS

1. The closed cell Al composite foam with pore size around 500-700 μm the relative density in the range of 0.23 to 0.29 was studied under static and dynamic loading at various train rate. SiC particles were added in Al alloy melt to achieve the stability of foam structure.) 0.5wt. % Nano Graphene sheet was dispersed with SiC particles to strengthen the cell walls. In the present investigation, the quantity of Graphene is restricted to 0.5wt. % because 0.5wt. %Graphene has a quite appreciable volume and while dispersing Graphene, in Al alloy melt, the viscosity of the liquid metal appears to increase to a greater extent and handling (stirring) the melt would be a problem.

2. The compressive deformation stress-strain diagram shows three distinct regions namely the linear elastic region, flat plateau region and finally the densification region. In most of the cases plateau region is seen flat however, in some cases plateau region signified as increases stress with strain. This increasing behaviour of stress with strain is mainly observed due to strain hardening of cell walls. In some instances, after reaching the peak stress instead of maintaining a constant stress for deformation, it was seen decreasing tendency of stress with strain, this mainly occurs due to the presence of defects in the foam structure. Once the whole material densified, there is a steep increase in the stress with strain.

3. A servo hydraulic machine was used to study the compressive behaviour of foam under quasi-static loading condition tested at strain rates of $0.001s^{-1}$, $0.01s^{-1}$, $0.1s^{-1}$ and $1.0s^{-1}$. It was observed that strain rate does not have any effect of plateau stress and energy absorption of Al-SiC composite foam under the domain of strain rate used in the present study. From stress-strain diagram, Plateau stress is found around 8 MPa and energy absorption is calculated and found around 2-3 MJ/m^3. On the same experimental condition, the hybrid composite foam shows increased plateau stress (10 MPa) and energy absorption is found around 3-5 MJ/m^3. The plateau stress and the densification strain are seen to be independent of the applied strain rate.

4. The dynamic compressive stress-strain curves of the hybrid composite closed cell Al foam of different relative density tested in the strain rate of $500s^{-1}$ to $2700s^{-1}$. The plateau stress is seen sensitive to strain rate but insensitive to densification strain. It is also noted that plateau stress is insensitive to relative density of Graphene Al foam. The plateau stress increases with strain rate, this increase is around 1.5 times irrespective of relative density

of the material. Energy absorption by the Graphene Al foam is also increased with strain rate. The enhancement of energy absorption is around 2 times irrespective of the relative density.

5. The essence of the present thesis lies in the fact that there is ample scope exist in the development of closed cell Al hybrid foam with the addition of Nano sheet Graphene. Presence of Graphene in the cell walls enhances the strength of the cell walls in large extent and stability of foam structure to some extent.

FUTURE SCOPE OF WORK

Aluminium alloy hybrid foam reinforced with Graphene proves to be a potential material for improved mechanical properties and energy absorption properties. This kind of metal foam shows potential applications in crashworthiness and noise and vibration attenuation essentially in transportation sectors. To meet the demand for such applications, the foam materials are to be tested over a range of strain rates right from $0.001s^{-1}$ to $4000s^{-1}$. In quasi static the compression tests of the material can be evaluated by a precision servo hydraulic machine, which can give up to a strain rate of $100s^{-1}$. Similar way, a Split Hopkinson Pressure bar unit can provide the compression properties in the strain range of $1000s^{-1}$ to $4000s^{-1}$. While in the range of strain rate over $100s^{-1}$ to $1000s^{-1}$, a drop test unit may be used. While seeing the literature on deformation behaviour of Al foam, we could not come across a literature discussed about hybrid composite foam with Graphene. There is some information available in the literature mentioning that addition of 0.3 wt.% Graphene could enhance the strength of the normal composite by 63%. To my opinion one should try for

Graphene reinforced hybrid composites for making closed cell Al foam for crashworthiness applications. Moreover, it was also noticed that foam filled multi channels could be a useful product for various applications in noise and vibration attenuation and also for crash. In recent days' considerable emphasis has been focussed on the impact crashworthiness application in automobile and railways. One should also design for blast resistant panels using Al hybrid foam as core and steel sheet as cover material. For noise and vibration attenuation one should look for foam core sandwich panels with polymer sheets. From the present investigation it was observed that densification strain is restricted to 0.3-0.4. This value is well below the expectation for designing component at least for crashworthiness application. Hence one has to look into this factor how to increase the densification strain value keeping plateau stress constant so that maximum foam material could be used for crash application. Further, in order to have a thorough understanding of deformation mechanism of foam, cell wall bending etc. one should go for a detailed high resolution SEM observation at each strain rate. These trends of research highlighted above would not be possible by a single student, within the limited time scale available, but could be possible to do by the subsequent available student's time to time.

References

1 Gibson, L. J., & Ashby, M. F. (1997) Cellular solids 2nd Edition, Cambridge University Press New York.

2 T. J. Lu, Audrey Hess, and M. F. Ashby, Sound absorption in metallic foams, J. Appl. Phys., Vol. 85, No. 11, 1 June 1999, pp-7528-7539

3 John Banhart, Manufacture, characterisation and application of cellular metals and metallic foams, Prog Mater. Sci. 46 (2001)559–632.

4 Miyoshi T, Itoh M, Akiyama S, Kitahara K., ALPORAS Aluminum Foam: Production Process, Properties, and Applications Adv. Eng. Mater 2(4), (2000)179-183

5 D.P.Mondal, M.D. Goel and S. Das, Compressive deformation and energy absorption characteristics of closed cell aluminum-fly ash particle composite foam Mater. Sci. Eng. A, 507, 102(2009).

6 John Banhart, Manufacturing routes for metallic foam J. Metal, 12, 22 (2000).

7 P. H. Thornton, C. L. Magee: The deformation of aluminum foams, *Metallurgical Transactions A*, 6A (1975) 1253-1263.

8 F. Han, Z. Zhu, J. Ga: Compressive deformation and energy absorbing characteristic of foamed aluminum, *Metallurgical Transactions A*, 29A **(1998**) 2497-2502.

9 W. Andrews, W. Sanders, L. J. Gibson: Compressive and tensile behavior of aluminum foams, *Materials Science and Engineering A*, 270 **(1999**) 113-124.

10 P. J. Tan, S.R. Reid, J.J. Harrigan, Z. Zou, S. Li: Dynamic compressive strength properties of aluminum foams. Part I-Experimental data and observations, *Journal of the Mechanics and Physics of Solids*, 53 (2005) 2174-2205.

11 X. Zhang, G. Cheng: A comparative study of energy absorption characteristics of foam-filled and multi-cell square columns, International Journal of Impact Engineering, 34 (2007) 1739–1752.

12 F.Campana, D.Pilone: Effect of wall microstructure and morphometric parameters on the crush behavior of Al-alloy foams, *Materials Science & Engineering A*, 479(1-2) (2008) 58-64.

13 Z. Li, J. Yu, L. Guo: Deformation and energy absorption of aluminum foam-filled tubes subjected to oblique loading, *International Journal of Mechanical Sciences*, 54 (2012) 48-56.

14 P. Pinto, N. Peixinho, F. Silva, D. Soares: Compressive properties and energy absorption of aluminum foams with modified cellular geometry, *Journal of Materials Processing Technology*, 214 (2014) 571-577.

15 S. Mohsenizadeh, R. Alipour, M. Shokri Rad, A. Farokhi Nejad, Z. Ahmad: Crashworthiness assessment of auxetic foam-filled tube under quasi-static axial loading, *Materials and Design*, 88 (2015) 258-268.

16 Y. Alvandi-Tabrizi, D.A. Whisler, H. Kim, A. Rabiei: High strain rate behavior of composite metal foams, *Materials Science & Engineering A*, 631 (2015) 248–257.

17 D. Karagiozova, D.W. Shu, G. Lub, X. Xiang: On the energy absorption of tube reinforced foam materials under quasi-static and dynamic compression, *International Journal of Mechanical Sciences*, 105 (2016) 102-116.

18 Jiwei Wang, Xudong Yang, Miao Zhang, Jiajum Li, Chunsheng Shi, Naiqin Zhao, Taichung Zou, A novel approach to obtain in-situ growth carbon Nanotube reinforced aluminum foams with enhanced properties, Materials Letters, 161 (2015)763-766.

19 Isabel Duarte, Eduardo Ventura, Sisana Olhero, Jose MF Ferreira, A novel approach to prepare aluminum alloy foams reinforced by carbon Nano tubes, Materials Lett. 160 (2015)162-166.

20 Min Zeng, Han Wang, Chong Zhao, Jiake Wei, Wenlong Wang, Xuedong Bai, 3D Graphene foam-supported cobalt phosphate and borate electro catalysis for high efficiency water oxidation, Sic. Bull, 60(16) 2015, 1426-1433.

21 Yarjan Abdul Samad, Yuanqing Li, Saeed M. Alhassan, Kin Liao, Noval Graphene foam composite with adjustable sensitivity for sensor applications, Appl. Mater and Interfaces, DOI:10.1021/acsami.5b01608 (2015)

22 Reinforcement with Graphene Nanosheets in aluminum matrix composites, Jingyue Wang,a Zhiqiang Li, Genlian Fan, Huanhuan Pan, Zhixin Chenb, and Di Zhanga, Scripta Materialia, 66 (2012) 594–597

23 Meador, M. A., et al. (2010). DRAFT Nanotechnology Roadmap Technology Area 10. National Aeronautics and Space Administration (NASA). 5. Available at:http://www.nasa.gov/pdf/501325main_TA10-Nanotech-DRAFT-Nov2010-A.pdf

24 L.-Y. Chen et al., Novel Nano processing route for bulk Graphene Nano platelets reinforced metal matrix Nanocomposites, Scripta Materialia 67 (2012) 29–32.

25 F. Chen et al., Effects of Graphene content on the microstructure and properties of copper matrix composites, Carbon 96 (2016) 836-842.

26 Bancroft, D., 'The velocity of longitudinal Waves in cylindrical Bars', physical Review, V.59 No.59, (1941) pp.588-593.

27 D. A. Gorham, "A numerical method for the correction of dispersion in pressure bar signals", Journal of Physics E: Scientific Instruments, vol. 16, pp. 477-479, 1983

28 P. S. Follansbee, C. Frantz, "Wave Propagation in the Split Hopkinson Pressure Bar", Journal of Engineering Materials and Technology, vol. 105, pp. 61-66, 1983

29 J. C. Gong, L. E. Malvern, D. A. Jenkins, "Dispersion Investigation in the Split Hopkinson Pressure Bar", Journal of Engineering Materials and Technology, vol. 112, pp. 309-314, July 1990.

30 J. M. Lifshitz and H. Leber, "Data processing in the Split Hopkinson Pressure bar tests", International Journal of Impact Engineering, vol. 15, No. 6, pp. 723-733, 1994

31 Bertram Hopkinson, "A method of Measuring the Pressure produced in the Detonation of High Explosives or by the Impact of Bullets", Philosophical Transactions of the Royal Society of London, Series A, vol. 213, pp. 437-456, 1914

32 H. Kolsky, "An Investigation of the mechanical properties of Materials at very high rates of loading", Proc. Phys. Soc. (London), vol. 62B, pp. 676-700, 1949

33 Bazle A. Gama, Sergey L. Lopatnikov, John W. Gillespie Jr., "*Hopkinson bar experimental tenique: A critical review*", American Society of Mechanical Engineers, vol. 57, No. 4, pp. 223-250, July 2004

34 George T. (Rusty) Gray III, "Classic Split-Hopkinson Pressure bar testing", ASM Handbook, vol. 8: Mechanical Testing and Evaluation, pp. 462-476, 2000

35 R.M. Davies, A critical study of the Hopkinson pressure bar, Philosophical Transactions A 240 (1948), 375–457.

36 P.S. Follansbee and C. Frantz, Wave propagation in the split Hopkinson pressure bar, J. Engng. Materials and Tech. 105 (1983), 61–66.

37 Jin *et al. (1990)* Method of producing lightweight foamed metal. US Patent No. 4,973,358.

Jin *et al.* (1992) Stabilized metal foam body. US Patent No. 5, 112, 697.

Jin *etal.* (1993) Lightweight metal with isolated pores and its production. US Patent No. 5,221,324.

Kenny *et al.* (1994) Process for shape casting of particle stabilized metal foam. US Patent No. 5,281,251.

38 Akiyama *et al.* (1987) Foamed metal and method of producing same. US Patent No. 4,713,277.

39 Miyoshi, T., Itoh, M., Akiyama, S. and Kitahara, A. (1998) *Aluminum foam, ALPORAS, the production process, properties and applications,* Shinko Wire Company, Ltd, New Tech Prod. Div., Amagasaki, Japan.

40 Baumeister, J. (1988) Methods for manufacturing foamable metal bodies. US Patent 5,151,246 Yu, C.-J. and Eifert, H. (1998) Metal foams. *Advanced Materials & Processes* November, 45-47.

MEPURA. (1995) Alulight. Metallpulver GmbH. Brannau-Ranshofen, Austria.

41 T Mukai, Kanahashi H, Miyoshi T, Mabuchi M, Nieh TG, Higashi K. Experimental study of energy absorption in a closed-celled aluminum foam under dynamic loading. Scripta Mater 1999; 40:921-7.

42 C.J. Yu, Eiferet HH, Banhart J, Baumeister J. Metal foams. Adv Mater Processes (1998), 11:45-7

43 L.J. Gibson, Mechanical behaviour of metallic foams. Annu Rev Mater Science (2000); 30:191-227.

44 F. Han, Z. Zhu, and J. Gao, Compressive Deformation and energy absorbing characteristic of foamed aluminum. MetallMater Trans. A (1998); 29:2497 – 502.

45 Bart-Smith H, Bastawros A. F. Mumm D. R., Evans A.G., Sypeck D. J. and Wadley H. N. G., Acta. Mater. 1998, 46 (10), 3583.

46 Andrews E., Sanders W. and Gibson L. J., "Compressive and tensile behaviour of aluminum foams," Mater. Sci. Eng., 1999, A270, 113.

47 Dannemann KL, James Jl. High strain rate compression of closed-cell aluminum foams. Mater Sci Eng, A (2000); 293:157-64.

48 Hsiao HM, Daniel IM, Coreds RD. Strain rate effects on the transverse compressive and shear behaviour of unidirectional composites. J Compos Mater (1999); 33: 1620-42.

49 Simone AE, Gibson LJ. The compressive behaviour of porous copper made by the GASAR process. J Mater Sci. (1997); 32: 451-7

50 Yamada Y, Shimojima K, Sakaguchi Y. Compressive properties of open-cellular SG91A A1 and AZ91 Mg. Mater Sci. Eng, A (1999); 272: 455-8.

51 J. J. Harrigan, S. R. Reid and C. Peng. Inertia effects in impact energy absorbing materials and structures, Int. J. Impact Eng 22(1999), pp. 955-979

52 M.F. Ashby, L. Gibson, A Evans. Metal foams—A design guide [M]. Boston: Butterworth-Heinemann, 2000.

53 L.D. Kenny. Mechanical properties of particle stabilised aluminum foam J. Materials Science Forum, 1996, 217−222: 1883−1890.

54 V.S. Deshpande N A. Fleck, High strain rate compressive behaviour of aluminum alloy foams J. International Journal of Impact Engineering, , 24, 2000, 277−298.

55 J. Lankford, K.A. Dannemann, Strain rate effects in porous materials, J. Proceedings of symposium of Material Research Society, 1998, 521: 103−108.

56 D. Ruan , G. Ju , F.L. Chen , E. Siores, Compressive behaviour of aluminum foams at low and medium strain rates J. Composite Structures, 2002, 57: 331−336.

57 A Paul U. Ramamurty Strain rate sensitivity of a closed-cell aluminum foam J. Material Science and Engineering A, 281, 2000, 1-7

58 I. Elnasri, S. Pattofatto, H. Zhao, H. Tsitsiris, F. Hild, Y. Girard, Shock enhancement of cellular structures under impact loading: Part I. Experiments, J. Journal of the Mechanics and Physics of Solids, 2007, 55(12): 2652−2671.

59 H. Kanahashi , T. Mukai , Y. Yamada, K. Shimojima, M. Mabuchi, T. G. Nieh, H. Higashi, Dynamic compression of an ultra-low density aluminum foam, J. Material Science and Engineering A, 2000, 280: 349−353.

60 K.A. Dannemann, J.Lankford, High strain rate compression of closed-cell aluminum foams, J. Material Science and Engineering A, 2000, 293: 157−164.

61 T. Mukai, T. Miyoshi, S. Nakano, H. Somekawa, K. Higashi, Compressive response of a closed-cell aluminum foam at high strain rate, J. Scripta Materialia, 2006, 54(4): 533−537.

62 Cao Xiao-qing, Wang Zhi-hua, MA Hong-wei, Zhao Long-mao, Yang Gui-tong. Effects of cell size on compressive properties of aluminum foam, J. Transactions of Nonferrous Metals Society of China, 2006, 16(2): 351−356.

63 M. Peroni, L. Peroni, M. Avalle, High strain-rate compression test on metallic foam using a multiple pulse SHPB apparatus, Journal de Physique IV, 2006, 134: 609−616.

64 Edwin Raj R, V. Parameswaran, BSS Daniel. Comparison of quasi-static and dynamic compression behavior of closed-cell aluminum foam, J. Materials Science and Engineering A, 2009, 526: 11−15.

65 Wang Zhi-hua, Jing Lin, Zhao Long-mao, Elasto-plastic constitutive model of aluminum alloy foam subjected to impact loading, J. Transactions of Nonferrous Metals Society of China, 2011, 21(3): 449−454.

66 K. Myers, B. Katona, P. Cortes, I. N. Orbulov: Quasi-static and high strain rate response of aluminum matrix syntactic foams under compression, *Composites: Part A*, 79 (2015) 82-91.

67 A. Szlancsik, B. Katona, K. Majlinger, I. N. Orbulov: Compressive behavior and microstructural characteristics of iron hollow sphere filled aluminum matrix syntactic foams, *Materials*, 8 (2015) 7926–7937.

68 James Cox, Dung D. Luong, Vasanth Chakravarthy Shunmugasamy , Nikhil Gupta1,*, Oliver M. Strbik and Kyu Cho Dynamic and Thermal Properties of Aluminum Alloy A356s-1ilicon Carbide Hollow Particle Syntactic Foams *Metals* **2014**, *4*, 530-548; doi:10.3390/met4040530.

69 T. Fiedler, M. Taherishargh, L. K. Opara, M. Vesenjak: Dynamic compressive loading of expanded perlite/aluminum syntactic foam, *Materials Science & Engineering A*, 626 (2015) 296–304

70 D. Karagiozova, D.W. Shu, G. Lub, X. Xiang: On the energy absorption of tube reinforced foam materials under quasi-static and dynamic compression, *International Journal of Mechanical Sciences*, 105 (2016) 102-116.

71 Q. Gao, L. Wang, Y. Wang, C. Wang: Crushing analysis and multiobjective crashworthiness optimization of foam-filled ellipse tubes under oblique impact loading, *Thin-Walled Structures*, 100 (2016) 105-112.

72 O. Mohammadih, H. Ghariblu: Crush behavior optimization of multi-tubes filled by functionally graded foam, *Thin-Walled Structures*, 98 (2016) 627-639.

73 C. Kılıcaslan: Numerical crushing analysis of aluminum foam-filled corrugated single- and double-circular tubes subjected to axial impact loading, *Thin-Walled Structures*, 96 (2015) 82-94.

74 F. Li, G. Sun, X. Huang, J.Rong, Q.Li: Multiobjective robust optimization for crashworthiness design of foam filled thin-walled structures with random and interval uncertainties, *Engineering Structures*, 88 (2015) 111-124.

75 Z. Xiao, J. Fang, G. Sun, Q. Li: Crashworthiness design for functionally graded foam-filled bumper beam, *Advances in Engineering Software*, 85 (2015) 81-95.

76 S. Mohsenizadeh, R. Alipour, M. Shokri Rad, A. Farokhi Nejad, Z. Ahmad: Crashworthiness assessment of auxetic foam-filled tube under quasi-static axial loading, *Materials and Design*, 88 (2015) 258-268.

77 M. D. Goel: Deformation energy absorption and crushing behavior of single-, double- and multi-wall foam filled square and circular tubes, *Thin-Walled Structures*, 90 (2015) 1-11.

78 Zhang, H. Zhou, L. Wu, G. Chen: Bending collapse theory of thin-walled twelve right-angle section beams filled with aluminum foam,*Thin-Walled Structures*, 94 (2015) 45-55.

79 Francisco García-Moreno, Commercial Applications of Metal Foams: Their Properties and Production *Materials* 2016, *9*(2), 85; doi:10.3390/ma9020085

80 Louis-Philippe Lefebvre, * John Banhart and David C. Dunand, Porous Metals and Metallic Foams: Current Status and Recent Developments,Adv. Engg. Mater. DOI: 10.1002/adem.200800241.

81 High Strain Rate Behavior of Graphene Reinforced Polyurethane Composites, Sanjeev K. Khanna and Ha T. T. Phan *J. Eng. Mater. technol* 137(2), 021005 (Apr 01, 2015)

82 K.S. Vecchio and F. Jiang, “Improved pulse shaping to achieve constant strain rate and stress equilibrium in Split-Hopkinson pressure bar testing”, Metallurgical and Materials Transactions A 38, 2655–2665 (2007).

83 Jingyue Wang, Zhiqiang Li, Genlian Fan, Huanhuan Pan, Zhixin Chen and Di Zhang, reinforcement with Graphene Nano sheets in aluminum matrix composites, Scripta Materialia 66 (2012) 594–597

84 KANG Ying-an, ZHANG Jun-yan, TAN Jia-cai, Compressive behavior of aluminum foams at low and high strain rates, **J. Cent. South Univ. Technol.** (2007)s1−0301−05, **DOI:** 10.1007s‑111771−007−0269−8

85 Takeshi Hamada, Hidetaka Kanahashi, Tetsuji Miyoshi and Naoyuki Kanetake, Effects of the Strain Rate and Alloying on the Compression Characteristics of Closed Cell Aluminum Foams Materials Transactions, Vol. 50, No. 6 (2009) pp. 1418 to 1425